Università degli Studi Roma TRE

e

Consorzio Nazionale Interuniversitario per le Scienze Fisiche della Materia

Dottorato di Ricerca in Scienze Fisiche della Materia
XXV ciclo

Electronic properties of strained graphene

Tesi di dottorato del dott. F. M. D. Pellegrino

Relatore
Prof. G. G. N. Angilella

Coordinatore Dottorato
Prof. Settimio Mobilio

a. a. 2011/2012

Contents

Introduction

Graphene is an atomically thick single layer of carbon atoms arranged according to a honeycomb lattice. Its quite recent discovery, due to Geim and Novoselov, and the realization of sufficiently large graphene flakes in the laboratory have stimulated an enormous outburst of both experimental and theoretical investigation [104, 105] . Indeed in 2010, Geim and Novoselov were awarded the Nobel Prize in Physics *for groundbreaking experiments regarding the two-dimensional material graphene* [51, 103].

The electronic band structure of graphene consists of two bands. In pristine graphene, they touch each other at the Fermi level in a linear, cone-like fashion at the so-called Dirac points K and K'. The low-energy electronic properties of graphene can be therefore mapped onto those of relativistic massless particles, thus allowing the observation of several effects predicted by quantum electrodynamics in a solid state system [28, 34]. This in turn determines most of the peculiar transport properties of graphene, including a minimal, finite conductivity in the clean limit at zero temperature [28], and a nearly constant optical conductivity over a large interval of frequencies [62, 138].

Transport measurements show that graphene has a remarkably high electron mobility at room temperature. Specifically, the electron mobility for graphene on a silicon dioxide (SiO_2) substrate is $\sim 10^5$ cm^2 V^{-1} s^{-1}, whereas for suspended graphene (*i.e.* without substrate) it is $\sim 10^6$ cm^2 V^{-1} s^{-1} [16, 17, 135]. These values are comparable with those obtained in more complex systems, as a modulation-doped field transistor (MODFET) [141]. Besides a high mobility, graphene presents a relatively high optical transparency, in addition to a remarkable flexibility, robustness and environmental stability. These properties make graphene an attractive material for applications also in photonics, optoelectronics and plasmonics [18, 78].

Graphene is also notable for its remarkable mechanical properties. In particular, recent *ab initio* calculations [87] as well as experiments [77] have demonstrated that graphene single layers can reversibly sustain elastic deformations as large as 20%. In microelectronics, the effect of strain is often used to modify the electronic and transport properties of materials in order to improve the performance of the devices [71]. In graphene, the application of strain (*e.g.* by stretching [19] or bending [77]) allows to tune its electronic properties [121, 123].

Recently, there has been a great interest towards the study and the realization of graphene-based electronic devices designed by a suitable tailoring of the electronic structure exploiting not only electric field effect but also applied strain. Both these techniques allow to tune the electronic properties of graphene in a reversible and clean way, *i.e.* without adding any source of disorder.

Therefore, an in-depth knowledge of the effects of the strain on graphene could be exploited to improve graphene-based devices. In this Thesis, we study in detail the influence that applied strain can have on several properties such as the optical properties, the plasmonic properties, and the transport properties. First of all, we focus on the strain-induced modifications of the optical conductivity. This quantity is observable by means of transmittance or reflectivity measurements [101], and it allows to recognize the features of the electronic structure which are tightly related to the lattice symmetry and that can be modified exploiting the strain. Moreover, we study the changes of the plasmonic spectrum when the system is under strain. Due to its low dimensionality and the large mean free path, graphene is an interesting material for applications in plasmonics [78]. Hence, the application of strain for tuning the plasmonic spectrum could have worthwhile technological implications. Finally, we devote the last part of the Thesis to the effects that local strain can induce on ballistic transport. Our study is motivated by the possibility of realizing basic elements for all-graphene electronics, which, by an engineering of the local strain profile, could be integrated on a single graphene sheet.

The outline of the Thesis is as follows.

In Chapter 1, we present an overview of the main properties of graphene. Such a review is far from being complete, but hopefully it should be sufficient to understand in which context this work is inserted.

In Chapter 2, we introduce the tight binding model, which we have used to describe the electronic structure of graphene. In addition, we show the Dirac approximation, which we have exploited to obtain analytical results about the low energy electronic properties of graphene.

In Chapter 3, we study the dependence of the electronic band structure and of the optical conductivity of a graphene single layer on the modulus and direction of applied uniaxial strain [110, 113]. In order to study the strain-induced modifications of the electronic structure we use a tight binding model. Despite its simplicity, it provides a lot of information about the electronic properties which are tightly related to the lattice symmetry [28]. First of all, using the tight binding model, we study whether it is possible to open a gap between conduction and valence bands due to uniaxial strain. The presence of a gap between the two electronic bands would allow new applications in nanoelectronics. Moreover, already within the tight binding model, we recover that in the unstrained graphene there is a Van Hove singularity corresponding to each electronic band [5, 28, 86]. Hence, we analyze how in graphene under uniaxial strain the number of Van Hove singularities can increase as a function of strain modulus and direction. Therefore, we propose that these features may be observed in the frequency dependence of the longitudinal optical conductivity in the visible range, as a function of strain modulus and direction, as well as of field orientation.

In Chapter 4, we study the dependence of the plasmonic dispersion relation of graphene on applied uniaxial strain [111, 114]. An in-depth analysis of the electronic bands allows to study purely electronic quantities, such as the plasmonic spectrum. In this Chapter, besides the electron correlation at the random phase approximation level, we also include local field effects specific for the honeycomb lattice. This improvement allows to take into account the Umklapp processes in the electron-electron scatterings, and consequently we can have information about the plasmonic spectrum for any wavevector and any energy.

In Chapter 5, starting from the tight binding model, we focus on the analytical study of the electronic properties at low energy [115, 119]. In particular, after deriving a general correspondence between linear response correlation functions in graphene with and without applied uniaxial strain, we study analytically the dependence on the strain modulus and direction of selected electronic properties, such as the plasmonic dispersion relation, the optical conductivity,

as well as the static magnetic and electric susceptibilities. Specifically, we study how the uniaxial strain can change the dispersion of the recently predicted transverse collective excitation which exhibits an anisotropic deviation from the photonic behavior [98], thus facilitating its experimental detection in strained graphene samples.

In Chapter 6, we consider the effects of uniaxial strain on ballistic transport in graphene, across single and multiple tunneling strain-induced barriers [116, 118]. We therefore study the angular dependence of the tunneling transmission across a single barrier, as well as on the conductivity and Fano factor across a single barrier and a superstructure of several, periodically repeated, such sharp barriers [13, 120]. Our model is generalized to the case of nonuniform barriers, where either the strain or the gate potential profiles may depend continuously on position. This should afford a more accurate description of realistic 'origami' nanodevices based on graphene [120], where 'foldings' are expected to embrace several lattice spacings.

Chapter 1

Graphene: Generalities

Graphene is the name given to a two-dimensional single layer of carbon atoms. It can be thought of as the building block of several sp^2-bonded carbon allotropes, ranging from three-dimensional graphite, to one-dimensional nanotubes, to zero-dimensional fullerenes [28].

Carbon is the sixth element in the Periodic Table. Thus, two of the six electrons fill the $1s$ shell. These ones are called core electrons, whereas the other ones are called valence electrons. In graphene, three ($2s$, $2p_x$, $2p_y$) of the four valence electrons get hybridized into sp^2 states. These electrons are extended along the layer, and they lead to a trigonal planar structure with the formation of a σ-bond between nearest-neighbor carbon atoms which are separated by 1.42 Å. These bonds are responsible for the robustness of the honeycomb lattice structure. The remaining two electrons, which occupy the p_z states in the free carbon atoms, form the (bonding) π band, known as valence band, and the (anti-bonding) π^* band, known as conduction band. In addition, these electrons are delocalized along the plane and they are responsible for transport and other long-range electronic properties of graphene. Despite its simplicity, single graphene layers have been obtained only recently (Geim and Novoselov, 2004 [104]) and it exhibits many appealing properties that make it a promising material for several technological applications [48].

1.1 The discovery of a two-dimensional crystal

Theoretically, graphene has been studied for more than sixty years. Specifically, graphene has been used for describing properties of various carbon-based materials. Already in 1947 Wallace published the first paper on the band structure of graphene [151]. In his work, Wallace suggested a description of the transport properties of graphite neglecting the out-of-plane degree of freedom. Thus, he used a graphene layer as a simple model to describe the electronic properties of graphite. Before its discovery in 2004, graphene was regarded as experimentally unrealizable [104], and it was thought merely as a theoretical object.

Indeed, already in the 30s, Landau and Peierls argued that strictly two-dimensional crystals were thermodynamically unstable and therefore could not exist at any finite temperature. They stated that a divergent contribution of the thermal fluctuations should lead to such displacements of the atoms that they become comparable to interatomic distances at $T \neq 0$. In addition, the existence of a two-dimensional crystal would be in contrast with a general theorem of Statistical Field Theory: the Mermin-Wagner theorem. According to this theorem no continuous symmetry can be spontaneously broken in dimensions $d < 3$ at any finite temperature [55]. In the case of a two-dimensional crystal, its formation would require the breaking of translational and rotational symmetries. Namely, unlike free space, a crystal is not invariant with respect to each element of the Euclidean group, which is the direct product of the continuous rotation group SO(2) and the continuous translational symmetry T_2 [144]. For this reason, for long time atomic monolayers have been known only as an integral part of three-dimensional structures, usually grown epitaxially either supported by a bulk substrate or embedded in a three-dimensional crystal [52]. Without a three-dimensional basis, two-dimensional materials were presumed not to exist, until 2004, when there was the experimental discovery of graphene [104] and other free-standing two-dimensional atomic crystals (for example, single-layer boron nitride [105]).

In 2004 Novoselov and Geim obtained, for the first time, single and few layers of graphene characterized by linear dimensions up to 10 μm on top of non-crystalline substrates [104]. Moreover, not long after samples of graphene were obtained as suspended membranes on a micro-fabricated scaffold in vacuum or air [97]. An important characteristic of these graphene

samples is their high crystal quality.

At first sight, it may seem as if that there is a violation of Mermin-Wagner theorem. But, in reality, the existence of graphene is compatible with Mermin-Wagner theorem. Indeed, two-dimensional crystals become intrinsically stable by gentle crumpling in the third dimension. Such ripples lead to a gain in elastic energy but suppresses thermal vibrations, which above a certain temperature can minimize the total free energy [44]. These ripples are observed both in suspended graphene, by electron diffraction measurements, and in graphene on substrate, by means of scanning tunneling microscopy (STM) measurements. Electron diffraction studies of free-standing graphene indicate the presence of an intrinsic rippling, which is characterized by a height on the order of ~ 1 nm over a lateral scale of $10 \div 25$ nm [97]. A comparable height variation has also been measured in several studies of graphene supported by insulating substrates [53, 140]. Hence graphene shows a slight extension in height, and so, since it is not exactly two-dimensional, and Mermin-Wagner theorem is not violated.

To obtain the first samples of graphene, Geim and Novoselov used a simple but effective procedure [105]. The technique used is called micro-mechanical cleavage, but also scotch-tape method. Let us remind that graphite is a layered material. It is made by weakly interacting ordered stacked graphene layers, which is the reason why the scotch-tape method works well. The top layer of an high quality graphite is removed by a scotch-tape, which is then pressed against the chosen substrate, thus depositing several flakes attached to it. Among the resulting flakes, single layers are usually found. A problem of this method is that most of the flakes are not graphene monolayers but thick graphite flakes (> 10 graphene layers). Therefore one should scan a huge area, typically ~ 1 cm^2, to find a micrometer-sized graphene monolayer. To use directly atomic force microscopy (AFM) or scanning electron microscopy (SEM) to search a graphene monolayers is unrealistic [103]. A crucial point is that a graphene monolayer is visible in an optical microscope if placed on a silicium (Si) wafer with a suitable thickness (300 nm) of silicon dioxide (SiO_2). In this way, it is possible to preliminarly identify thin flakes, but in order to be sure that a selected flake is a graphene layer a further analysis is performed by AFM or Raman microscopy [45].

1.2 Main physical properties of graphene

The enormous outburst of both experimental and theoretical investigation of graphene has been fueled, mainly, by numerous remarkable properties that make graphene an ideal candidate for applications in nanotechnologies. In this section we list several properties that make graphene such an attractive material.

1.2.1 Transport properties

Due to its lattice symmetry, graphene is a zero-gap semiconductor and is characterized by a low-energy linear dispersion relation [28]. In other words, the low-energy quasi-particles are massless and are characterized by an energy independent effective velocity[1]. The dynamics of the low-energy excitations is described by the Dirac-Weyl equation, which is used for massless fermions [136].

Intrinsic graphene disposes of no charge carriers. However, using electric doping it is possible to have either electrons or holes as charge carriers. Exploiting the electric field effect, a gate electrode can continuously change both the carrier density and type [104].

An attractive feature of graphene is its high carrier mobility at room temperature. Mobility in graphene on SiO_2 is generally of the order of $10000 \div 15000$ cm^2 V^{-1} s^{-1} [135]. Moreover, mobility on SiO_2 is almost a constant at low temperature ($T \ll 300\,\mathrm{K}$) and is limited by disorder. Disorder in exfoliated graphene on SiO_2 is mainly due to the charges trapped on the surface of the substrate or adsorbed on graphene. At high temperature $T \approx 300$ K, most properties of graphene are strongly dependent on temperature because of the optical phonons of the substrate [100].

In the case of suspended graphene, removing the substrate, one gets rid of extrinsic disorder and so mobility increases of an order of magnitude with respect to graphene on substrate. In suspended graphene it is possible to measure a mobility as high as 250000 cm^2 V^{-1} s^{-1} at low temperature and 120000 cm^2 V^{-1} s^{-1} at 240 K [16, 17]. Unlike in graphene on substrate, the mobility in suspended graphene is strongly temperature dependent also at low temperature [16]. These large values of the mobility mean that in suspended graphene the mean free path is of the

[1] See § 2.2 for details about the low-energy electronic structure.

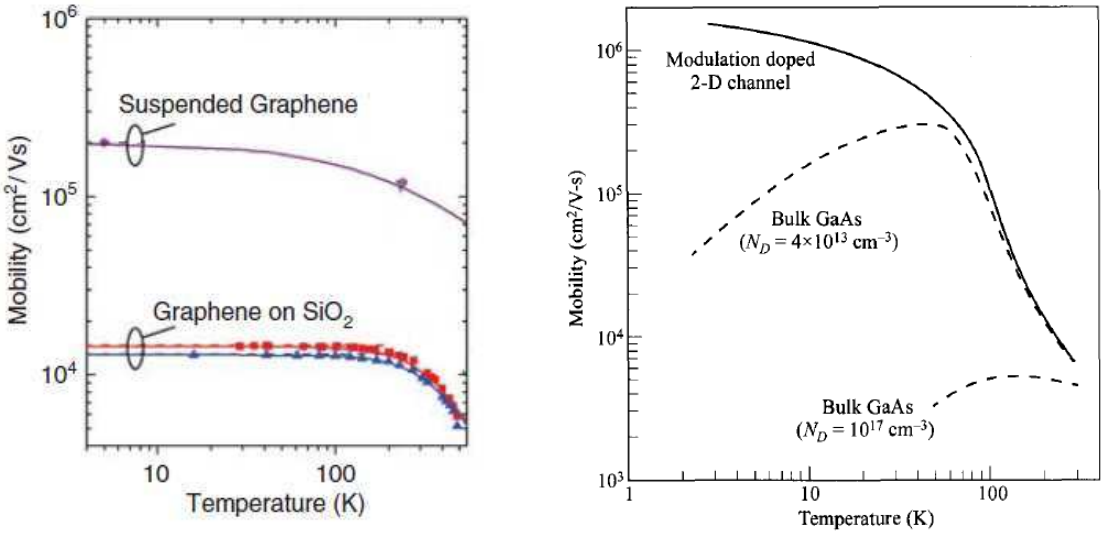

Figure 1.1: *Left*: Mobility as a function of temperature for graphene on SiO_2 at carrier density of 10^{11} cm^{-2} (blue and red), and suspended graphene at carrier density as 2×10^{11} cm^{-2} (purple). Adapted from [48]. *Right*: Comparison of mobility as a function of temperature for a MODFET and for bulk GaAs samples at different doping levels. Adapted from [141].

order of 1μm, which is comparable to the dimension of a typical device [16, 40].

For comparison, we consider the modulation-doped field effect transistor (MODFET). It is based on an heterostructure (*e.g.* AlGaAs and GaAs), where the wide energy gap material (*e.g.* AlGaAs) is doped and carriers diffuse to the intrinsic narrow bandgap layer (*e.g.* GaAs), at whose interface a two dimensional electron gas (channel) is formed [141]. The physical distance from channel and dopants allows to obtain an high mobility. This methodology is called modulation doping and it was invented by Horst Stormer at Bell Labs [38]. The modulation doping represents the best technique to obtain a very large value of electron mobility in a bulk system. At cryogenic temperatures it is possible to reach a mobility of the order of 10^6 cm^2 V^{-1} s^{-1}, but at temperatures above $T \approx 80$ K the mobility of these systems falls down to values of the order of 10^4 cm^2 V^{-1} s^{-1} [141]. Fig. 1.1 compares the mobility as a function of the temperature for graphene on SiO_2, suspended graphene and a MODFET. Here, one can see that at room temperature the mobility of graphene can be larger than that of a MODFET.

Due to the gapless energy spectrum, low carrier density and atomic thickness, it is possible to modify the profile of carriers along a graphene layer exploiting the electric field effect. For example, it is possible to realize a *p-n* or a *p-n-p* multi-polar configuration by electrostatic

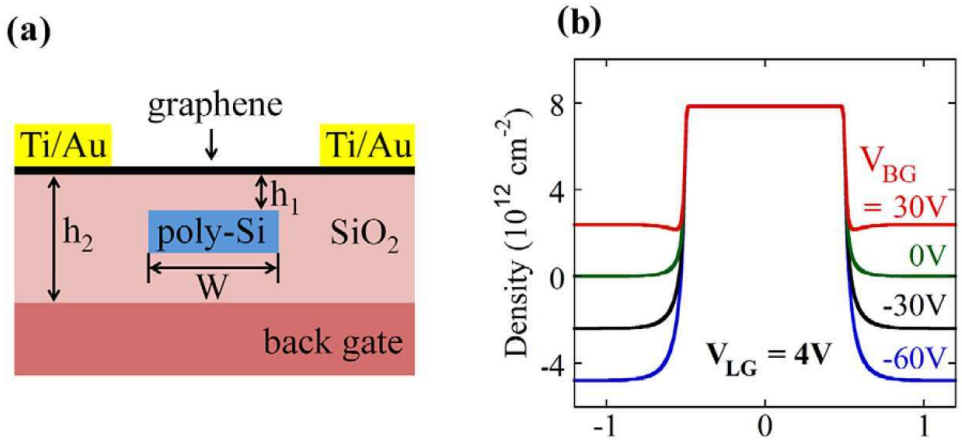

Figure 1.2: (a) Schematic *p-n-p* configuration of a graphene device. (b) Carriers density profile around the local-gate region fixed at $V_{LG} = 4$V for various values of the back-gate V_{BG}. Adapted from [102].

gates [157]. Let us see the case of Nam *et al.* [102], who have realized a *p-n-p* structure. Fig. 1.2 (a) schematically shows the *p-n-p* configuration. One observes that the back-gate (V_{BG}) is responsible of the electric doping in the *p*-regions whereas the local-gate (V_{LG}) is responsible of the electric doping in the *n*-region. From the bottom to the top, the device is made by a highly doped Si wafer (back-gate), an insulating SiO_2 layer where embedded inside there is a poly-silicon layer (local-gate) which is conductive by implantation of phosphorus ions. Finally, above the substrate there is a graphene monolayer with metal electrodes (Ti/Au). Moreover, Fig. 1.2 (b) shows the profile of carriers density at $V_{LG} = 4$ V for different values of V_{BG}. Where the density is positive, the region is *n*-doped, whereas where the density is negative the region is *p*-doped. In the case that we are taking into account the local-gate has a width of 130 nm, which is comparable to the mean free path of the sample. Indeed, Nam *et al.* have found ballistic and phase-coherent carrier transport. Fig. 1.3 shows the conductivity as a function of the local-gate V_{LG} at fixed back-gate V_{BG}. One observes an oscillating behavior due to the Fabry-Pérot interference between the two *p-n* interfaces. Morever, there is an important interest towards the theoretical study of the spectra and the electronic transport through differently doped regions, whose behavior differs from that of conventional two-dimensional electron gases [4, 10]. Recently, Rossi *et al.* [131] used a microscopic model where the disorder is dominated by charge impurities and transport properties are obtained fully quantum mechanically. In particular, they have studied the effects of disorder on transport through *p-n-p* junctions. The crossover from

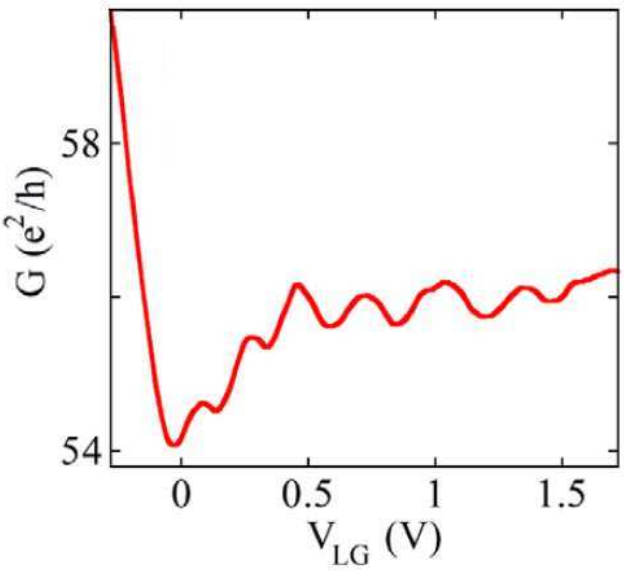

Figure 1.3: Conductance as a function of V_{LG} at fixed $V_{BG} = -40$V. Adapted from [102].

the ballistic transport governed by Klein tunneling, to the disordered diffusive transport is found to take place as the mean free path becomes of the order of the distance between the two *p-n* interfaces consistent with the experiments. These results demonstrate that the signatures of coherent transport are observable for impurity densities as high as 10^{12}cm^{-2}, then the quantum transport properties are sufficiently robust in graphene [34].

1.2.2 Optical properties

In addition to an high charge mobility, graphene is characterized by an excellent optical transparency. Such properties make graphene an attractive material for photonics and opto-electronic devices such as displays, touch screen, light-emitting diodes (LEDs), and solar cells [18].

Current transparent conductors are semiconductor-based: doped indium oxide (In_2O_3), zinc oxide (ZnO), tin oxide (SnO_2), or ternary compounds based on their combinations [18]. The most widely used material is indium tin oxide (ITO), a doped *n*-type semiconductor composed of $\approx 90\%$ In_2O_3 and $\approx 10\%$ SnO_2 [63]. ITO is commercially available with trasmittance

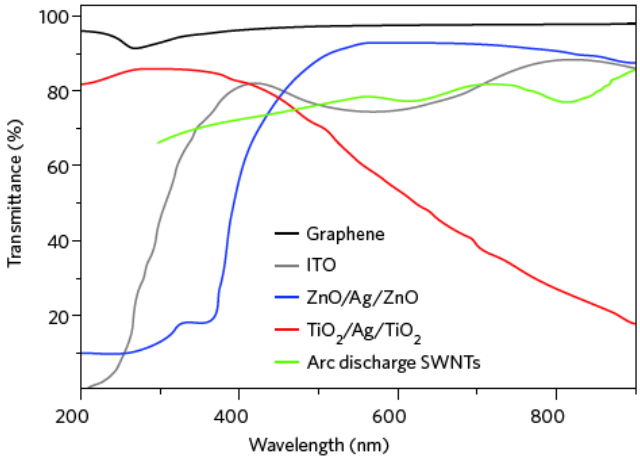

Figure 1.4: Transmittance for different transparent conductors: graphene, single-walled carbon nanotubes (SWNTs), ITO, ZnO/Ag/ZnO and TiO_2/Ag/TiO_2. Adapted from [18].

$T \approx 80\%$. Moreover, ITO is brittle for applications involving bending, such as touch screens and flexible displays. For this reason, there is interest in the research of new transparent conductor materials with improved performance. Metal grids, metallic nanowires or other metal oxides have been explored as alternatives. Nanotubes and graphene are promising materials. In particular, by the comparison in Fig. 1.4 one can see that graphene films have a higher trasmittance over a wider wavelength range than single-walled carbon nanotube (SWNT) films, thin metallic films, and ITO [18].

Despite its thickness, Nair *et al.* have observed that graphene absorbs a significant fraction ($\pi\alpha \approx 2.3\%$, where α is the fine structure constant) of incident light, from the near-infrared to violet [101]. In Fig. 1.5 (Left) we observe an aperture of the SiO_2 substrate that it is only partially covered by suspended graphene, so that the opacities of different regions (with or without graphene) can be compared. Fig. 1.5 (Right) shows transmittance measurements on monolayer graphene obtained by standard spectroscopy using a xenon lamp as a light source (blue circles) and by optical microscopy (red squares). Both experimental data sets are in agreement and yield a constant value for transmittance ($\approx 1 - \pi\alpha$) in the energy range taken into account [101].

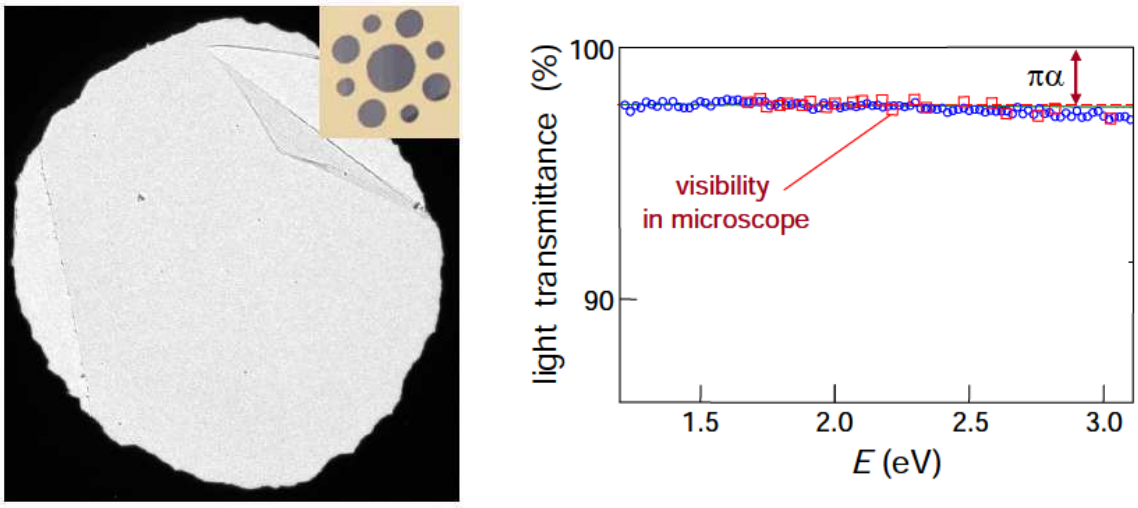

Figure 1.5: *Left*: Transmission electron microscopy (TEM) micrograph of a 30μm aperture covered by graphene. *Right*: Transmittance spectrum of graphene over a range of photon energies from the near-infrared to violet. The blue open circles show the data obtained using standard spectroscopy. The red squares are the spectrum measured using an optical microscope. The red line indicates the opacity of $\pi\alpha$. Adapted from [101].

1.2.3 Plasmonic properties

It has been said already that it is possible to modify the type and density of charge carriers in graphene using an external voltage. This feature can be effectively exploited in plasmonics. A doped graphene monolayer can sustain low-energy plasmons which are tunable by means of the electric field effect. In particular, plasmons in doped graphene enable low losses and significant wave localization of the light in the terahertz (THz) and infrared (IR) domains [72]. These properties make graphene relevant for possible applications in plasmonics.

The recent attraction towards plasmonics is immediately motivated by the constant effort towards improving the performance of devices. A limitation to an improvement of the speed of digital circuits is due to electronic interconnections. A possible solution is offered by photonics by implementing faster communication systems based on optical fibers and photonic circuits [107]. However, the replacement of electric circuits by photonic ones is hindered by the low level of integration and miniaturization of the photonic components. The wavelength of light used in photonic circuits is of the order of 1000 nm, hence it is larger than the typical dimensions of an electronic circuit. Thus, if the dimensions of the optical components should be reduced

further and become comparable with the wavelength of light, propagation would be obstructed by optical diffraction. One way to avoid this obstacle is suggested by plasmonics. Surface plasmons enable to confine light to within very small dimensions, as electromagnetic waves can be trapped near the surface due to their interaction with the electron plasma. Hence, the idea is to use plasmonic guides instead of optical fibers.

To date, the noble metals are the materials mainly investigated for developments in plasmonics, but they are hardly tunable and have large ohmic losses that limit their applicability. In graphene both characteristics are improved, and the confinement of plasmons is much stronger than that of surface plasmons in metals due to the two-dimensional nature of graphene. In particular, graphene plasmons are confined to volumes $\approx 10^6$ times smaller than the diffraction limit, thus facilitating strong light-matter interactions [78]

In aluminium, which is a relatively absorbing metal, the propagation length is 2 mm at a wavelength of 500 nm, whereas in silver, which is a low loss metal, at the same wavelength the propagation length is 20 mm. For slightly longer wavelengths, such as 1.55 mm, the propagation length is around 1 mm [8], whereas in graphene, the propagation distance can reach values well above 100 plasmon wavelengths [72, 78].

1.2.4 Mechanical properties

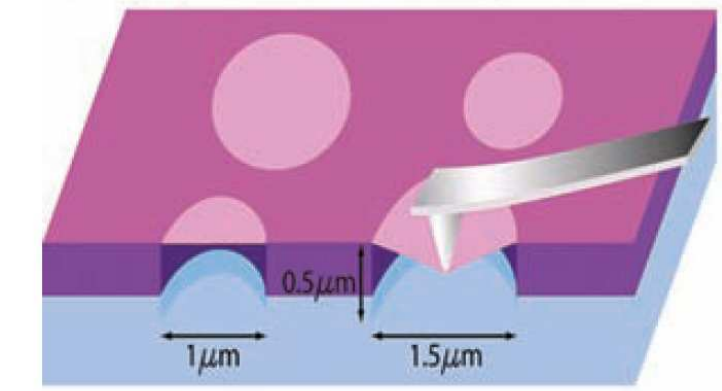

Figure 1.6: Scheme of AFM nanoindentation on suspended graphene monolayer. Adapted from [82].

In addition to its electronic properties, graphene is a remarkable material also for its mechanical properties. Generally, carbon nanostructures characterized by sp^2 bonds, such as carbon

nanotubes, show an exceptional resistance to mechanical stress, notwithstanding low dimensionality [158]. Lee *et al.* have measured the mechanical properties of graphene using atomic force microscope (AFM) nanoindention, this technique has been used to study a single layer suspended over an aperture of a substrate [82]. The experimental apparatus consists of an array of circular holes in a substrate, on top of which graphene monolayers have been deposited. Once a graphene sample placed over an hole was detected, the mechanical properties of the suspended membrane have been measured by indenting with AFM. Fig. 1.6 schematically shows the layout of the experiment. The measured breaking strength of graphene is 42 N m^{-1}. In order to compare the mechanical properties of graphene with those of other three-dimensional materials, Lee *et al.* consider a graphene sheet as a three-dimensional slab having an effective height equal to the distance between two adjacent graphene planes in graphite ($h = 3.35$ Å). Thus the Young modulus of graphene is $E = 1.0$ TPa and the third-order elastic stiffness is $D = -2.0$ TPa. These values allow to list graphene among of the strongest materials ever measured [82].

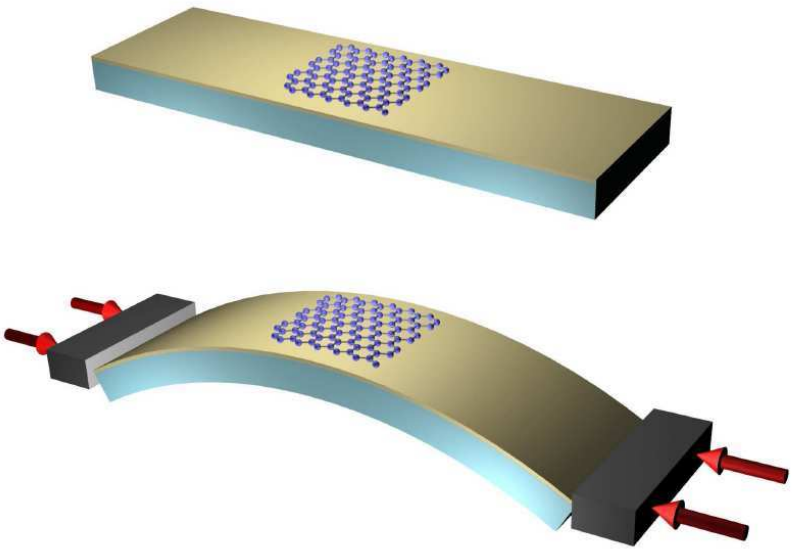

Figure 1.7: Schematic apparatus to induce strain in graphene by means of a stretchable substrate. Adapted from [99].

Another methodology to study graphene under strain is to transfer it onto a flexible substrate, so that one can apply controllable (uniaxial or biaxial) strain to graphene by applying stress on the supporting substrate (Fig. 1.7) [77, 99]. Exploiting this technique, Kim *et al.* have found

that graphene can reversibly sustain elastic deformations as large as 20% [77]. Theoretical results are in agreement with these measurements. Indeed, according to *ab initio* calculations the graphene lattice is stable with respect to uniaxial deformations up to around 20% [87].

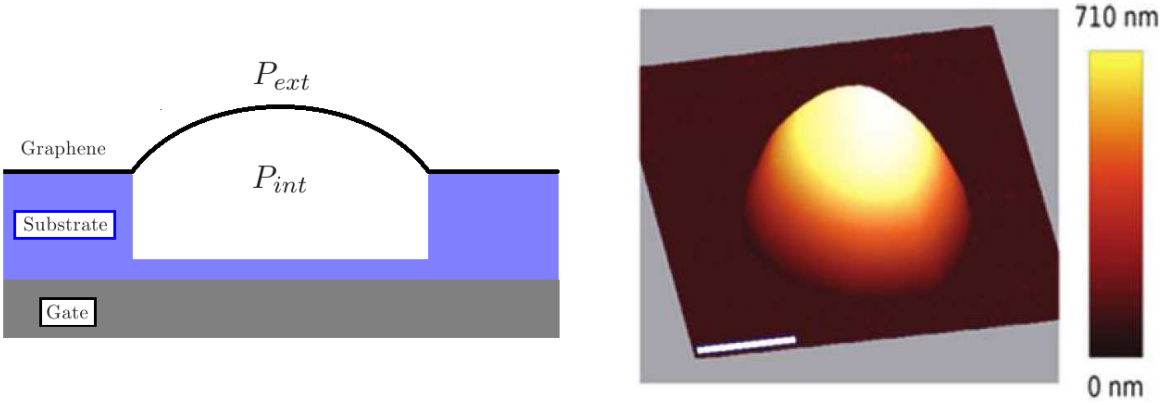

Figure 1.8: *Left*: Scheme of the methodology to induce strain in graphene using a pressure difference ($\Delta P = P_{int} - P_{ext}$). *Right*: AFM image of a single layer graphene bubble. The lateral scale is 4μm. Adapted from [160].

Graphene behaves as an impermeable membrane and can support pressure differences larger than 1 atm. Exploiting this property it is possible to deform graphene [24, 160]. Fig. 1.8 (Left) shows a scheme of the experimental setup, where the impermeability of graphene is used. There is a graphene layer suspended over a well in a SiO_2 substrate. The graphene membrane is clamped to the substrate through the Van der Waals interaction. Inside the well there is a gas at pressure P_{int}, whereas outside the pressure P_{ext} is different so the difference of pressure ($\Delta P = P_{int} - P_{ext}$) allows to have a controlled deformation of graphene. A similar methodology to have the desired amount of strain in graphene is obtained by using a gate in a configuration like in Fig. 1.8. In this case an electric field induces an electron concentration in graphene and exerts on it a pressure of electrostatic nature [47].

Uniaxial or biaxial strain induces modifications not only in the phonon spectrum but also in the electronic spectrum, and can be measured directly using Raman spectroscopy [99, 160]. In graphene, Raman measurements give information not only about phonons but also about the electronic properties since graphene is a non-polar crystal, and so Raman scattering involves electronic excitations as intermediate states [9].

Material science teaches that the presence of strain can significantly affect the device perfor-

mance. Indeed, sometimes strain is intentionally applied to improve mobility, as in the strained silicon technology, which is used in modern microelectronics [84]. Recently, an appealing challenge is to exploit the modifications of the electronic structure due to the strain to realize an all-graphene circuit where all the elements are made of graphene with different amount and types of strain [120, 160]. Further methodologies to accomplish this challenge and to have a controlled strain profile in a graphene sample are obtained by means of an appropriate geometrical pattern in a homogeneous substrate, or by means of a heterogeneous substrate so that each region interacts with graphene in a different way [89, 125, 149]. Among the experimental methodologies to realize strain superstructures in graphene, one is based on the relatively large and negative thermal coefficient of graphene (which is around 5 times larger than that of bulk graphite in the basal plane). Bao *et al.* [6] have realized experimentally a strain superlattice in graphene, it is possible to manipulate the orientation and dimensions of ripples exploiting the boundary conditions and the difference in the thermal expansion coefficients between graphene and the substrate. The graphene membrane is annealed up to 700 K, so any pre-existing ripple disappears. After this phase, the sample is cooled and the graphene layer exhibits ordered ripples, whose geometry depends on the boundary conditions. In particular, the necessary tension to produce this structure is due to the different sign of the thermal coefficients of graphene and substrate [6].

Such recent ideas to exploit mechanical modifications to realize an all-graphene device is attractive as strain engineering would allow to tailor electronic properties, in a controlled fashion, without the introduction of disorder [120].

Chapter 2

Graphene: Model

Graphene is characterized by an honeycomb lattice. This lattice is not a Bravais lattice and it can be described as a triangular lattice with a basis of two carbon atoms per unit cell [5, 132]. Hence, the honeycomb lattice is equivalent to two interpenetrating triangular sublattices (A and B, say), both sublattices being shifted with respect to each other. The lattice of graphene is characterized by hexagonal symmetry. The space group of graphene is therefore the D_{6h}^1 group [39]. Moreover, since the space group of graphene is symmorphic, it can be expressed as the semi-direct product of the discrete translation group T_2 and the point hexagonal symmetry group D_{6h}.

Fig. 2.1 shows a partion of the direct lattice of graphene, where the shaded region is the unit cell. The basis vectors are defined as:

$$\mathbf{a}_1 = \frac{a}{2}\left(3, \sqrt{3}\right), \quad \mathbf{a}_2 = \frac{a}{2}\left(3, -\sqrt{3}\right), \tag{2.1}$$

where $a \approx 1.42$ Å is the distance between two nearest neighbor carbon atoms. Each carbon atom has three nearest neighbors, for example a generic carbon atom of the A sublattice is connected to its nearest neighbors by the vectors:

$$\boldsymbol{\delta}_1 = \frac{a}{2}\left(1, \sqrt{3}\right), \tag{2.2a}$$

$$\boldsymbol{\delta}_2 = \frac{a}{2}\left(1, -\sqrt{3}\right), \tag{2.2b}$$

$$\boldsymbol{\delta}_3 = a\left(-1, 0\right). \tag{2.2c}$$

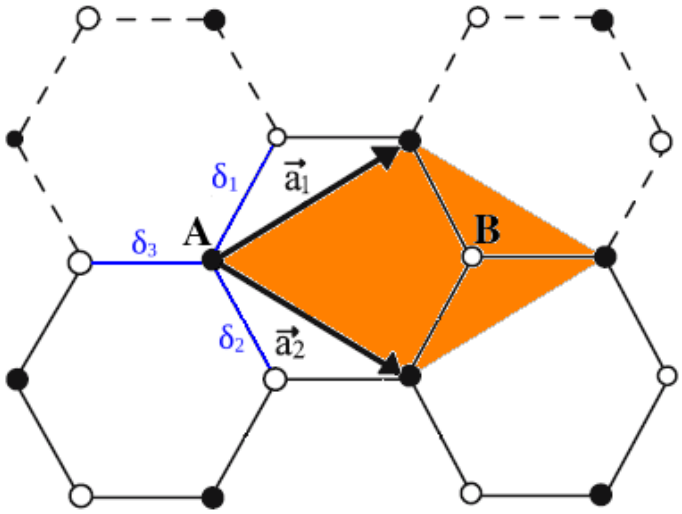

Figure 2.1: Direct lattice of graphene. The shaded region is the unit cell and it is identified by the basis vectors $\mathbf{a}_1$ and $\mathbf{a}_2$. The blue vectors $\boldsymbol{\delta}_\ell$ $(\ell = 1, 2, 3)$ connect a carbon atom with its nearest neighbors. Adapted from [39].

In the case of graphene, the basis vectors of the reciprocal space are given by

$$\mathbf{b_1} = \frac{2\pi}{3a}\left(1, \sqrt{3}\right) \qquad \mathbf{b_2} = \frac{2\pi}{3a}\left(1, -\sqrt{3}\right). \tag{2.3}$$

The space symmetry properties of the direct lattice are present also in reciprocal lattice. Indeed, in the case of graphene, the reciprocal lattice and the direct lattice are identical up to a rotation of $\pi/2$, how one can see in Fig. 2.2.

2.1 Tight binding model

Once defined the graphene lattice, we can study the electronic band structure. In a generic perfect crystal the Hamiltonian of the system has the following structure:

$$\mathcal{H}_{tot} = T_{el} + T_{nucl} + V_{el-el} + V_{nucl-nucl} + V_{el-nucl} + C_{rel}. \tag{2.4}$$

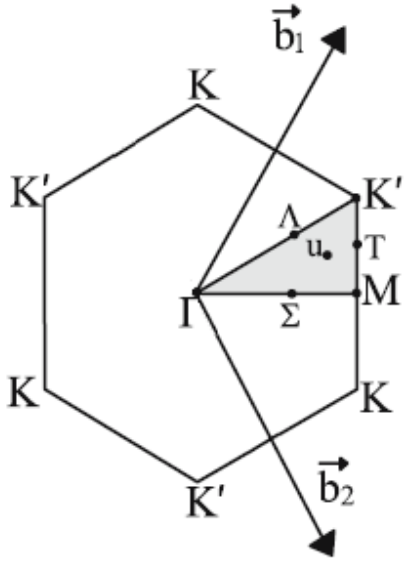

Figure 2.2: First Brillouin zone (1BZ), where Γ, M, K e K' are the high symmetry points, Σ, T e Λ are points located on high symmetry lines, and u is a generic point inside the 1BZ. Adapted from [39].

In order, there are the kinetic energy of the electrons, the kinetic energy of nuclei, the interaction between the electrons, the interaction between the nuclei, the interaction between electrons and nuclei, and finally the relativistic correlation terms (*e.g.* spin-orbit term). In general, the many-particle Hamiltonian in Eq. (2.4) cannot be solved without a large number of simplifications. The first approximation is to separate the electrons into two groups: valence electrons and core electrons. The core electrons are mostly localized around the nuclei, so they are considered as a part of the nuclei (globally they are called ion cores). Hence, when considering an electron, we will be usually referring to the valence electrons. The second approximation is called the Born-approximation. According to this approximation, the dynamics of the electrons is separated from the dynamics of the ions. In the equation of motion for the electrons we consider that ions are frozen in their equilibrium positions. Hence, the Hamiltonian for the electrons can be written in this form:

$$\mathcal{H}_{el} = T_{el} + V_{el-el} + V_{el-ion}. \tag{2.5}$$

To diagonalize the Hamiltonian $\mathcal{H}_{el}$ is still a prohibitive problem. It is helpful to use a further drastic approximation known as the mean field approximation. It is assumed that every electron

'sees' the same average potential U_c [159]. Using this approximation the electrons are treated as non-interacting particles and the single-particle Hamiltonian has the following form in the coordinate space:

$$\mathcal{H} = -\frac{\hbar^2\nabla^2}{2m} + U_c(\mathbf{r}), \tag{2.6}$$

where U_c is called crystalline potential. The Hamiltonian $\mathcal{H}$ consists of two terms: the first term is the kinetic term and is invariant under every spatial symmetry operation, the second term is the crystalline potential and is invariant under each operation of the space group of the crystal. Hence, globally the Hamiltonian $\mathcal{H}$ is invariant under each operation of the space group of the crystal.

In order to describe the electronic band structure we will use the tight binding approximation. The Hamiltonian obtained following this approach has the form expressed in Eq. (2.6).

For every sp^2 allotropic form of carbon with long range order (*i.e.* nanotubes, graphene, graphite) a calculation of the electronic bands based on the tight binding approximation, despite its simplicity, provides a lot of information about the electronic properties [132]. We assume that the crystalline potentials can be written as the sum of identical potentials centered around each atomic site:

$$U_c(\mathbf{r}) = \sum_{\alpha=A,B}\sum_{j} U_{ion}(\mathbf{r} - \mathbf{R}_{j\alpha}), \tag{2.7}$$

where $\mathbf{R}_{j\alpha}$ identifies site j of sublattice α ($\alpha = A, B$). Using the basis vector defined in Eq. (2.1), we can write a generic vector of the A sublattice as

$$\mathbf{R}_{jA} = j_1\mathbf{a}_1 + j_2\mathbf{a}_2, \tag{2.8}$$

where $j = (j_1, j_2)$ is an integer pair, whereas we write a generic vector of the sublattice B as

$$\mathbf{R}_{jB} = j_1\mathbf{a}_1 + j_2\mathbf{a}_2 + \boldsymbol{\delta}_3, \tag{2.9}$$

where we have used the shift vector $\boldsymbol{\delta}_3$ defined in Eq. (2.2c). The sublattice variable that can assume either value A or B is called pseudospin, by analogy with the z-projection of the spin $1/2$ of the electron.

We assume to know the eigenfunction $\phi(\mathbf{r})$ of the following atomic Hamiltonian

$$\mathcal{H}_{ion} = -\frac{\hbar^2\nabla^2}{2m} + U_{ion}(\mathbf{r}), \tag{2.10}$$

$$\mathcal{H}_{ion}\phi(\mathbf{r}) = \epsilon\phi(\mathbf{r}). \tag{2.11}$$

Using the wave function $\phi(\mathbf{r})$, we define a set of Bloch wave functions as

$$\psi_\alpha(\mathbf{k};\mathbf{r}) = \frac{1}{\sqrt{N}}\sum_j e^{i\mathbf{k}\cdot\mathbf{R}_{j\alpha}}\phi(\mathbf{r}-\mathbf{R}_{j\alpha}) \tag{2.12}$$

where α is the pseudospin and N is the number of unit cell in the crystal. We have defined the Bloch wave function in terms of a linear combination of atomic wave function. The atomic wave functions are written in Dirac notation as

$$\langle\mathbf{r}|j\alpha\rangle = \phi(\mathbf{r}-\mathbf{R}_{j\alpha}), \tag{2.13}$$

where the generic $\phi(\mathbf{r}-\mathbf{R}_{j\alpha})$ is the eigenfunction of the atomic Hamiltonian Eq. (2.10) centered around the site j of the sublattice α. After a manipulation, one can rewrite the wave functions in Eq. (2.12) as the product of a plane wave function and a periodic function

$$\psi_\alpha(\mathbf{k};\mathbf{r}) = e^{i\mathbf{k}\cdot\mathbf{r}}\mathcal{U}_{\alpha\mathbf{k}}(\mathbf{r}), \tag{2.14}$$

and

$$\mathcal{U}_{\alpha\mathbf{k}}(\mathbf{r}) = \frac{1}{\sqrt{N}}\sum_j e^{-i\mathbf{k}\cdot(\mathbf{r}-\mathbf{R}_{j\alpha})}\phi(\mathbf{r}-\mathbf{R}_{j\alpha}). \tag{2.15}$$

The wave functions just defined span the subspace $\mathcal{S}_{TB}$ of the Hilbert space where we will apply the Ritz variational method [96]. Moreover, using this set of basis we neglect any z-extension of the electronic wave functions. For each wave-vector $\mathbf{k}$ of the 1BZ we must find the extrema of the expectation value of the energy, *i.e.*

$$\delta\frac{\langle\lambda\mathbf{k}|\mathcal{H}|\lambda\mathbf{k}\rangle}{\langle\lambda\mathbf{k}|\lambda\mathbf{k}\rangle} = 0, \tag{2.16}$$

where the trial state has the following form:

$$|\mathbf{k}\lambda\rangle = u^{A}_{\mathbf{k}\lambda}|\mathbf{k}A\rangle + u^{B}_{\mathbf{k}\lambda}|\mathbf{k}B\rangle. \tag{2.17}$$

In the Hamiltonian that we are taking into account there is no spin dependent term, hence the z-component of spin is a good quantum number that we can neglect in the calculations.

For each wave-vector $\mathbf{k}$ we define the generic element of the transfer integral matrix as

$$H_{\alpha\beta}(\mathbf{k}) = \langle\alpha\mathbf{k}|\mathcal{H}|\beta\mathbf{k}\rangle. \tag{2.18}$$

Similarly, we define the generic element of the overlap integral matrix as:

$$S_{\alpha\beta}(\mathbf{k}) = \langle\alpha\mathbf{k}|\beta\mathbf{k}\rangle, \tag{2.19}$$

where both the α and β indices can assume value either A or B. Both matrices are Hermitian, square, and of order 2. Since the distinction between A and B carbon atoms is only mathematical, and not physical, one finds the following equalities between diagonal elements

$$H_{AA}(\mathbf{k}) = H_{BB}(\mathbf{k}), \tag{2.20a}$$

$$S_{AA}(\mathbf{k}) = S_{BB}(\mathbf{k}). \tag{2.20b}$$

Hence there are only two independent elements for each matrix.

In this case, the variational problem (2.16) is equivalent to solve the following generalized eigenvalue problem

$$H(\mathbf{k})\mathbf{u}_{\mathbf{k}\lambda} = E_{\mathbf{k}\lambda}S(\mathbf{k})\mathbf{u}_{\mathbf{k}\lambda}. \tag{2.21}$$

The solution of this problem gives eigenstates and eigenenergies for each wave-vector $\mathbf{k}$. The eigenenergies we obtain have the following form

$$E_{\lambda}(\mathbf{k}) = \frac{-\varepsilon_1 + (-1)^{\lambda}\sqrt{\varepsilon_1^2 - 4\varepsilon_2\varepsilon_0}}{2\varepsilon_2}, \tag{2.22}$$

where

$$\begin{aligned}\varepsilon_0 &= H_{AA}^2(\mathbf{k}) - |H_{AB}(\mathbf{k})|^2,\\ \varepsilon_1 &= H_{AB}^*(\mathbf{k})S_{AB}(\mathbf{k}) + H_{AB}(\mathbf{k})S_{AB}^*(\mathbf{k}) - 2S_{AA}(\mathbf{k})H_{AA}(\mathbf{k}),\\ \varepsilon_2 &= S_{AA}^2(\mathbf{k}) - |S_{AB}(\mathbf{k})|^2. \end{aligned} \tag{2.23}$$

In Eq. (2.23) $\lambda = 1$ refers to the valence band, and $\lambda = 2$ refers to the conduction band.

The elements of both the transfer integral matrix and the overlap integral matrix can be expanded in the tight binding basis as

$$H_{\alpha\beta}(\mathbf{k}) = \frac{1}{N}\sum_{j,j'} e^{-i\mathbf{k}\cdot(\mathbf{R}_{j\alpha}-\mathbf{R}_{j'\beta})}\langle j\alpha|\mathcal{H}|j'\beta\rangle, \tag{2.24}$$

$$S_{\alpha\beta}(\mathbf{k}) = \frac{1}{N}\sum_{j,j'} e^{-i\mathbf{k}\cdot(\mathbf{R}_{j\alpha}-\mathbf{R}_{j'\beta})}\langle j\alpha|j'\beta\rangle. \tag{2.25}$$

Exploiting the discrete translational invariance we can order the terms of the expansions in Eq. (2.24) and in Eq. (2.25) according to the distance from the origin of the lattice. We have chosen the origin $\mathbf{0} = (0,0)$ as belonging to sublattice A. Thus, one finds that the diagonal elements can be written as

$$\mathcal{H}_{AA}(\mathbf{k}) = \epsilon + \langle \mathbf{0}A|\Delta U_c|\mathbf{0}A\rangle + \sum_{j\neq\mathbf{0}} e^{i\mathbf{k}\cdot\mathbf{R}_j}\langle \mathbf{0}|\mathcal{H}|jA\rangle, \tag{2.26}$$

where

$$\langle \mathbf{r}|\Delta U_c|\mathbf{r}'\rangle = [U_c(\mathbf{r}) - U_{ion}(\mathbf{r})]\,\delta(\mathbf{r}-\mathbf{r}'),$$

and

$$S_{AA}(\mathbf{k}) = 1 + \sum_{j\neq\mathbf{0}} e^{i\mathbf{k}\cdot\mathbf{R}_j}\langle \mathbf{0}A|jA\rangle. \tag{2.27}$$

Similarly, we obtain the expansion for the off-diagonal elements

$$H_{AB}(\mathbf{k}) = \sum_j e^{i\mathbf{k}\cdot(\mathbf{R}_j+\boldsymbol{\delta}_3)}\langle \mathbf{0}A|\mathcal{H}|jB\rangle, \tag{2.28}$$

$$S_{AB}(\mathbf{k}) = \sum_j e^{i\mathbf{k}\cdot(\mathbf{R}_j+\boldsymbol{\delta}_3)}\langle \mathbf{0}A|jB\rangle. \tag{2.29}$$

The $2p_z$ electrons form the conduction band (π^*) and the valence band (π). In a hydrogen-like model the $2p_z$ wave-function is real and invariant with respect to the rotation around the $\hat{z}$-axis. Assuming that $\phi(\mathbf{r})$ has these latter properties, we can formally expand the elements of the transfer integral matrix up to nearest neighbor terms. One finds for the diagonal elements the following expression

$$H_{AA}(\mathbf{k}) = t^{(0)} + \mathcal{O}(t^{(2)}), \tag{2.30}$$

where

$$t^{(0)} = \langle \mathbf{0}A|\mathcal{H}|\mathbf{0}A\rangle = \epsilon + \langle \mathbf{0}A|\Delta U_c|\mathbf{0}A\rangle, \tag{2.31}$$

and one finds for the off-diagonal elements the following expression

$$H_{AB}(\mathbf{k}) = t^{(1)}\gamma_{\mathbf{k}} + \mathcal{O}(t^{(3)}), \tag{2.32}$$

where

$$t^{(1)} = \langle \mathbf{0}A|\mathcal{H}|\mathbf{0}B\rangle, \tag{2.33}$$

and we have introduced the complex structure function defined as

$$\gamma_{\mathbf{k}} = \sum_{l=1}^{3} e^{i\mathbf{k}\cdot\boldsymbol{\delta}_l}. \tag{2.34}$$

Since the energy bands are defined up to a constant, we fix this constant by setting $t_0 = 0$. With this choice of truncation of the expansion of the transfer integral matrix elements, we have only one hopping parameter. Thus we redefine the nearest neighbor hopping parameter as

$$t = t^{(1)}. \tag{2.35}$$

Similarly, we can expand the overlap integral matrix elements up to nearest neighbor terms and thus one finds

$$S_{AA}(\mathbf{k}) = 1 + \mathcal{O}(s^{(2)}), \tag{2.36}$$

$$S_{AB}(\mathbf{k}) = s^{(1)}\gamma_{\mathbf{k}} + \mathcal{O}(s^{(3)}), \tag{2.37}$$

where

$$s^{(1)} = \langle \mathbf{0}A|\mathbf{0}B\rangle. \tag{2.38}$$

Also for the overlap integral matrix elements only one parameter remains, thus the nearest neighbor overlap parameter is redefined as

$$s = s^{(1)}. \tag{2.39}$$

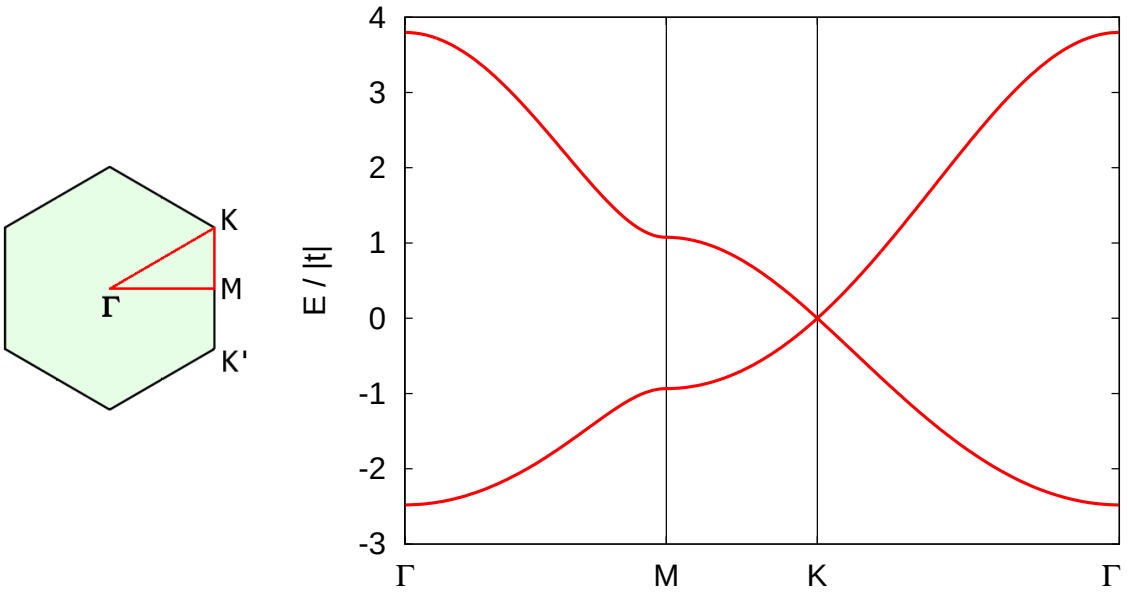

Figure 2.3: *Left*: High symmetry path Γ-M-K-Γ in the 1BZ. *Right*: Conduction band and valence band along the high symmetry path. The unit of energy is the absolute value of the hopping parameter t, and the overlap parameter is fixed at $s = 0.07$.

Following this choice of truncation of the expansions of the matrix of the tight binding model, we can write explicitly the electronic bands thus obtained as

$$E_\lambda(\mathbf{k}) = \frac{(-1)^{\lambda+1} t|\gamma_\mathbf{k}|}{1 + (-1)^{\lambda+1} s|\gamma_\mathbf{k}|}, \tag{2.40}$$

where $E_1(\mathbf{k})$ is the dispersion relation of the valence band, whereas $E_2(\mathbf{k})$ is the dispersion relation of the conduction band.

Conduction and valence bands touch each other at the corners of the 1BZ, *i.e.* at the K and

K' points,

$$K = \frac{2\pi}{3\sqrt{3}a}\left(\sqrt{3}, 1\right), \tag{2.41a}$$

$$K' = \frac{2\pi}{3\sqrt{3}a}\left(\sqrt{3}, -1\right). \tag{2.41b}$$

This result does not depend on the particular approximation chosen but is an intrinsic property of the electronic structure of graphene. The band degeneracy at the K and K' points is related to the hexagonal symmetry of graphene. In terms of group theory, one says that there is an essential degeneracy.

Another intrinsic property of the electronic structure of graphene is the presence of saddle points at the midpoints of the sides of the 1BZ for both the conduction and the valence band. The positions of the midpoints of the sides of the 1BZ are given by:

$$M_1 = \frac{2\pi}{3a}\left(-\frac{1}{2}, -\frac{\sqrt{3}}{2}\right), \tag{2.42a}$$

$$M_2 = \frac{2\pi}{3a}\left(-\frac{1}{2}, \frac{\sqrt{3}}{2}\right), \tag{2.42b}$$

$$M_3 = \frac{2\pi}{3a}\left(1, 0\right). \tag{2.42c}$$

The zero gradient of both electronic bands at the edge midpoints M_ℓ is due to the time-reversal symmetry and the inversion axis symmetry [39]. Moreover, since a honeycomb lattice is symmetric with respect to $\pm 2\pi/3$ rotations each electronic band assumes the same value at each edge midpoint. Thus, there is a degeneracy at the edge midpoints M_ℓ.

At zero temperature ($T = 0$), since there are two (valence) electrons for each unit cell, the valence band is completely filled, whereas the conduction band is totally empty. Fig. 2.3 shows both the electronic bands evaluated along the high symmetry path in the 1BZ. One recovers the features that we have just listed, and in addition one sees that conduction and valence band have no overlap and there is no gap. Hence, one says that graphene is a zero-gap semiconductor.

We do not treat directly the single-particle Hamiltonian $\mathcal{H}$. In other words, we do not find the tight binding parameters by the calculation of any matrix element. We have obtained an analytic expression for the electronic bands taking into account the symmetry properties of the

lattice. With our choice of truncation we have two parameters, whose values have to be fixed. A suitable solution is to choose these values in agreement with experimental measurements or with *ab initio* calculations.

In the case of graphene, the most common practice is to fit the tight binding dispersion around the K and K' points [129]. This approach is excellent to describe the low-energy electronic excitations. In our case we have chosen the tight binding parameters that better fit to *ab initio* calculations, hence one finds [129]:

$$t = -2.8 \text{ eV}, \tag{2.43a}$$

$$s = 0.07. \tag{2.43b}$$

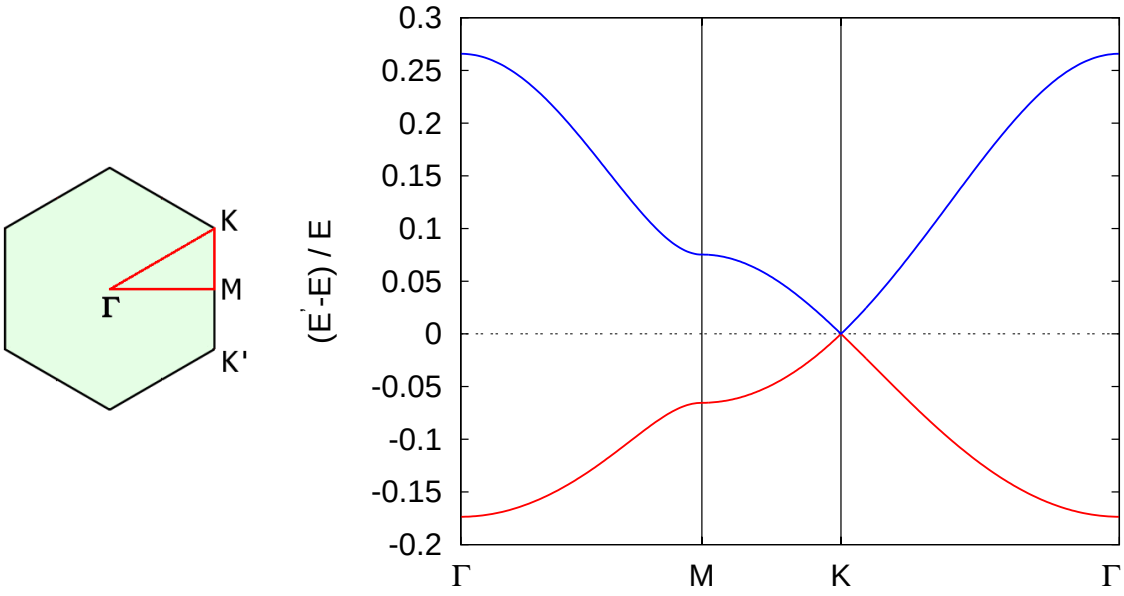

Figure 2.4: *Left*: High symmetry path Γ-M-K-Γ in the 1BZ. *Right*: The blue line curve is the relative difference $[E_2'(\mathbf{k}) - E_2(\mathbf{k})]/E_2(\mathbf{k})$ between conduction band neglecting s parameter $E_2'(\mathbf{k})$ and taking into account it $E_2(\mathbf{k})$. Similarly, the red line curve is the relative difference $[E_1'(\mathbf{k}) - E_1(\mathbf{k})]/E_1(\mathbf{k})$ between valence band without and with the overlap parameter. Both curves are evaluated along the high symmetry path in the 1BZ.

The hopping parameter t is the energy scale of the model. For example, both the energy bandwidths and the low-energy Fermi velocity are related to this parameter. The overlap parameter s is a dimensionless term, a non-zero overlap parameter ($s \neq 0$) leads to the asymmetry

between conduction and valence band. This term is negligible at low energies ($|E/t| \ll 1$). Indeed, by comparison between the dispersion relations with and without the overlap parameter shown in Fig. 2.4, one sees that s is negligible close to the K and K' points.

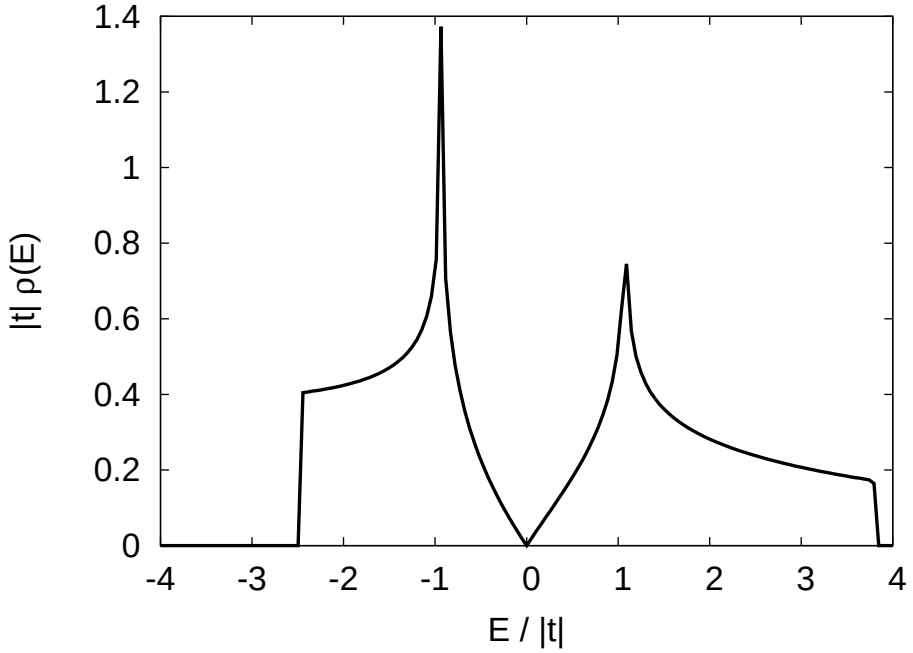

Figure 2.5: Density of states (DOS) as a function of energy (in units of $|t|$) obtained by the dispersion relation (2.40).

Fig. 2.5 shows the density of states $\rho(E)$ as a function of the energy. Positive energies refer to the conduction band whereas negative energies refer to the valence band. Close to the neutrality point ($E = 0$), the density of states $\rho(E)$ has a linear behavior. This is due to the linearity of the electronic bands in proximity of the corner points K and K'.

In each band there is a separatrix which passes through the saddle points M_ℓ ($\ell = 1, 2, 3$). A separatrix is an isoenergetic line which separates regions with different topology. A Fermi level crossing these saddle points would imply the change in the topology of the Fermi surface, which actually corresponds to a Lifshitz transition of the neck-disruption type. A Lifshitz transition [86, 106], also known as electronic topological transition (ETT), is a change in the Fermi surface topology occurring upon a continuous change of some external parameter, such as pressure, magnetic field or, most naturally, doping. This transition does not involve a symmetry breaking, as in conventional phase transitions of the Landau type, but still leads to observable singularities

in thermodynamics, electron transport, sound propagation, and the magnetic response of metals [3, 14]. The hallmark of an ETT is provided, in a two-dimensional system, by a logarithmic cusp (Van Hove singularity) in the DOS. Indeed, Fig. 2.5 shows that the DOS exhibits two logarithmic divergences which are due to the separatrices present in the electronic bands (one for each band).

In addition to the knowledge of the dispersion relations of the electronic bands, it is useful to obtain the eigenstates of the model. The eigenvectors in Eq. (2.21) can be presented as

$$\mathbf{u}_{\mathbf{k}\lambda} = \frac{1}{\sqrt{2}} \begin{pmatrix} (-1)^{\lambda} \\ e^{-i\theta_{\mathbf{k}}} \end{pmatrix}, \tag{2.44}$$

where

$$e^{i\theta_{\mathbf{k}}} = -\frac{\gamma_{\mathbf{k}}}{|\gamma_{\mathbf{k}}|}. \tag{2.45}$$

The norm of the eigenvector in Eq. (2.44) is given by:

$$\|\mathbf{u}_{\mathbf{k}\lambda}\| = \langle \mathbf{k}\lambda | \mathbf{k}\lambda \rangle^{1/2} = 1 + \mathcal{O}(s^{(2)}) \qquad \lambda = 1, 2, \tag{2.46}$$

and consistently with our choice of truncation these eigenvectors are orthonormal.

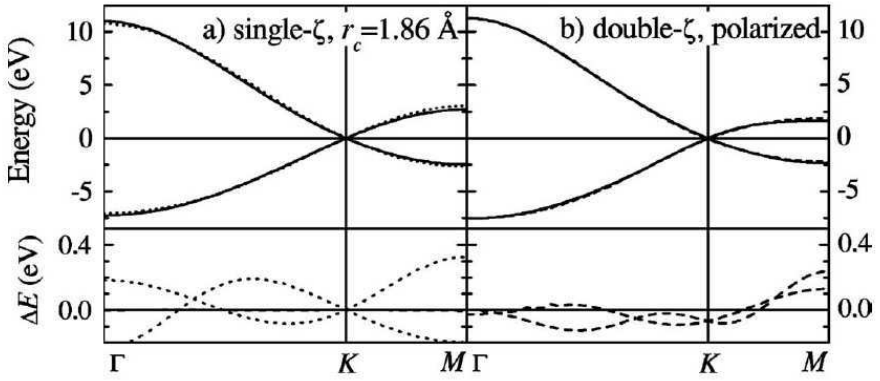

Figure 2.6: (a) *Top*, full lines: *ab initio* result with a simple basis set (single-ζ) and a radial cutoff $r_c = 1.86$ Å; dotted lines: nearest-neighbor tight binding band structure Eq. (2.40) with $t = -2.8$ eV and $s = 0.07$. The *ab initio* result shown by the full line coincides, in this energy scale, with the third-nearest neighbor tight binding model. *Bottom*, dotted line: difference between the *ab initio* and the nearest neighbor tight-binding band structure shown in the top panel. (b) *Top*, full lines: *ab initio* result with a double-ζ plus polarization basis set and a radial cutoff $r_c = 3.31$ Å; dashed lines: third-neighbor tight-binding band structures. *Bottom*: difference between the two band structures above. Adapted from [129].

In order to study the electronic properties of graphene over the whole bandwidth we will use the model just presented, *i.e.* the nearest-neighbor tight binding model.

In Fig. 2.6 (a), Reich *et al.* compare the nearest-neighbor tight binding band structure (dotted lines) with an *ab initio* band structure (solid lines) and the third-nearest neighbor tight-binding band structure (which coincides with *ab initio* results) [129]. In particular, for the *ab initio* band structure in Fig. 2.6 (a), Reich *et al.* used a simple basis set (single-ζ) with a cutoff radius of 1.86 Å. By a comparison between the dispersion relations in Eq. (2.40) and *ab initio* calculations have obtained that there is a discrepancy always lesser than 0.4 eV over the whole bandwidth for both the conduction bands and the valence bands.

In Fig. 2.6 (b), Reich *et al.* compare the third-nearest neighbor tight-binding band structure (dashed lines) with a more accurate *ab initio* band structure (solid lines) [129]. In particular, for the first principles band structure in Fig. 2.6 (b), Reich *et al.* used two independent radial functions to describe the p orbitals, and included a shell of polarized d orbitals (double-ζ plus polarization basis set), and had a radial cutoff of 3.31 Å. By a comparison between the dispersion relations in Eq. (2.40) and *ab initio* calculations shown in Fig. 2.6 (b) the discrepancy is maximum at the saddle point (M point) and it is around 1 eV, at the center of 1BZ (Γ point) the discrepancy is around 0.3 eV, and the agreement is excellent in proximity of the Dirac points.

Although the nearest-neighbor tight binding model is quantitatively reliable to describe the low energy ($|E/t| \ll 1$) properties, this model is qualitatively relevant because it contains all the principal features of the electronic structure of graphene (i.e. Dirac points, saddle points, finite bandwidths). In particular, our principal results are directly explainable in terms of these features of the electronic system, which can be traced back to the lattice symmetry.

2.2 Massless Dirac fermions

Intrinsic graphene has a Fermi energy coinciding with the energy $E = 0$ at the K and K' points. For experimentally realizable dopings, the Fermi energy is much smaller than the hopping energy $|E_{\mathrm{F}}/t| \ll 1$. Thus, it is useful to employ an effective model to describe the low-energy excitations. This model is obtained by the expansion of the complete electronic Hamiltonian $\mathcal{H}$ around the K and K' points [76].

An arbitrary wave function $\psi(\mathbf{r}, z)$ involving only low-energy states can be written in terms of a four component smooth envelope function $\Psi(\mathbf{r})$, or its Fourier transform $\Psi(\mathbf{p})$, as [9]

$$\begin{aligned}\psi(\mathbf{r}, z) = \int \frac{d^2\mathbf{p}}{(2\pi)^2} \Psi_{AK}(\mathbf{p}) e^{i(\mathbf{K}+\mathbf{p})\cdot\mathbf{r}} \mathcal{U}_{AK}(\mathbf{r}, z) + \Psi_{BK}(\mathbf{p}) e^{i(\mathbf{K}+\mathbf{p})\cdot\mathbf{r}} \mathcal{U}_{BK}(\mathbf{r}, z) + \\ + \Psi_{AK'}(\mathbf{p}) e^{i(\mathbf{K}'+\mathbf{p})\cdot\mathbf{r}} \mathcal{U}_{AK'}(\mathbf{r}, z) + \Psi_{BK'}(\mathbf{p}) e^{i(\mathbf{K}'+\mathbf{p})\cdot\mathbf{r}} \mathcal{U}_{BK'}(\mathbf{r}, z).\end{aligned} \tag{2.47}$$

The low-energy effective electronic Hamiltonian is defined as a matrix of order 4 whose element between any two smooth envelope functions, e.g. $\Psi(\mathbf{r})$ and $\Psi'(\mathbf{r})$, coincides with the matrix element of the complete Hamiltonian, between the corresponding full wave functions $\psi(\mathbf{r}, z)$ and $\psi'(\mathbf{r}, z)$

$$\int d^2\mathbf{r} \Psi^\dagger(\mathbf{r}) H(-i\nabla) \Psi'(\mathbf{r}) = \int d^2\mathbf{r} dz \psi^\dagger(\mathbf{r}, z) \mathcal{H}(-i\nabla, \mathbf{r}, -i\partial_z, z) \psi'(\mathbf{r}, z). \tag{2.48}$$

If one uses as the complete Hamiltonian the one obtained by means of the tight binding approximation and expands the effective Hamiltonian in powers of the momentum, one obtains as leading term ($pa \ll 1$) the following matrix

$$H(\mathbf{p}) = \hbar v_{\mathrm{F}} \tau_0 \boldsymbol{\sigma} \cdot \mathbf{p}, \tag{2.49}$$

where $v_{\mathrm{F}} = 3ta/2\hbar$ is the Fermi velocity. Moreover, $\boldsymbol{\sigma} = (\sigma_x, \sigma_y)$ is a vector consisting of two Pauli matrices acting in the two-dimensional pseudospin space (A and B), whereas τ_0 is an identity matrix of order 2 which acts in the two-dimensional valley space (K and K'). The Hamiltonian, Eq.(2.49), acts on the generic four-component spinor

$$\Psi_{\mathbf{p}} = \left(\Psi_{AK}(\mathbf{p}), \Psi_{BK}(\mathbf{p}), \Psi_{BK'}(\mathbf{p}), -\Psi_{AK'}(\mathbf{p})\right)^\top. \tag{2.50}$$

Using this particular choice of the form of the generic spinor, one has the most symmetric form for the effective Hamiltonian [9]. Moreover Basko, using symmetry considerations, has demonstrated that the leading term of the effective Hamiltonian in powers of $\mathbf{p}$ is unique and is expressed by Eq. (2.49), independently of the microscopic model used.

In ideal graphene the valleys K and K' are decoupled. However, the presence of some inhomogeneity can induce a coupling between the valleys. In particular, an inhomogeneity

which is smooth at the atomic scale leaves the valleys independent. Hence, an atomic-scale inhomogeneity, *e.g.* point-defects, can mix the states from different valleys [76, 109].

In each valley (K or K') the dynamics of the low energy massless quasiparticles can be effectively described by the Dirac-Weyl equation, rather than by the Schrödinger equation. This is why the points of the 1BZ, where conduction and valence bands touch each other, are termed Dirac points .

The dispersion relations obtained by the Hamiltonian, Eq. (2.49), are given by

$$E_\lambda(\mathbf{p}) = (-1)^\lambda \hbar v_{\mathrm{F}} p, \tag{2.51}$$

where $\lambda = 1$ refers to the valence band, and $\lambda = 2$ refers to the conduction band. Hence, both the conduction band and the valence band consist of two isotropic cones, one centered at the K point and the other one at the K' point. According to the dispersion relations, Eq. (2.51), the low energy excitations are massless, and characterized by an energy independent Fermi velocity v_{F}. Hence, each eigenstate of the energy is identified by the momentum $\mathbf{p}$, the valley label (K or K'), and the z-projection of the real spin. The latter will be omitted.

By analogy with the spin of the electron, the pseudospin operator is defined as

$$\mathbf{\Sigma} = \frac{1}{2}\tau_0 \boldsymbol{\sigma}. \tag{2.52}$$

Hence, a relevant quantity which characterizes the eigenstates is their helicity, which is defined as the projection of the momentum operator along the pseudospin direction

$$\mathbf{\Sigma} \cdot \frac{\mathbf{p}}{p} \Psi_\lambda(\mathbf{p}) = (-1)^\lambda \Psi_\lambda(\mathbf{p}), \qquad \lambda = 1, 2. \tag{2.53}$$

One finds that electrons (holes) in graphene have parallel (antiparallel) pseudospin along the direction of motion [76].

Finally, using the conical relation dispersions, Eq. (2.51), one can find the analytical expression of the DOS at low energies

$$\rho(E) = \frac{3\sqrt{3}}{\pi} \frac{a^2}{\hbar^2 v_{\mathrm{F}}^2} |E|. \tag{2.54}$$

Hence, for energies near the neutrality point ($E = 0$), the DOS behaves as a linear function of the energy, and the slope is inversely proportional to the square of the Fermi velocity.

Chapter 3

Strain effect on the electronic bands

Graphene is an atomically thick membrane but, notwithstanding its low dimensionality, it is notable for its remarkable mechanical properties [77, 87]. These properties suggested that applied strain can induce substantial modifications of the band structure of graphene, such as the opening of a gap at the Fermi level, thereby triggering a quantum phase transition from a semimetal to a semiconductor. While earlier *ab initio* calculations were suggestive of a gap opening for arbitrary strain modulus and direction [60], both tight-binding models [121] as well as more accurate *ab initio* calculations [130] point towards the conclusion that the strain-induced opening of a band gap in fact depends critically on the direction of strain.

In this Chapter, we will be concerned on the effects induced by applied strain on the electronic bands. Although uniaxial strain will be included in a standard, non-interacting model Hamiltonian at the tight-binding level, *i.e.* through the introduction of strain-dependent hopping parameters [121], this will nonetheless capture the essential consequences of applied strain on the band structure of graphene.

Moreover, we will study the modifications of the optical conductivity due to the strain. This quantity is related to measurable quantities, such as the optical transmittance or the optical absorption. In the case of unstrained graphene, the optical conductivity has been derived within the Dirac-cone approximation [62], and within a more accurate tight binding approximation also for frequencies in the visible range [138]. The effect of disorder has been considered by Peres *et al.* [124], and that of finite temperature by Falkovsky and Varlamov [42]. These studies are consistent with the experimental observation of a nearly constant conductivity of $\pi e^2/2h$

over a relatively broad frequency range [93, 101]. Such a result demonstrates that impurities and phonon effects can be neglected in the visible range of frequencies [93]. Hence, using the tight binding model, we will analyze how the modifications of the electronic bands due to the applied strain induce a direct effect on the optical responses of graphene [111].

3.1 Tight binding model for strained graphene

In this paragraph we deal with the strain effects on the tight binding model, which we have derived in detail in § 2.1.

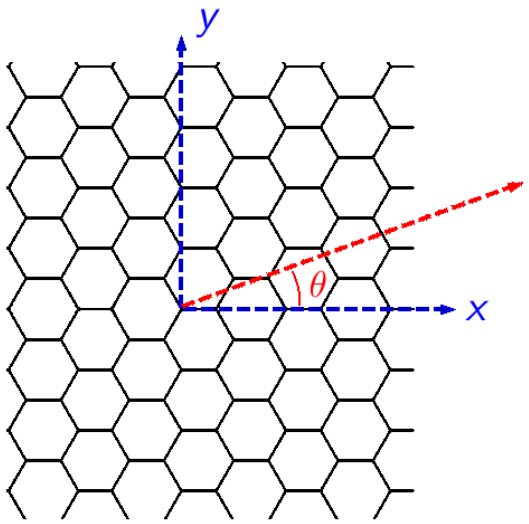

Figure 3.1: Lattice coordinate system. The abscissa coincides with the armchair direction and the ordinate coincides with the zig-zag direction . The uniaxial strain is identified by a vector, whose modulus is the longitudinal deformation ε and its direction θ is that of the applied tension.

In particular, we are interested in uniformly strained graphene. The generalized Hooke's law, which relates the stress tensor τ_{ij} and strain tensor ε_{ij}, has the general form

$$\varepsilon_{ij} = \sum_{hk} S_{ijhk}\tau_{hk}, \tag{3.1}$$

where S_{ijhk} is the generic component of the compliance tensor [5]. In the case of a bidimensional system with hexagonal symmetry, such as graphene, the S_{ijhk} tensor has only two independent components, as in an elastic continuum sheet [80, 121]. Hence, if we take into account

to apply a uniform tension T along a generic direction we have only a longitudinal deformation equal to $S_{xxxx}T$, and a transversal deformation equal to $S_{xxyy}T$. The strain tensor in the lattice coordinate system, in Fig. 3.1, is written as

$$\boldsymbol{\varepsilon} = \varepsilon \begin{pmatrix} \cos^2\theta - \nu \sin^2\theta & (1+\nu)\cos\theta\sin\theta \\ (1+\nu)\cos\theta\sin\theta & \sin^2\theta - \nu\cos^2\theta \end{pmatrix}, \tag{3.2}$$

where ε is the longitudinal deformation, ν is the Poisson's ratio ($\nu = -S_{xxyy}/S_{xxxx}$), and θ denotes the direction along which the tension is applied, with respect to the $\hat{x}$ axis in the lattice coordinate system. In particular, for the Poisson's ratio we use the value $\nu = 0.14$, as determined from *ab initio* calculations for graphene [43]. Such value is comparable with the known experimental value $\nu = 0.165$ for graphite [12]. We will focus on the uniaxial strain, and in this case the tunable parameters are the strain modulus ε and the direction of the tension θ. According to Fig. 3.1, the special values $\theta = m\pi/3$ and $\theta = \pi/6 + n\pi/3$, where m and n are any two integers, refer respectively to the armchair and the zig-zag directions.

Moreover, the form of the strain tensor in Eq. (3.2) is suitable also for biaxial deformation, but in this case the parameter ν is different from Poisson's ratio and becomes a tunable parameter. In particular, if one fixes $\nu = -1$, we can treat the case of homogeneous deformation, which, at variance with the other cases, preserves hexagonal lattice symmetry.

In terms of the strain tensor, the deformed lattice distances are related to the relaxed (unstrained) ones by:

$$\mathbf{R} = (\mathbb{I} + \boldsymbol{\varepsilon}) \cdot \mathbf{R}^{(0)}, \tag{3.3}$$

where $\mathbf{R}^{(0)}$ is a generic vector in the relaxed graphene lattice. Hence, the three vectors $\boldsymbol{\delta}_\ell^{(0)}$ which connect any carbon atom to its nearest neighbors, defined in Eqs. (2.2), are modified by the previous linear transformation as

$$\boldsymbol{\delta}_\ell = (\mathbb{I} + \boldsymbol{\varepsilon}) \cdot \boldsymbol{\delta}_\ell^{(0)}. \tag{3.4}$$

The deformation of the direct lattice according to the Eq. (3.3) leads to a modification of the reciprocal lattice vectors

$$\mathbf{G} = (\mathbb{I} + \boldsymbol{\varepsilon})^{-1} \cdot \mathbf{G}^{(0)}. \tag{3.5}$$

A modification of the lattice, and in particular the change in bond lengths (3.4), leads to different hopping parameters and overlap parameters between nearest neighbors. In the previous Chapter, we have shown that, within the tight binding approximation, the energy dispersion relations $E_{\mathbf{k}\lambda}$ can be obtained as the solutions of the generalized eigenvalue problem

$$H_{\mathbf{k}}\mathbf{u}_{\mathbf{k}\lambda} = E_{\mathbf{k}\lambda}S_{\mathbf{k}}\mathbf{u}_{\mathbf{k}\lambda},$$

where

$$H_{\mathbf{k}} = \begin{pmatrix} 0 & f_{\mathbf{k}} \\ f_{\mathbf{k}}^* & 0 \end{pmatrix}, \tag{3.6a}$$

$$S_{\mathbf{k}} = \begin{pmatrix} 1 & g_{\mathbf{k}} \\ g_{\mathbf{k}}^* & 1 \end{pmatrix}. \tag{3.6b}$$

The off-diagonal elements of the two matrices are related to the following complex functions

$$f_{\mathbf{k}} = \sum_{\ell=1}^{3} t_\ell e^{i\mathbf{k}\cdot\boldsymbol{\delta}_\ell}, \tag{3.7a}$$

$$g_{\mathbf{k}} = \sum_{\ell=1}^{3} s_\ell e^{i\mathbf{k}\cdot\boldsymbol{\delta}_\ell}, \tag{3.7b}$$

where $t_\ell = t(\boldsymbol{\delta}_\ell)$ and $s_\ell = s(\boldsymbol{\delta}_\ell)$ are respectively the hopping parameters and the overlap parameters between two nearest neighbors connected by one of the three vectors $\boldsymbol{\delta}_\ell$ $(\ell = 1, 2, 3)$. The complex functions in Eqs. (3.7) can be expressed in terms of the wavevectors of unstrained graphene. Exploiting Eqs. (3.4) and (3.5) one can write

$$f_{\mathbf{k}} = \sum_{\ell=1}^{3} t_\ell e^{i\mathbf{k}^{(0)}\cdot\boldsymbol{\delta}_\ell^{(0)}}, \tag{3.8a}$$

$$g_{\mathbf{k}} = \sum_{\ell=1}^{3} s_\ell e^{i\mathbf{k}^{(0)}\cdot\boldsymbol{\delta}_\ell^{(0)}}, \tag{3.8b}$$

where $t_\ell = t(\boldsymbol{\delta}_\ell)$ and $s_\ell = s(\boldsymbol{\delta}_\ell)$ are respectively the hopping parameters and the overlap parameters used in Eqs. (3.7).

So far, we have not chosen the analytical form of the atomic wave function $\phi(\mathbf{r})$, but we

have only assumed that it has some general properties. Due to the two-dimensionality of the graphene sheet, we can safely neglect that extension along the axis orthogonal to the graphene, z say [109]. One possible choice of the atomic wave function is such that its square modulus is a normalized gaussian function

$$\phi(\mathbf{r}) = (1/\sqrt{\pi}\sigma_g)\exp(-r^2/2\sigma_g^2), \tag{3.9}$$

where $1/\sigma_g = Z_g/2\sqrt{3}a$, and the value $Z_g = 11.2$ is fixed by the condition that the relaxed overlap parameter be $s = 0.07$ [109, 129]. Thus, the strain-dependent overlap parameters s_ℓ are defined as

$$s_\ell = \int d\mathbf{r}\phi(\mathbf{r})\phi(\mathbf{r}+\boldsymbol{\delta}_\ell) = \exp\left(-\frac{\delta_\ell^2}{4\sigma_g^2}\right). \tag{3.10}$$

Correspondingly, the hopping parameters t_ℓ are defined as the transition amplitudes of the single-particle Hamiltonian, $H_1 = -(\hbar^2/2m)\nabla^2 - Ze^2/r$, between two lattice sites being $\boldsymbol{\delta}_\ell$ apart from each other. Here, Z is chosen so that $t = -2.8$ eV in the unstrained limit. One finds

$$t_\ell = \left[\frac{\hbar^2}{2m\sigma_g^2}\left(1+\frac{\delta_\ell^2}{4\sigma_g^2}\right) - \frac{Ze^2\sqrt{\pi}}{\sigma_g} I_0\left(\frac{\delta_\ell^2}{8\sigma_g^2}\right)\right] s_\ell, \tag{3.11}$$

where $I_0(x)$ is a modified Bessel function of the first kind [58]. One finds $dt_\ell/d\delta_\ell = 7.6$ eV/Å for $\varepsilon = 0$, which is comparable with the value 6.4 eV/Å obtained in Ref. [121] within Harrison's approach [67]. In the unstrained limit ($\varepsilon = 0$), Eqs. (3.7) reduce to $f_\mathbf{k} \to t\gamma_\mathbf{k}$ and $g_\mathbf{k} \to s\gamma_\mathbf{k}$, respectively. The solution of the generalized eigenvalue problem gives the dispersion relations

$$E_{\mathbf{k}\lambda} = \frac{-F_\mathbf{k} + (-1)^\lambda\sqrt{F_\mathbf{k}^2 + 4G_\mathbf{k}|f_\mathbf{k}|^2}}{2G_\mathbf{k}}, \tag{3.12}$$

where $\lambda = 1$ refers to the valence band, and $\lambda = 2$ refers to the conduction band, and

$$F_\mathbf{k} = g_\mathbf{k}f_\mathbf{k}^* + g_\mathbf{k}^* f_\mathbf{k}, \tag{3.13a}$$

$$G_\mathbf{k} = 1 - |g_\mathbf{k}|^2. \tag{3.13b}$$

The associated eigenvectors $\mathbf{u}_{\mathbf{k}\lambda}$ can be presented as

$$u_{\mathbf{k}\lambda} = \begin{pmatrix} \cos\phi_{\mathbf{k}\lambda} \\ e^{-i\theta_{\mathbf{k}}}\sin\phi_{\mathbf{k}\lambda} \end{pmatrix}, \tag{3.14}$$

where

$$e^{i\theta_{\mathbf{k}}} = f_{\mathbf{k}}/|f_{\mathbf{k}}|, \tag{3.15}$$

and

$$\cos\phi_{\mathbf{k}\lambda} = -\frac{E_{\mathbf{k}\bar{\lambda}}\sqrt{G_{\mathbf{k}}}}{\sqrt{|f_{\mathbf{k}}|^2 + G_{\mathbf{k}}E_{\mathbf{k}\bar{\lambda}}^2}}, \tag{3.16a}$$

$$\sin\phi_{\mathbf{k}\lambda} = -\frac{|f_{\mathbf{k}}|}{\sqrt{|f_{\mathbf{k}}|^2 + G_{\mathbf{k}}E_{\mathbf{k}\bar{\lambda}}^2}}, \tag{3.16b}$$

with $\cos(\phi_{\mathbf{k},1} - \phi_{\mathbf{k},2}) = 0$. In the limit of no strain, one finds $\phi_{\mathbf{k},1} \to 3\pi/4$ and $\phi_{\mathbf{k},2} \to \pi/4$. Here and below, $\bar{\lambda} = 2$ when $\lambda = 1$, and vice versa. In the unstrained limit ($\varepsilon = 0$), one recovers the band dispersion in Eq. (2.40).

The band dispersion relations $E_{\mathbf{k}\lambda}$, Eq. (3.12), are characterized by Dirac points, *i.e.* points in $\mathbf{k}$-space around which the dispersion is linear, when $f_{\mathbf{k}} = 0$. As a function of strain, such a condition is satisfied by two inequivalent points $\pm\mathbf{k}_D$ only when the 'triangular inequalities'

$$|t_{\ell_1} - t_{\ell_2}| \leq |t_{\ell_3}| \leq |t_{\ell_1} + t_{\ell_2}| \tag{3.17}$$

are fulfilled [68], with (ℓ_1, ℓ_2, ℓ_3) a permutation of $(1, 2, 3)$. Around such points, the dispersion relations $E_{\mathbf{k}\lambda}$ can be approximated by cones, whose constant energy sections are ellipses.

The location of $\pm\mathbf{k}_D$ in the reciprocal lattice satisfies

$$\cos\left(\mathbf{k}_D \cdot (\boldsymbol{\delta}_{\ell_1} - \boldsymbol{\delta}_{\ell_2})\right) = \frac{t_{\ell_3}^2 - t_{\ell_1}^2 - t_{\ell_2}^2}{2t_{\ell_1}t_{\ell_2}}, \tag{3.18}$$

with (ℓ_1, ℓ_2, ℓ_3) a permutation of $(1, 2, 3)$. While in the unstrained limit the Dirac points are located at the vertices of the 1BZ, *i.e.* $\mathbf{k}_D \to K =$ and $-\mathbf{k}_D \to K' \equiv -K$, when either of the limiting conditions in Eqs. (3.17) is fulfilled as a function of strain, say when $t_{\ell_3} = t_{\ell_1} + t_{\ell_2}$, the would-be Dirac points coincide with the middle points of the sides of the 1BZ, say $\mathbf{k}_D \to M_{\ell_3}$.

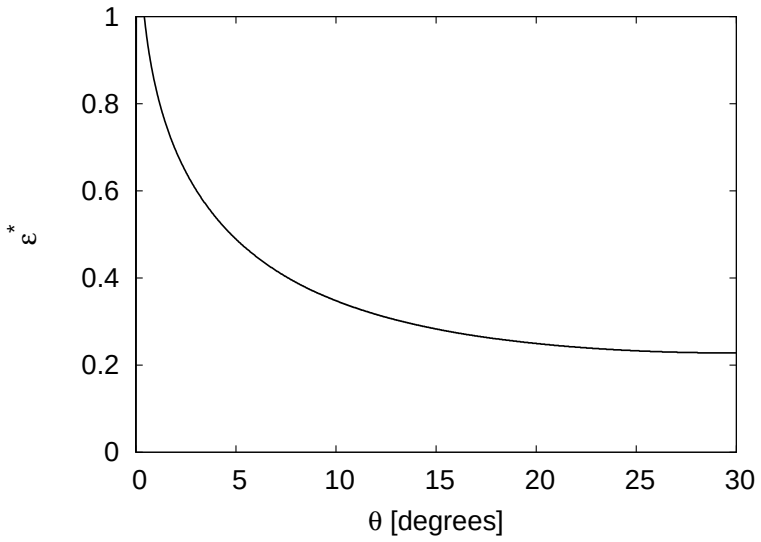

Figure 3.2: Critical value of the longitudinal deformation ε^* as a function of the direction of the applied tension θ. In this plot, a limited interval of values of the direction θ are taken into account because any other value can be obtained exploiting the lattice symmetry properties.

In this limit, the dispersion relations cease to be linear in a specific direction, and the cone approximation fails. For each direction θ there is a critical value of the longitudinal deformation ε^* at which the Dirac points coincide with the middle points of the sides of the 1BZ, and thus for larger deformations ($\varepsilon > \varepsilon^*$) there is a gap opening. Fig. 3.2 shows the critical value ε^* as a function of the direction of the applied tension. One finds that the zig-zag direction gives the minimum value of the critical deformation $\varepsilon^* = 22.8\%$, whereas for the armchair direction ε^* diverges, this implying that in this case it is impossible to have a gap opening. These results are in excellent agreement with *ab initio* calculations [32].

In order to make a comparison between the electronic bands with or withour strain it is useful to express the $\mathbf{k}$-dependences in terms of the unstrained reciprocal lattice, exploiting relations in Eqs. (3.4) and (3.5). Under the conditions given by Eqs. (3.17), the band dispersions, Eqs. (3.12), can be expanded as $E_{\mathbf{q}\lambda} \equiv E_{\mathbf{k}\lambda}$ around either Dirac point, with $\mathbf{k} = \mathbf{k}_D + \mathbf{q}$, as:

$$E_{\mathbf{q}\lambda} = \frac{-\mathbf{q}\cdot\mathbf{d} + (-1)^\lambda \sqrt{(\mathbf{q}\cdot\mathbf{d})^2 + 4G_{\mathbf{k}_D}|\mathbf{q}\cdot\nabla f_{\mathbf{k}_D}|^2}}{2G_{\mathbf{k}_D}}, \tag{3.19}$$

where

$$\mathbf{d} = g_{\mathbf{k}_D} \nabla f^*_{\mathbf{k}_D} + g^*_{\mathbf{k}_D} \nabla f_{\mathbf{k}_D}. \tag{3.20}$$

Eq. (3.19) defines a cone, whose section $E_{\mathbf{q}\lambda} = E$ at a constant energy level E is an ellipse. Its equation can be cast in canonical form as

$$\frac{(q_x - q_{x0})^2}{A^2} + \frac{(q_y - q_{y0})^2}{B^2} = E^2. \tag{3.21}$$

The center (q_{x0}, q_{y0}) with respect to $\mathbf{k}_D$ of the ellipse evolves linearly with energy E according to

$$q_{x0} = \frac{1}{2} A^2 (d_x \cos\eta - d_y \sin\eta) E \tag{3.22a}$$

$$q_{y0} = \frac{1}{2} B^2 (d_x \sin\eta + d_y \cos\eta) E. \tag{3.22b}$$

The ellipse semiaxes A, B are given by

$$\frac{1}{A^2} = \frac{1}{2}(\gamma - \sqrt{\alpha^2 + \beta^2}) \tag{3.23a}$$

$$\frac{1}{B^2} = \frac{1}{2}(\gamma + \sqrt{\alpha^2 + \beta^2}). \tag{3.23b}$$

In the above equations, we have made use of the following definitions:

$$\cos\eta = \frac{1}{\sqrt{2}} \left(1 + \frac{\alpha}{\sqrt{\alpha^2 + \beta^2}} \right)^{1/2} \tag{3.24a}$$

$$\sin\eta = \frac{\beta}{2\cos\eta \sqrt{\alpha^2 + \beta^2}} \tag{3.24b}$$

$$\alpha = -\frac{3a^2}{2}(t_1^2 + t_2^2 - 2t_3^2) \tag{3.24c}$$

$$\beta = -\frac{3\sqrt{3}a^2}{2}(t_1^2 - t_2^2) \tag{3.24d}$$

$$\gamma = \frac{3a^2}{2}(t_1^2 + t_2^2 + t_3^2). \tag{3.24e}$$

One finds $\alpha, \beta \to 0$, while $\gamma \to 9t^2a^2/2$, in the limit of no strain, $\varepsilon \to 0$. Further insight into the anisotropic character of the low-energy cone dispersion relations around the Dirac points, Eq. (3.19) can be obtained by recasting them in polar coordinates (q, ϕ), where

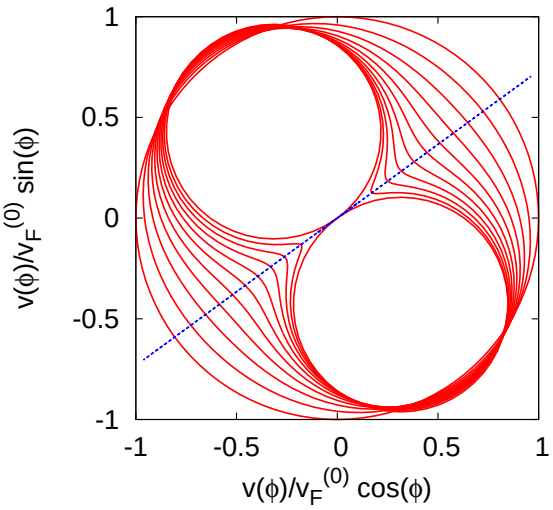

Figure 3.3: Polar plot of $v_\lambda(\phi)$ (with $\lambda = 2$, *i.e.* for the conduction band) around $\mathbf{k}_D$, $v_\lambda(\phi)$, normalized with respect to its value in the absence of strain, $v_{\mathrm{F}}^{(0)}$. Strain is here applied at a generic fixed angle $\theta = \pi/4$. The anisotropy of the Fermi velocity increases with increasing strain, until the shape of $v_\lambda(\phi)$ breaks at $\varepsilon = 0.28$. This corresponds to the existence of a direction (dashed blue line), Eq. (3.25), along which the dispersion relation $E_{\mathbf{q}\lambda}$ displays a nonlinear character.

$\mathbf{q} = (q\cos\phi, q\sin\phi)$. One finds therefore $E_{\mathbf{q}\lambda} = v_\lambda(\phi)q$, the anisotropic prefactor $v_\lambda(\phi)$ depending on the Dirac point around which one is actually performing the expansion. Fig. 3.3 shows $v_\lambda(\phi)$ for the conduction band ($\lambda = 2$) centered around $\mathbf{k}_D$. One notices that applied strain increases the anisotropy of the ϕ dependence, until a critical value is reached, at which the cone approximation breaks down. This corresponds to a nonlinear behavior of $E_{\mathbf{q}\lambda}$ along a specific direction ϕ_0, characterized by the vanishing of $v_\lambda(\phi)$ and given explicitly by

$$\mathrm{cotg}\phi_0 = -\frac{\sqrt{3}}{3}\frac{t_1 \mp t_2}{t_1 \pm t_2}, \tag{3.25}$$

when $|t_3| = |t_1 \mp t_2|$ in Eqs. (3.17), and to the opening of a finite gap around zero energy in the DOS. In that case, the Fermi velocity vanishes along a direction ϕ_0' given by

$$\mathrm{cotg}\phi_0' = \frac{(1+\varepsilon_{xx})\mathrm{cotg}\phi_0 - \varepsilon_{xy}}{(1+\varepsilon_{yy}) - \varepsilon_{yx}\mathrm{cotg}\phi_0}. \tag{3.26}$$

Fig. 3.4 compares the tight binding model electronic band structure of strained graphene (red continuous lines), with strain modulus of $\varepsilon = 0.18$ along the generic direction $\theta = \pi/4$,

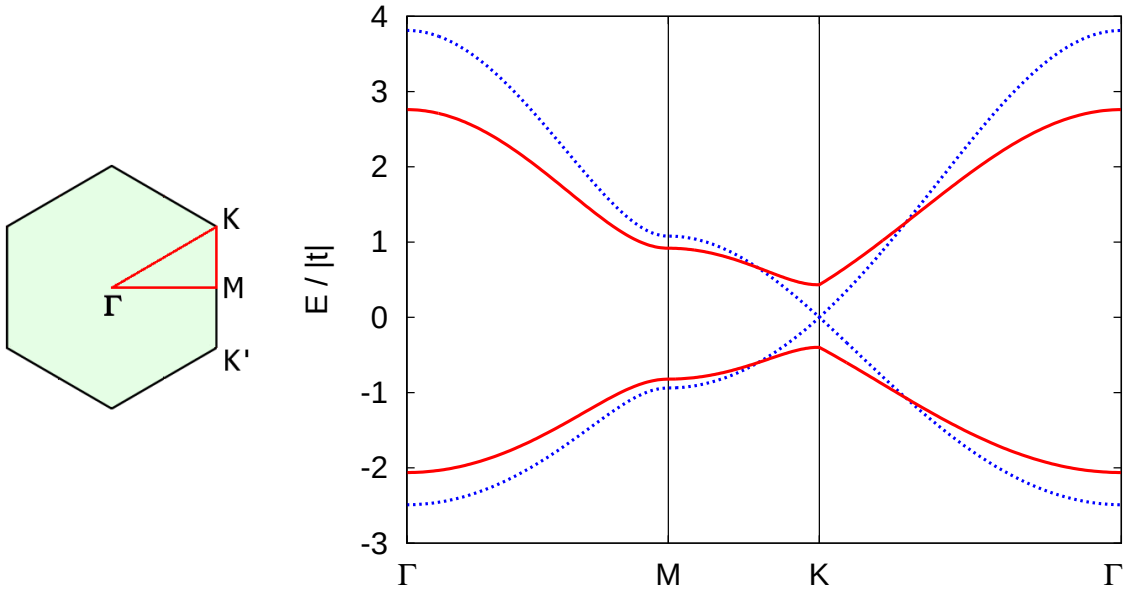

Figure 3.4: *Left*: High symmetry path Γ-M-K-Γ in the 1BZ. *Right*: Conduction band and valence band along the high symmetry path in graphene with a strain modulus of $\varepsilon = 0.18$ applied along $\theta = \pi/4$ (red continuous lines), and without strain applied (blue dotted lines). The unit of energy is the absolute value of the hopping parameter $t = -2.8$ eV.

and that of unstrained graphene (blue dotted lines). In Fig. 3.4 we evaluate the electronic bands along the high symmetry path Γ-M-K-Γ in the 1BZ, one can see that uniaxial strain causes a shrinking of the electronic bands. Actually, this modification of the electronic bands appear for any direction θ. Indeed, in Fig. 3.4 the Dirac point disappears. Both Dirac points are still well-defined, but they are not placed in special symmetry points.

Fig. 3.5 shows contour plots of $E_{\mathbf{k}\lambda}$, Eq. (3.12), at constant energy levels, with strain modulus of $\varepsilon = 0.18$ along the generic direction $\theta = \pi/4$. One can see that the Dirac points $\pm\mathbf{k}_D$ are shifted from the corners of the 1BZ, and they do not appear in Fig. 3.4 because they are not placed along the high symmetry path Γ-M-K-Γ. Moreover, for fixed strain, each of these lines can be interpreted as the Fermi line corresponding to a given chemical potential. One may observe that the various possible Fermi lines can be grouped into four families, according to their topology. In particular, from Fig. 3.5 one may distinguish among (i) closed Fermi lines around either Dirac point $\pm\mathbf{k}_D$ (and equivalent points in the 1BZ), (ii) closed Fermi lines around both Dirac points, (iii) open Fermi lines, (iv) closed Fermi lines around $\Gamma = (0, 0)$. The transition between two different topologies takes place when the Fermi line touches the midpoints of the

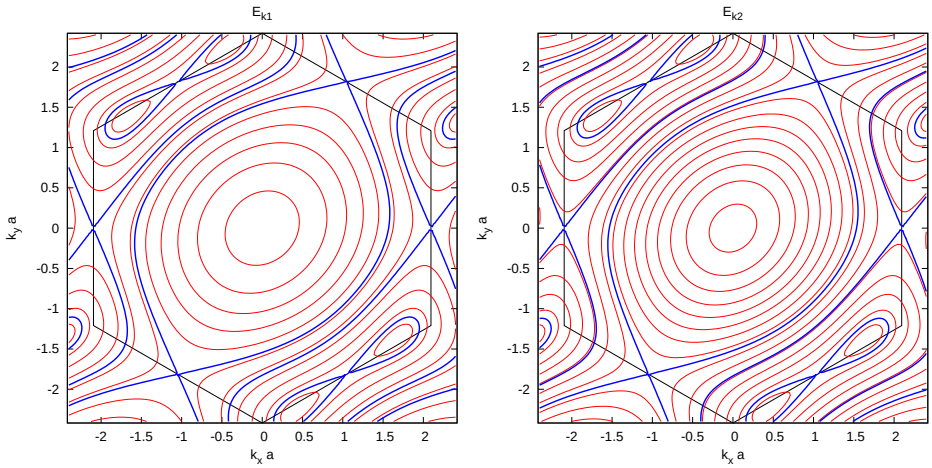

Figure 3.5: Contour plots of the dispersion relations within the 1BZ for the valence band, $E_{\mathbf{k}1}$ (left panel), and conduction band, $E_{\mathbf{k}2}$ (right panel). Here, we are depicting the situation corresponding to a strain modulus of $\varepsilon = 0.18$ along the generic direction $\theta = \pi/4$. Solid blue lines are separatrix lines and occur at an electronic topological transition, dividing groups of contours belonging to different topologies. Either line passes through one of the critical points M_ℓ ($\ell = 1, 2, 3$), defined as the middle points of the 1BZ edge (solid black hexagon).

boundary of the 1BZ (solid black hexagon in Fig. 3.5), and is marked by a separatrix line. Each separatrix line corresponds to an electronic topological transition (ETT) [86], *i.e.* a transition between two different topologies of the Fermi line. Here, in the case of strained graphene, we surmise the existence of at most three, possibly degenerate, ETTs, whose effect on observable quantities may be evidenced by the application of sufficiently intense strain along specific directions.

3.2 Density of states of strained graphene

Making use of Eq. (3.21), one can derive the low-energy expansion of the density of states (DOS), which turns out to be linear in energy,

$$\rho(E) = \rho_1 |E|, \tag{3.27}$$

with

$$\rho_1 = \frac{4}{\pi}[(t_1^2 + t_2^2 + t_3^2)^2 - 2(t_1^4 + t_2^4 + t_3^4)]^{-1/2}, \tag{3.28}$$

where the factor of four takes into account for the spin and valley degeneracies.

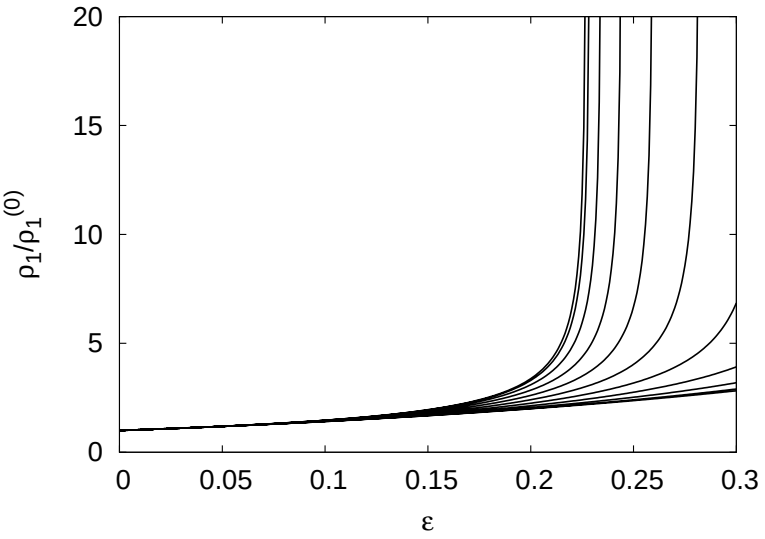

Figure 3.6: Showing the DOS prefactor ρ_1, Eq. (3.28), normalized with respect to its value $\rho_1^{(0)}$ in the absence of strain, as a function of the strain modulus ε, for various strain angles. The strain direction θ increases from $\theta = 0$ (armchair direction, corresponding to the lowest curve) to $\theta = \pi/6$ (topmost curve). All other cases can be reduced to one of these exploiting the symmetry properties of the lattice.

Fig. 3.6 shows the prefactor ρ_1, Eq. (3.28), as a function of the strain modulus ε, for various strain angles θ. One finds in general that ρ_1 increases monotonically with increasing strain. Such a behavior suggests that applied strain may be used to amplify the DOS close to the Fermi level. When the equality sign in Eqs. (3.17) is reached, the prefactor ρ_1 in Eq. (3.28) diverges, meaning that the cone approximation breaks down. In this case, the band dispersions still vanish, but now quadratically along a specific direction through the would-be Dirac point, and a nonzero gap in the DOS opens around $E = 0$.

This behavior is confirmed by the energy dependence of the DOS over the whole bandwidth, as numerically evaluated from the detailed band dispersions, Eq. (3.12). In particular, Fig. 3.7 shows $\rho(E)$ for increasing strain, at fixed strain angle $\theta = 0$ (armchair) and $\theta = \pi/6$ (zig-zag). In both cases, for sufficiently low values of the strain modulus, the DOS depends linearly on E, according to Eq. (3.27), and the DOS slope increases with increasing strain, in agreement with Eq. (3.28) and Fig. 3.6. However, while the spectrum remains gapless at all strains in the armchair case, a nonzero gap is formed at a critical strain in the zig-zag case $\theta = \pi/6$, corresponding to the breaking of the cone approximation at low energy. Such a behavior is confirmed by Fig. 3.8, showing the dependence of the DOS over the whole bandwidth, now at

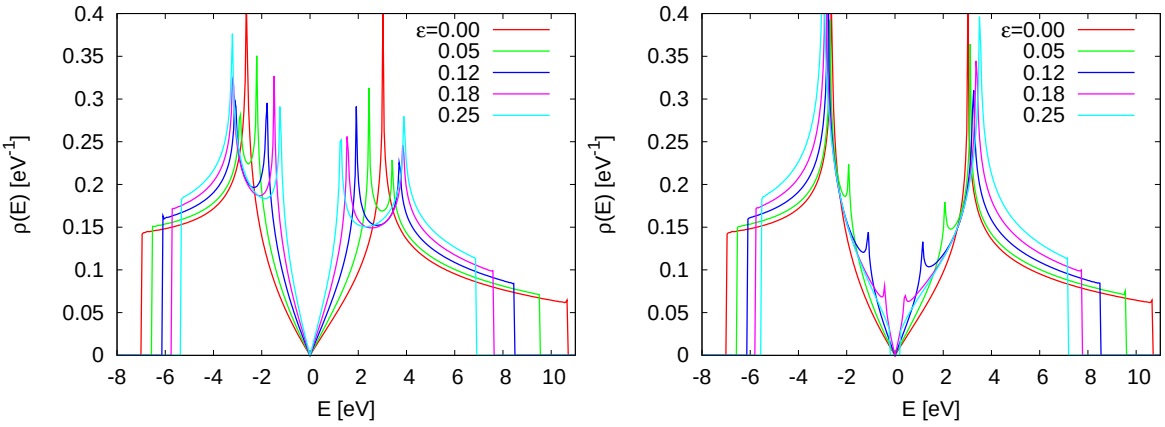

Figure 3.7: Energy dependence of the DOS over the whole bandwidth, for increasing strain modulus $\varepsilon = 0 - 0.25$ and fixed strain armchair direction (left panel) and zig-zag direction (right panel). In each case, the DOS slope close to the Fermi energy increases as a function of strain. However, while the DOS remains gapless for armchair case, a nonzero gap opens around $E = 0$ at a critical strain for any other case.

fixed strain modulus and varying strain angle.

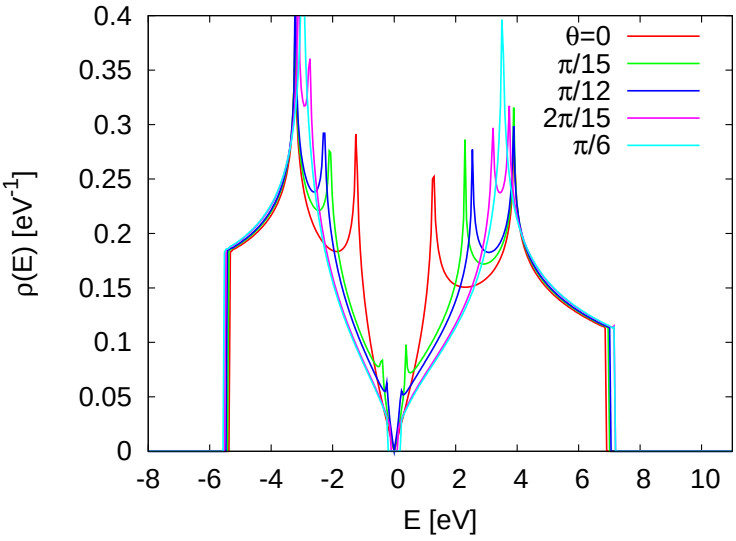

Figure 3.8: Energy dependence of the DOS over the full bandwidth, for fixed strain modulus $\varepsilon = 0.25$ and varying strain direction.

At sufficiently high energies, beyond the linear regime, the DOS exhibits Van Hove singularities both in the valence and in the conduction bands. As anticipated, these correspond to the occurrence of an ETT in the constant energy contours of either band dispersion relation $E_{\mathbf{k}\lambda}$,

Eq. (3.12). As shown by Fig. 3.7, the DOS is characterized by a single logarithmic cusp in each band in the unstrained limit ($\varepsilon = 0$), that is readily resolved into two logarithmic spikes, both in the $\theta = 0$ (armchair) and in the $\theta = \pi/6$ (zig-zag) cases, as soon as the strain modulus becomes nonzero ($\varepsilon > 0$). The low-energy spike disappears as soon as a gap is formed, corresponding to the breaking of the cone behavior around the Dirac point. Fig. 3.8 shows that the situation is indeed richer, in that the application of sufficiently intense strain along generic (*i.e.* non symmetry-privileged) directions allows the development of three logarithmic singularities in the DOS for each band, corresponding to the three inequivalent ETTs described in § 3.1. Again, the lowest energy Van Hove singularity disappears into the gap edge when the energy spectrum ceases to be linear around the Dirac points.

3.3 Optical conductivity of strained graphene

In order to obtain the optical conductivity in strained graphene we will use the linear response theory [23, 46, 54]. First of all, we choose a particular gauge such that the scalar potential is fixed

$$\varphi = 0, \tag{3.29}$$

and thus the electric field can be written only in terms of the vector potential as

$$\boldsymbol{\mathcal{E}} = -\frac{\partial \mathbf{A}}{\partial t}. \tag{3.30}$$

Thus, one takes into account the presence of a generic electromagnetic field adding a new term in the Hamiltonian

$$H^{\mathrm{A}} = -\int d\mathbf{r}\mathbf{J}(\mathbf{r},t)\cdot\mathbf{A}(\mathbf{r},t), \tag{3.31}$$

where the vector potential is coupled with the current density vector. One can split the current density vector in two terms, the paramagnetic and the diamagnetic term:

$$\mathbf{J} = \mathbf{J}^{\nabla} + \mathbf{J}^{A}, \tag{3.32}$$

which can be written respectively in terms of the field operators as

$$\mathbf{J}^{\nabla}(\mathbf{r}) = \frac{ie\hbar}{2m}\left[\Psi^{\dagger}(\mathbf{r})\nabla\Psi(\mathbf{r}) - \left(\nabla\Psi^{\dagger}(\mathbf{r})\right)\Psi(\mathbf{r})\right], \tag{3.33}$$

$$\mathbf{J}^{\mathrm{A}}(\mathbf{r}) = -\frac{e^2}{m}\mathbf{A}(\mathbf{r})\Psi^{\dagger}(\mathbf{r})\Psi(\mathbf{r}), \tag{3.34}$$

where m is the bare electron mass and, $-e$ is the electron charge.

We assume to have an electric field sufficiently weak such that one can treat it as a weak perturbation. This hypothesis allows us to use the linear response theory, and thus the response of the system to an external perturbation is linear in the same perturbation. The current density vector induced by the perturbation can written as

$$\langle\mathbf{J}(\mathbf{r},t)\rangle_{ext} = \langle\mathbf{J}(\mathbf{r},t)\rangle_0 - \frac{i}{\hbar}\int_{-\infty}^{t} dt'\langle\left[\mathbf{J}(\mathbf{r},t'), H^{\mathrm{A}}(t')\right]_-\rangle_0, \tag{3.35}$$

where $\langle\ldots\rangle_0$ is an equilibrium average with respect to the unperturbed Hamiltonian, and the symbol $[\ldots,\ldots]_-$ is a commutator. Taking into account only the linear terms in the vector potential, one finds

$$\langle J_h(\mathbf{r},t)\rangle_{ext} = -\frac{1}{4\pi}\sum_k \int d\mathbf{r}' \int_{-\infty}^{+\infty} dt' N_{hk}(\mathbf{r},\mathbf{r}',t-t')A_k(\mathbf{r}',t'), \tag{3.36}$$

where the kernel of the integral equation is invariant with respect to any time translation because the unperturbed Hamiltonian has no explicit time dependence. Exploiting a well-known theorem on the Fourier transform of a convolution, one can rewrite the previous expression in monochromatic components as

$$\langle\tilde{J}_h(\mathbf{q}',\omega)\rangle_{ext} = -\frac{1}{4\pi i\omega}\sum_k\sum_{\mathbf{G}}\delta_{\mathbf{q}',\mathbf{q}+\mathbf{G}}\tilde{N}_{hk}(\mathbf{q}+\mathbf{G},-\mathbf{q},\omega)\tilde{\mathcal{E}}_k(\mathbf{q},\omega), \tag{3.37}$$

where the Fourier transform of the external vector potential is written in terms of the Fourier transform of the external electric field. Since we are taking into account a crystal, the momentum of the response $\mathbf{q}'$ is equal to the momentum of the perturbation $\mathbf{q}$, or at most $\mathbf{q}'$ can differ from $\mathbf{q}$ by a vector of the reciprocal lattice. We are interested in an external homogeneous electric field, which means we take into account only the $\mathbf{q} = 0$ component. In addition, we

neglect in the response the components characterized by a wavelength of the order of the lattice distance, meaning that we take into account the response including only the $\mathbf{q}' = 0$ component. Thus one can rewrite the previous expression as

$$\langle \tilde{J}_h(0,\omega)\rangle_{ext} = \frac{ie^2\tilde{n}(0)}{m\omega}\mathcal{E}_h(0,\omega) + \sum_k \frac{i}{\hbar\omega}\tilde{\Pi}^{\mathrm{R}}_{hk}(0,0,\omega)\mathcal{E}_k(0,\omega), \tag{3.38}$$

where in the right-hand side there appears the Fourier transform of the electron density, $\tilde{n}$, and the Fourier transform of the retarded current-current correlation function, which is defined as

$$\Pi^{\mathrm{R}}_{hk}(\mathbf{r},\mathbf{r}',t) = -i\theta(t)\langle\left[J^{\nabla}_h(\mathbf{r},t), J^{\nabla}_k(\mathbf{r}',0)\right]_-\rangle_0. \tag{3.39}$$

Taking a space average of the current density

$$\mathbf{J}(\omega) = \frac{1}{NA_{cell}}\int d\mathbf{r}\langle\mathbf{J}(\mathbf{r},\omega)\rangle_{ext}, \tag{3.40}$$

one cancels out the atomic scale fluctuations [92]. Hence, the current density response is related to a homogeneous external electric field by means of the conductivity tensor

$$J_h(\omega) = \sum_k \overleftrightarrow{\sigma}_{hk}(\omega)\mathcal{E}_k(\omega), \tag{3.41}$$

which is explicitly written by means of the Kubo's formula as

$$\overleftrightarrow{\sigma}_{hk}(\omega) = \frac{ie^2n}{m\omega}\delta_{hk} + \frac{i}{\hbar\omega NA_{cell}}\tilde{\Pi}^{\mathrm{R}}_{hk}(0,0,\omega), \tag{3.42}$$

where n is the electron density, N is the number of the unit cells in the graphene sample under consideration, and A_{cell} is the area of the unit cell. Uniaxial strain changes the area of the unit cell as

$$A_{cell} = (1+\varepsilon)(1-\nu\varepsilon)\frac{3\sqrt{3}}{2}a^2, \tag{3.43}$$

where $a = 1.42$ Å. In addition, we are mainly interested in the dissipative part of the optical conductivity [54], *i.e.* its real part

$$\sigma_{hk}(\omega) = -\frac{1}{\hbar\omega NA_{cell}}\,\mathrm{Im}\,\tilde{\Pi}^{R}_{hk}(0,0,\omega). \tag{3.44}$$

According to the linear response theory, the optical conductivity is an equilibrium quantity, and it is dependent on the Fermi level μ, the temperature T, and frequency ω of the perturbation (*i.e.* the electric field). Since we consider a finite temperature, we use the Matsubara formalism [23].

The paramagnetic component of the current density vector in momentum space reads [23]

$$\tilde{\mathbf{J}}^{\nabla}(\mathbf{p}') = -\frac{e}{2m}\int \frac{d\mathbf{p}}{(2\pi)^2}(2\mathbf{p}+\mathbf{p}')c^{\dagger}_{\mathbf{p}}c_{\mathbf{p}+\mathbf{p}'}, \tag{3.45}$$

where $c_{\mathbf{p}}$ ($c^{\dagger}_{\mathbf{p}}$) are destruction (creation) operators in the plane wave representation. In the homogeneous limit (zero transferred momentum, $\mathbf{p}' = \mathbf{0}$), one has [108]

$$\tilde{\mathbf{J}}^{\nabla}(0) = \frac{e}{i\hbar}[H,\mathbf{r}] = -e\dot{\mathbf{r}}, \tag{3.46}$$

where H is the system's Hamiltonian. Eq. (3.46) allows to project the operator $\tilde{\mathbf{J}}^{\nabla}(0)$ onto the tight binding subspace, which is spanned by the basis defined in Eq. (2.12). Thus, similarly to what has been done with the Hamiltonian in Eq. (3.6), one obtains the operator $\mathbf{r}$ in the tight binding subspace. The generic matrix element of $\mathbf{r}$ reads

$$\langle \mathbf{k}\alpha|\mathbf{r}|\mathbf{k}'\beta\rangle = \delta_{\mathbf{k}\mathbf{k}'}\mathbf{r}_{\alpha\beta}(\mathbf{k}), \tag{3.47}$$

where α,β are pseudospin indices, and it is diagonal in the $\mathbf{k}$ variable. The operator $\mathbf{r}$ is explicitly written, in the tight binding subspace, as[1]

$$\mathbf{r}(\mathbf{k}) \;=\; \begin{pmatrix} i\nabla_{\mathbf{k}} & \frac{i}{2}\left(\nabla_{\mathbf{k}}g_{\mathbf{k}}\right) + g_{\mathbf{k}}i\nabla_{\mathbf{k}} \\ \frac{i}{2}\left(\nabla_{\mathbf{k}}g^{*}_{\mathbf{k}}\right) + g^{*}_{\mathbf{k}}i\nabla_{\mathbf{k}} & i\nabla_{\mathbf{k}} \end{pmatrix}. \tag{3.48}$$

Writing explicitly Eq. (3.44), one finds

$$\sigma_{hl}(\omega) = \mathrm{Re}\,\frac{2i}{A_{cell}\hbar\omega}\frac{1}{N}\sum_{\mathbf{k}\lambda}\left[\left(\tilde{J}^{\nabla}_{h}(\mathbf{k})\right)_{\lambda\bar{\lambda}}\left(\tilde{J}^{\nabla}_{l}(\mathbf{k})\right)_{\bar{\lambda}\lambda}\frac{n_F(\xi_{\mathbf{k}\bar{\lambda}}) - n_F(\xi_{\mathbf{k}\lambda})}{\hbar\omega + \xi_{\mathbf{k}\lambda} - \xi_{\mathbf{k}\bar{\lambda}} + i0^{+}}\right], \tag{3.49}$$

where $\xi_{\mathbf{k}\lambda} = E_{\mathbf{k}\lambda} - \mu$ and $n_F(\xi)$ denotes the Fermi function at temperature T. In the direction

[1] The form of the matrix in Eq. (3.48) is independent of the particular choice of the atomic function $\phi(\mathbf{r})$, indeed we have used only the equivalence $\int d\mathbf{r}\phi(\mathbf{r})\mathbf{r}\phi(\mathbf{r}-\boldsymbol{\delta}) = \frac{1}{2}\boldsymbol{\delta}\int d\mathbf{r}\phi(\mathbf{r})\phi(\mathbf{r}-\boldsymbol{\delta})$, which is valid for any rotational invariant two dimensional wave function.

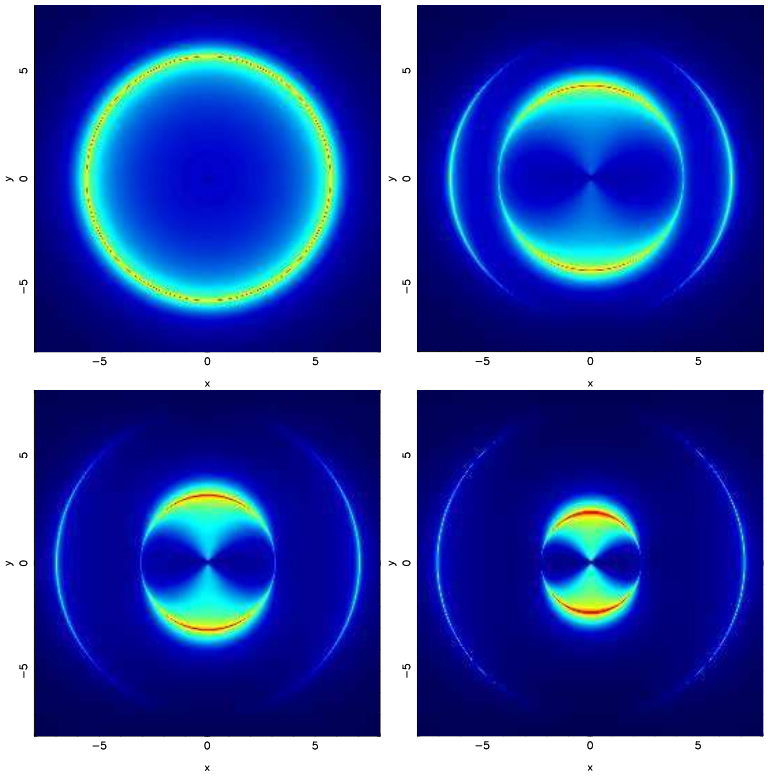

Figure 3.9: Polar plots of the longitudinal optical conductivity σ_{ll}/σ_0, Eq. (5.25), as a function of frequency $\omega > 0$ (polar axis) and electric field orientation ϕ (azymuthal direction). Here, we set $\mu = 0$ and $k_{\rm B}T = 0.025$ eV. Strain is applied along the $\theta = 0$ (armchair) direction, and the strain modulus increases from left to right, and from top to bottom ($\varepsilon = 0, 0.075, 0.175, 0.275$).

of the external field, *i.e.* for $h = l$, one finds[2]

$$\frac{\sigma_{ll}(\omega)}{\sigma_0} = \frac{\pi}{\tau_0^2}\frac{\sinh(\frac{1}{2}\beta\hbar\omega)}{\hbar\omega}\frac{1}{N}\sum_{\mathbf{k}\lambda}\frac{\left|\tilde{j}_l^{\nabla}(\mathbf{k})\right|^2_{\lambda\bar{\lambda}}}{\cosh\left(\frac{1}{2}\beta\xi_{\mathbf{k}\lambda}\right)\cosh\left(\frac{1}{2}\beta\xi_{\mathbf{k}\bar{\lambda}}\right)}\delta\left(\hbar\omega - (E_{\mathbf{k}\lambda} - E_{\mathbf{k}\bar{\lambda}})\right), \quad (3.50)$$

where $\beta = (k_{\rm B}T)^{-1}$ is the inverse temperature, $\tilde{J}_l^{\nabla}(\mathbf{k}) = e\frac{ta}{\hbar}\tilde{j}_l^{\nabla}(\mathbf{k})$, $\sigma_0 = \pi e^2/(2h)$ is proportional to the quantum of conductivity, $\tau_0^{-2} = (1+\varepsilon)(1-\nu\varepsilon)16t^2/(3\sqrt{3}\pi\hbar^2)$.

We have numerically evaluated the longitudinal optical conductivity $\sigma_{ll}(\omega)$, Eq. (5.25) as a function of frequency $\omega > 0$ at fixed temperature $k_{\rm B}T = 0.025$ eV, for several strain moduli ε and directions θ, as well as field orientations, here parametrized by the angle ϕ between the applied electric field and the lattice x direction.

Figs. 3.9 and 3.10 show our results in the case of strain applied in the armchair direction

[2] In this Chapter, we neglect the contribution of the Drude peak.

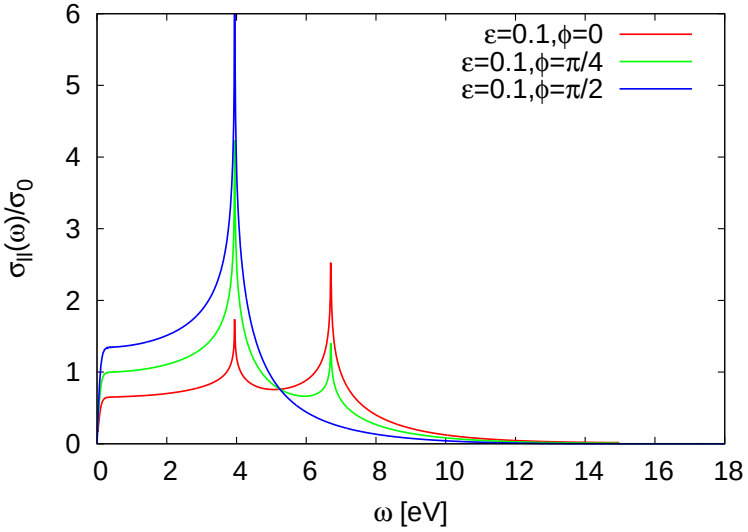

Figure 3.10: Longitudinal optical conductivity σ_{ll}/σ_0, Eq. (5.25), as a function of frequency $\omega > 0$, for fixed strain modulus $\varepsilon = 0.1$ and strain direction $\theta = 0$ (armchair). Different lines refer to various orientations of the electric field ($\phi = 0, \pi/4, \pi/2$).

($\theta = 0$). Fig. 3.9 shows a contour plot of the longitudinal optical conductivity σ_{ll}/σ_0 as a function of frequency ω (radial coordinate) and applied field angle (polar angle). In the relaxed limit ($\varepsilon = 0$), σ_{ll}/σ_0 is isotropic with respect to the applied field angle, and exhibits a maximum at a frequency that can be related to the single Van Hove singularity in the DOS (cf. Fig. 3.7). Such a maximum is immediately split into distinct maxima, in general, as soon as the strain modulus ε becomes nonzero. This can be interpreted in terms of applied strain partly removing the degeneracy among the inequivalent underlying ETTs. Such an effect is however dependent on the field direction ϕ, as is shown already by the anisotropic pattern developed by σ_{ll}/σ_0 in Fig. 3.9, for $\varepsilon \neq 0$. Indeed, Fig. 3.10 shows plots of σ_{ll}/σ_0 as a function of frequency for fixed strain modulus $\varepsilon = 0.1$ and varying field orientation $\phi = 0 - \pi/2$. The relative weight of the two maxima depends on the relative orientation between strain and applied field. Here and below, we consider the case $\mu = 0$. A nonzero value of the chemical potential would result in a vanishing conductivity below a cutoff at $\omega \approx |\mu|$, smeared by finite temperature effects [138].

An analogous behavior is recovered when strain is applied along the zig-zag direction $\theta = \pi/6$, as shown in Figs. 3.11 and 3.12. Again, applied strain breaks down the original isotropy of the optical conductivity with respect to the field orientation in the relaxed case, with two

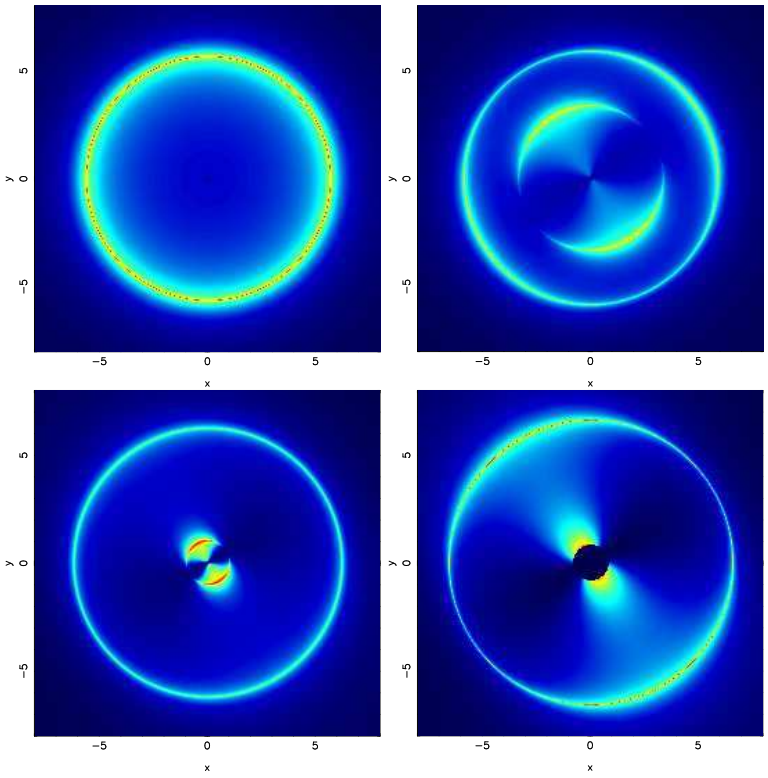

Figure 3.11: Same as Fig. 3.9, but for strain applied the $\theta = \pi/6$ direction. In the last panel, the strain modulus is equal to $\varepsilon = 0.275$, which is larger than critical value $\varepsilon^* \approx 0.228$, thus at low-energies there is a dark spot, because the optical conductivity is vanishing due to the presence of gap.

maxima appearing as a function of frequency (Fig. 3.11). The optical weight of the different maxima depend in general, again, on the relative orientation between strain and applied field. While the presence of the two peaks can be traced back to the existence of inequivalent ETTs, whose degeneracy is here removed by applied strain, the last panel in Fig. 3.11 shows that at a sufficiently large strain modulus (here, $\varepsilon = 0.275$), a gap opens in the low-energy sector of the spectrum, which is signalled here by a vanishing optical conductivity (dark spot at the origin in last panel of Fig. 3.11).

Finally, Figs. 3.13 and 3.14 show the longitudinal optical conductivity in the case of increasing strain applied along a generic direction, *viz.* $\theta = \pi/4$. Like in the previous cases, applied strain removes the isotropy of σ_{ll}/σ_0 with respect to the field orientation ϕ. However, the degeneracy among the three inequivalent ETTs is here lifted completely, and three peaks in general appear in the longitudinal optical conductivity as a function of frequency, as shown also by

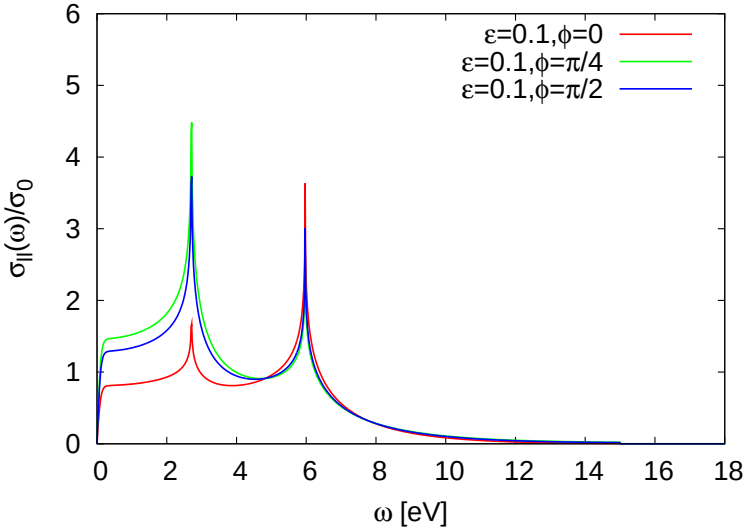

Figure 3.12: Same as Fig. 3.10, but for strain applied the $\theta = \pi/6$ direction.

Fig. 3.14. The redistribution of optical weight among the three peaks is now more complicated, as it in general depends on both the strain direction θ and the field orientation ϕ.

Pereira *et al.* have obtained the electronic bands and the optical conductivity of uniaxially strained graphene from first principles (DFT calculations within LDA approximation) [122, 130]. They have considered strain applied up to $\varepsilon = 0.1$, they have found that the spectrum remains gapless for all strain configurations studied, and their results are well comparable with those obtained using the tight binding model.

Using group theory, it is possible to obtain the analytical form of the optical conductivity for both relaxed and strained graphene [39]. In a two dimensional lattice with hexagonal symmetry such as relaxed graphene, there is only one independent parameter for a symmetric second rank tensor such as the optical conductivity tensor

$$\sigma_{hk}(\omega) = \sigma(\omega)\delta_{hk}, \tag{3.51}$$

thus, one recovers that the longitudinal optical response of relaxed graphene $\sigma(\omega)$ is independent of the polarization of electric field. In a two dimensional lattice with rhombic symmetry there are two independent parameters for a symmetric second rank tensor. This is the case of graphene with strain applied along one of the two special directions (armchair or zig-zag). In

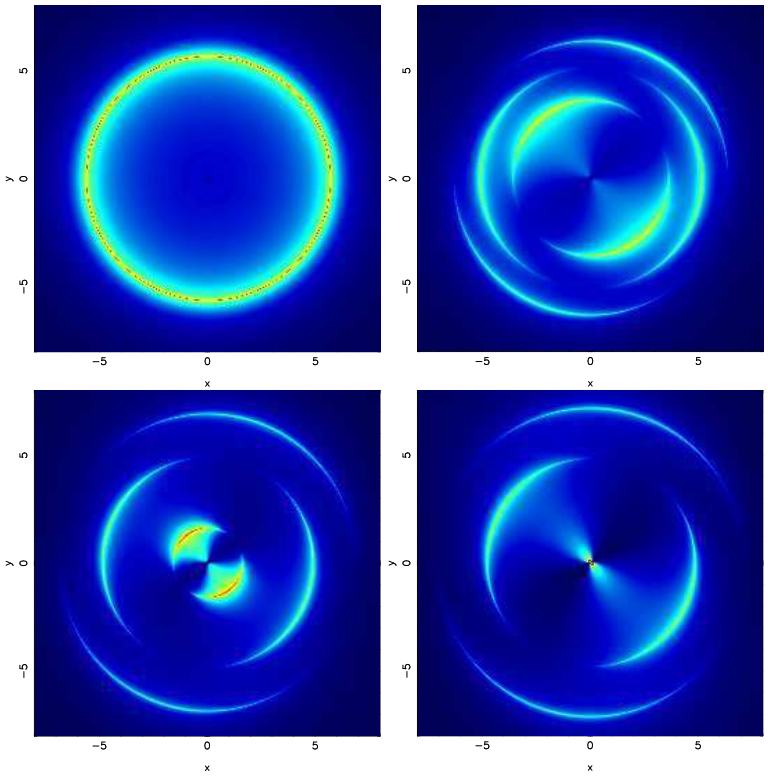

Figure 3.13: Same as Fig. 3.9, but for strain applied the $\theta = \pi/4$ direction.

these special cases the longitudinal optical conductivity can be written as

$$\sigma_{ll}(\omega) = \sigma_{\theta\theta}(\omega)\cos(\phi-\theta)^2 + \sigma_{\bar{\theta}\bar{\theta}}(\omega)\sin(\phi-\theta)^2, \tag{3.52}$$

where ϕ is the direction of the electric field, θ is the stress direction, and $\bar{\theta}$ is the complementary angle of θ (*i.e.* $\bar{\theta} = \theta + \pi/2$). Graphene strained along a generic (not special) direction has only inversion spatial symmetry and consequently its optical conductivity tensor has three independent components. Therefore, the longitudinal optical conductivity along the electric field has a more complicated form

$$\sigma_{ll}(\omega) = \sigma_{\theta\theta}(\omega)\cos(\phi-\theta)^2 + \sigma_{\bar{\theta}\bar{\theta}}(\omega)\sin(\phi-\theta)^2 + \left(\sigma_{\theta\bar{\theta}}(\omega) + \sigma^*_{\theta\bar{\theta}}(\omega)\right)\sin(\phi-\theta)\cos(\phi-\theta). \tag{3.53}$$

The, optical conductivity is related to measurable quantities, such as the transmittance or the reflectance [113]. For instance, we consider light scattering across two media, with refraction

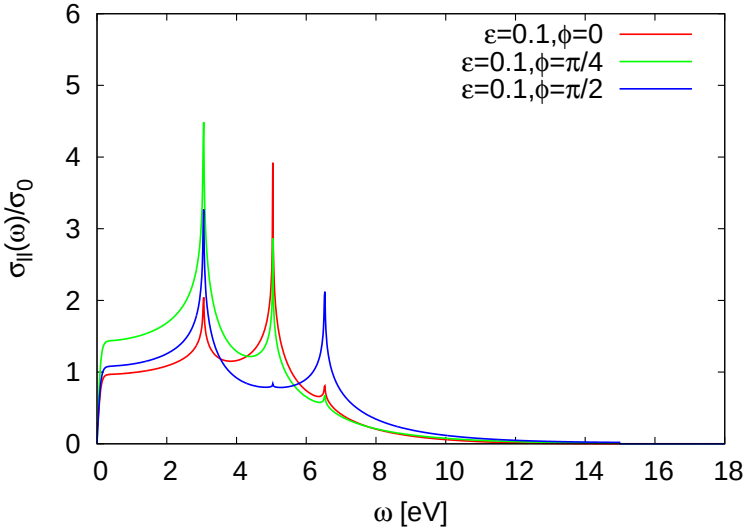

Figure 3.14: Same as Fig. 3.10, but for strain applied the $\theta = \pi/4$ direction.

index $n_i = \sqrt{\epsilon_i}$ $(i = 1, 2)$, separated by a graphene monolayer. In the case of normal incidence, the incident component of the electric field $\mathcal{E}_i$ is related to the reflected component $\mathcal{E}_r = r\mathcal{E}_i$, and to the transmitted component $\mathcal{E}_t = t\mathcal{E}_i$, by the following boundary condition obtained by use of the Maxwell's equations

$$\mathcal{E}_i = \mathcal{E}_r + \mathcal{E}_t. \tag{3.54}$$

Moreover, in this system energy conservation reads

$$\frac{c}{n_1}\epsilon_1\epsilon_0\mathcal{E}_i^2 = \frac{c}{n_1}\epsilon_1\epsilon_0\mathcal{E}_r^2 + \frac{c}{n_2}\epsilon_2\epsilon_0\mathcal{E}_t^2 + \boldsymbol{\mathcal{E}}\cdot\mathbf{J}, \tag{3.55}$$

where c is the speed of light, ϵ_0 is the vacuum permittivity, and $\mathbf{J}$ is the induced current density vector in graphene. The component of the current density vector J_ϕ parallel to the electric field is related to the same electric field by the relation $J_\phi = \sigma_{\phi\phi}(\omega)\mathcal{E}$. Using Eqs. (3.54) and (3.55), one obtains the transmittance and reflectance of such a system, which can be written respectively as

$$T(\omega) = \frac{n_2}{n_1}t^2 = \frac{4n_1n_2}{[n_1 + \pi\alpha\sigma_{\phi\phi}(\omega)/\sigma_0 + n_2]^2}, \tag{3.56}$$

$$R(\omega) = r^2 = \left(\frac{n_1 + \pi\alpha\sigma_{\phi\phi}(\omega)/\sigma_0 - n_2}{n_1 + \pi\alpha\sigma_{\phi\phi}(\omega)/\sigma_0 + n_2}\right)^2. \tag{3.57}$$

where $\alpha = e^2/(4\pi\epsilon_0 c\hbar)$ is the fine structure constant. In the case of suspended graphene,

substituting $n_1 = n_2 = 1$ one finds

$$T(\omega) \approx 1 - \pi\alpha\sigma_{\phi\phi}(\omega)/\sigma_0, \tag{3.58}$$

$$R(\omega) \approx \frac{(\pi\alpha)^2}{4} \left(\sigma_{\phi\phi}(\omega)/\sigma_0\right)^2 . \tag{3.59}$$

Hence, we have seen how uniaxial strain can deeply modify the optical response of graphene. The asymmetry induced by uniaxial strain in the optical conductivity causes an observable degree of dichroism. Indeed, the optical response of uniaxially strained graphene to a linearly polarized light depends on the direction of the polarization [122]. Moreover, the optical response of graphene can give a measure of the magnitude and of the direction of strain in a graphene sample.

Chapter 4

Strain effect on the plasmonic spectrum

Most of the electronic properties of graphene are encoded in the electron polarization, which has been studied within the Dirac cone approximation at zero [57] and finite temperature [147] for pristine graphene, as well as for doped graphene [70, 155]. These results have been recently extended beyond the Dirac cone approximation [139].

In this Chapter, we are concerned with the dynamical polarization of graphene within the full first Brillouin zone of the honeycomb lattice. While electron correlations are treated at the level of the random phase approximation (RPA), we explicitly include local field effects (LFE) [2], which are characteristic of the lattice structure of graphene. The importance of LFE have been shown to be more important in graphene than in bulk semiconductors, in connection with the static dielectric properties of graphene [143, 148]. By discussing the singularities of the polarization, we can identify the longitudinal collective modes of the correlated electron liquid. We are mainly interested in the plasmon modes, which dominate the long wavelength charge density fluctuations. The role of electron-plasmon interaction in renormalizing the (especially low-energy) quasiparticle dispersion relation has been emphasized [20, 22], and plasmons in graphene are potentially interesting for applications in nanophotonics [72].

Specifically, we are interested in the dependence of the plasmon modes on applied uniaxial strain. To this aim we use the tight binding model modified under strain, that we have presented in the previous Chapters. Despite its simplicity, the tight binding model is successful because it is tightly related to the symmetry properties of graphene. In particular, the tight-binding approximation allows to include important features of the electronic band dispersion, such as a

finite bandwidth and the occurrence of Van Hove singularities. These features play an essential role in deriving some of the characteristics of the plasmon dispersion.

4.1 Local field effects on the electron polarization

Within linear response theory, plasmon modes can be described as poles of the density-density correlation function , *i.e.* the polarization. The random phase approximation (RPA) is then the simplest, infinite order, diagrammatic procedure to include electron correlations in the dielectric screening giving rise to the polarization [54]. Besides electron-electron correlations, another source of $\mathbf{k}$-space dependence of the dielectric function is provided by local field effects (LFE) [134]. This is due to the generally atomic consistence of matter and, in the case of solids, to the periodicity of the crystalline lattice. An account of the LFE on the dielectric function of crystalline solids dates back at least to the original paper of Adler [2, 64, 65], and is generalized below to the case of graphene, including both valence and conduction bands.

We start by considering the polarization, which for a noninteracting system at finite temperature T reads

$$\Pi^0_{\rho\rho}(\mathbf{x},\mathbf{x}',i\omega_m) = \frac{1}{\hbar^2\beta}\sum_{i\omega_n}\sum_{\mathbf{k}\lambda\mathbf{k}'\lambda'} \psi^*_{\mathbf{k}\lambda}(\mathbf{x}')\mathcal{G}^0_\lambda(\mathbf{k},i\omega_n)\psi_{\mathbf{k}\lambda}(\mathbf{x})\psi^*_{\mathbf{k}'\lambda'}(\mathbf{x})\mathcal{G}^0_{\lambda'}(\mathbf{k}',i\omega_n+i\omega_m)\psi_{\mathbf{k}'\lambda'}(\mathbf{x}'), \tag{4.1}$$

where $\psi_{\mathbf{k}\lambda}(\mathbf{x})$ is the two-dimensional eigenfunction, $\mathcal{G}^0_\lambda(\mathbf{k},i\omega_n) = (i\omega_n - \xi_{\mathbf{k}\lambda}/\hbar)^{-1}$ is the Green's function for the noninteracting system, and $\hbar\omega_n = (2n+1)\pi k_{\rm B}T$ [$\hbar\omega_m = 2m\pi k_{\rm B}T$] denote the fermionic [bosonic] Matsubara frequencies at temperature T, with $\hbar$ Planck's constant and $k_{\rm B}$ Boltzmann's constant. In treating systems at finite temperatures, it is convenient to use the grand canonical ensemble [46]. Hence we use as a natural variable the single-particle energy $\xi_{\mathbf{k}\lambda}$, which is defined as $\xi_{\mathbf{k}\lambda} = E_{\mathbf{k}\lambda} - \mu$, where μ is the chemical potential, and $E_{\mathbf{k}\lambda}$ is the electronic dispersion relation where $\lambda = 1$ refers to the valence band and $\lambda = 2$ refers to the conduction band. Fourier transforming into momentum space Eq. (4.1), and performing the

summation over the Matsubara frequencies, one finds

$$\Pi^0_{\rho\rho}(\mathbf{q}+\mathbf{G},-\mathbf{q}'-\mathbf{G}',i\omega_m) = (2\pi)^2 A_{cell}^{-1}\delta(\mathbf{q}-\mathbf{q}') \times\frac{1}{N}\sum_{\mathbf{k}\lambda\lambda'} T_{\mathbf{k}\lambda,\mathbf{k}-\mathbf{q}\lambda'}(i\omega_m)\langle\mathbf{k}-\mathbf{q}\lambda'|e^{-i(\mathbf{q}+\mathbf{G})\cdot\hat{\mathbf{r}}}|\mathbf{k}\lambda\rangle\langle\mathbf{k}\lambda|e^{i(\mathbf{q}+\mathbf{G}')\cdot\hat{\mathbf{r}}}|\mathbf{k}-\mathbf{q}\lambda'\rangle, \tag{4.2}$$

where

$$T_{\mathbf{k}\lambda,\mathbf{k}-\mathbf{q}\lambda'}(i\omega_m) = \frac{n_{\rm F}(\xi_{\mathbf{k}-\mathbf{q}\lambda'}) - n_{\rm F}(\xi_{\mathbf{k}\lambda})}{i\hbar\omega_m + \xi_{\mathbf{k}-\mathbf{q}\lambda'} - \xi_{\mathbf{k}\lambda}}. \tag{4.3}$$

Here, $n_{\rm F}(\omega)$ is the Fermi function, $A_{cell} = 3\sqrt{3}a^2/2$ is the area of the unit cell, $\mathbf{q}$, $\mathbf{q}'$ belong to the first Brillouin zone (1BZ), $\mathbf{G}$, $\mathbf{G}'$ are vectors of the reciprocal lattice, and LFE are embedded in the Adler's weights [2]

$$\begin{aligned}\langle\mathbf{k}-\mathbf{q}\lambda'|e^{-i(\mathbf{q}+\mathbf{G})\cdot\hat{\mathbf{r}}}|\mathbf{k}\lambda\rangle &= \int d^2\mathbf{x} e^{-i(\mathbf{q}+\mathbf{G})\cdot\mathbf{x}}\psi_{\mathbf{k}\lambda}(\mathbf{x})\psi^*_{\mathbf{k}-\mathbf{q}\lambda'}(\mathbf{x}) \\ &\simeq \frac{1}{2}\left[(-1)^{\lambda-\lambda'} + e^{i(\theta_{\mathbf{k}-\mathbf{q}}-\theta_{\mathbf{k}})-i\mathbf{G}\cdot\boldsymbol{\delta}_3}\right] e^{-\sigma_g^2|\mathbf{q}+\mathbf{G}|^2/4},\end{aligned} \tag{4.4}$$

where in the last line only the onsite overlap between pairs of atomic orbitals (3.9), centered on either sublattices, has been retained, on account of their localized character, we have retained only the lowest (zeroth) order contributions in the overlap function $g_{\mathbf{k}}$, and $e^{i\theta_{\mathbf{k}}} = -f_{\mathbf{k}}/|f_{\mathbf{k}}|$. Using a more compact notation, one may also write

$$\Pi^0_{\rho\rho}(\mathbf{q}+\mathbf{G},-\mathbf{q}'-\mathbf{G}',i\omega_m) = (2\pi)^2 A_{cell}^{-1}\delta(\mathbf{q}-\mathbf{q}')\sum_{\alpha\beta}\rho_{\mathbf{q}\alpha}(\mathbf{G})Q^0_{\alpha\beta}(\mathbf{q},i\omega_m)\rho^*_{\mathbf{q}\beta}(\mathbf{G}'), \tag{4.5}$$

where

$$Q^0_{\alpha\beta}(\mathbf{q},i\omega_m) = \frac{1}{N}\sum_{\mathbf{k}\lambda\lambda'} u^{\alpha}_{\mathbf{k}\lambda}u^{\beta *}_{\mathbf{k}\lambda}u^{\alpha *}_{\mathbf{k}-\mathbf{q}\lambda'}u^{\beta}_{\mathbf{k}-\mathbf{q}\lambda'}T_{\mathbf{k}\lambda,\mathbf{k}-\mathbf{q}\lambda'}(i\omega_m), \tag{4.6}$$

with $u^{\alpha}_{\mathbf{k}\lambda}$ the components of $\mathbf{u}_{\mathbf{k}\lambda}$, which are solutions of the generalized eigenvalue problem (2.21), and

$$\rho_{\mathbf{q}\alpha}(\mathbf{G}) = \exp(-i\mathbf{G}\cdot\boldsymbol{\delta}_\alpha - \sigma_g^2|\mathbf{q}+\mathbf{G}|^2/4) \tag{4.7}$$

are the LFE weights. The indices α and β refer to the pseudo-spin space ($\alpha,\beta = A,B$), whereas the indices λ and λ' refer to the conduction and valence bands ($\lambda,\lambda' = 1,2$). Moreover, we also set $\boldsymbol{\delta}_A = \mathbf{0}$ and $\boldsymbol{\delta}_B = \boldsymbol{\delta}_3$. The continuum limit is recovered when $\mathbf{G} = \mathbf{G}' = 0$.

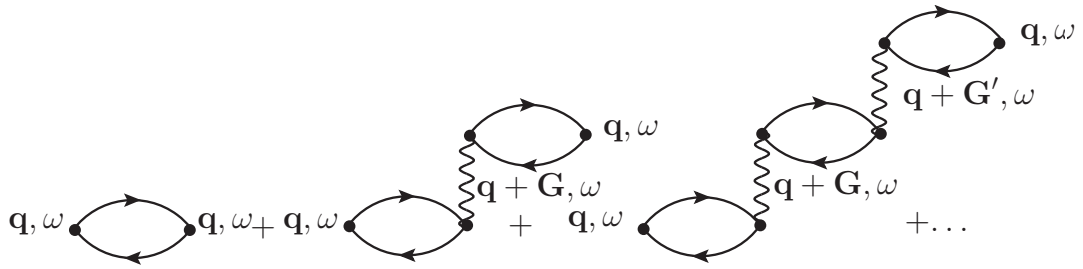

Figure 4.1: Diagrammatic representation of the random phase approximation (RPA), including local field effects (LFE), for the electron polarization. The exchange momentum in the interaction terms can be outside the first Brillouin zone (1BZ). Indeed, $\mathbf{q}$ belongs to the 1BZ, whereas $\mathbf{G}$, $\mathbf{G}'$ are vectors of the reciprocal lattice.

Many-body correlations are then included within RPA, yielding a renormalized polarization

$$\Pi_{\rho\rho}(\mathbf{q}+\mathbf{G},-\mathbf{q}'-\mathbf{G}',i\omega_m) = (2\pi)^2 A_{cell}^{-1}\delta(\mathbf{q}-\mathbf{q}')\sum_{\alpha\beta}\rho_{\mathbf{q}\alpha}(\mathbf{G})Q_{\alpha\beta}(\mathbf{q},i\omega_m)\rho^*_{\mathbf{q}\beta}(\mathbf{G}'), \quad (4.8)$$

where now

$$Q(\mathbf{q},i\omega_m) = g_s Q^0(\mathbf{q},i\omega_m)\left[\mathbb{1} - g_s A_{cell}^{-1} V(\mathbf{q}) Q^0(\mathbf{q},i\omega_m)\right]^{-1}, \quad (4.9)$$

where matrix products are being understood, $g_s = 2$ is a factor for spin degeneracy, and

$$V_{\alpha\beta}(\mathbf{q}) = \sum_{\mathbf{G}''}\rho^*_{\mathbf{q}\alpha}(\mathbf{G}'')V_0(\mathbf{q}+\mathbf{G}'')\rho_{\mathbf{q}\beta}(\mathbf{G}'') \quad (4.10)$$

is the renormalized Coulomb potential, $V_0(\mathbf{q}) = e^2/(2\varepsilon_0\epsilon_r q)$, now a matrix over band indices. Here, $\epsilon_r = (\epsilon_{r1}+\epsilon_{r2})/2$ denotes the average relative dielectric constants of the two media surrounding the graphene layer, *viz.* air for suspended graphene ($\epsilon_{r1} = \epsilon_{r2} = \epsilon_r = 1$). In the case of a stronger dielectric substrate, we expect therefore a softening of the correlation effects on the plasmon frequency. It is relevant to note that the renormalized potential already includes LFE. Finally, the approximation used to obtain the electron polarization in Eq. (4.8) is shown diagrammatically in Fig. 4.1.

4.1.1 Plasmons

Plasmons are defined as collective excitations of the electron liquid corresponding to poles of the retarded polarization,

$$\Pi_{\rho\rho}(\mathbf{q},\omega) \equiv \Pi_{\rho\rho}(\mathbf{q},-\mathbf{q},i\omega_m \to \omega + i0^+), \tag{4.11}$$

where $\mathbf{q} \in$ 1BZ. Here and in what follows we shall restrict to the case $\mathbf{G} = \mathbf{G}' = 0$. Indeed, it is apparent from the definition of $\Pi_{\rho\rho}(\mathbf{q},\omega)$ that its poles can only arise from the vanishing of $\det[\mathbb{1} - V(\mathbf{q})Q^0(\mathbf{q},\omega)]$ in Eq. (4.9), which already contains LFE via the renormalized Coulomb potential, Eq. (4.10). We therefore define the dispersion relation $\omega_\ell(\mathbf{q})$ of the ℓ-th plasmon branch as

$$\Pi^{-1}_{\rho\rho}\left(\mathbf{q},\omega_\ell(\mathbf{q})\right) = 0. \tag{4.12}$$

This clearly involves vanishing of both real and imaginary parts of the inverse polarization. It will be useful to define the dispersion relation $\tilde{\omega}_\ell(\mathbf{q})$ of damped plasmons through

$$\mathrm{Re}\,\left[\Pi^{-1}_{\rho\rho}\left(\mathbf{q},\tilde{\omega}_\ell(\mathbf{q})\right)\right] = 0. \tag{4.13}$$

Correspondingly, the inverse lifetime $\tau^{-1}(\mathbf{q},\omega)$ of such damped plasmons is proportional to $-\mathrm{Im}\,\Pi_{\rho\rho}(\mathbf{q},\omega)$, for $\omega = \tilde{\omega}_\ell(\mathbf{q})$.

Fig. 4.2 shows our numerical results for the plasmon dispersion relation in doped suspended graphene ($\mu = 1$ eV, $\epsilon_{r1} = \epsilon_{r2} = 1$, $\mu = 1$ eV) at finite temperature ($T = 3$ K) along a symmetry contour in the 1BZ, without LFE [$\mathbf{G}'' = 0$ in Eq. (4.10), left panel] and including LFE (right panel). At small wavevectors and low frequencies, one recognizes a square-root plasmon mode $\omega_1(\mathbf{q}) \sim \sqrt{q}$, typical of a 2D system [54]. This is in agreement with earlier studies of the dynamical screening effects in graphene at RPA level, employing an approximate conic dispersion relation for electrons around the Dirac points [70, 155]. Such a result has been confirmed also for a tight-binding band [69, 139], and is here generalized with the inclusion of LFE.

The high energy ($5 - 20$ eV) pseudo-plasmon mode, extending throughout the whole 1BZ, is rather associated with a logarithmic singularity of the bare polarization $Q^0(\mathbf{q},\omega)$ in Eq. (4.9),

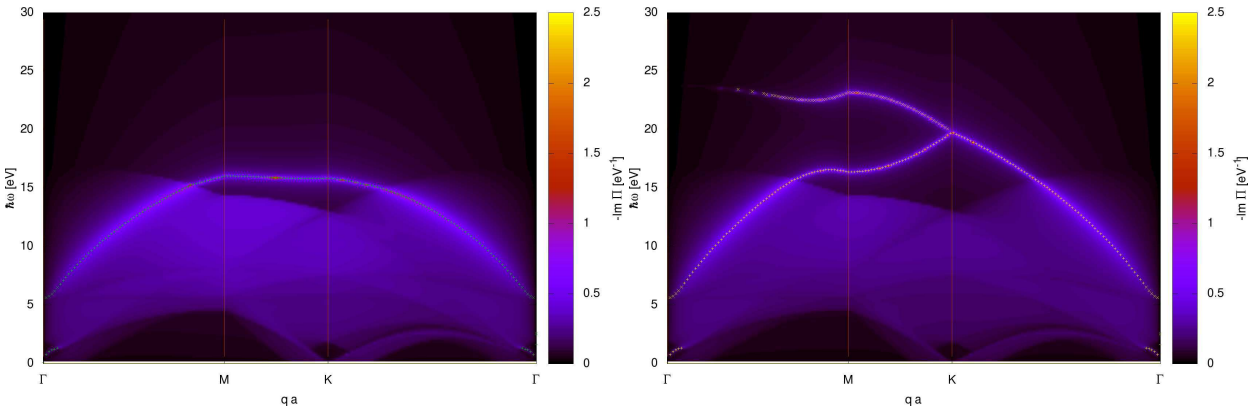

Figure 4.2: Plasmon dispersion relation for suspended doped graphene ($\mu = 1$ eV, $\epsilon_{r1} = \epsilon_{r2} = 1$) at finite temperature ($T = 3$ K), not including (left panel) and including (right panel) LFE. Results are shown along a symmetry contour in the 1BZ, with $\Gamma = (0, 0)$, $M = (2\pi/3a, 0)$, and $K = (2\pi/3a, 2\pi/3\sqrt{3}a)$. Energies $\hbar\omega$ are in eV. The shaded background is a contour plot of $-\mathrm{Im}\,\Pi_{\rho\rho}(\mathbf{q}, \omega)$ (arbitrary scale), while continuous lines are the dispersion relation of damped plasmons, $\tilde{\omega}_\ell(\mathbf{q})$, Eq. (4.13), is shown as a dotted line.

and therefore does not correspond to a true pole of the polarization. This collective mode can be related to an interband transition between the Van Hove singularities in the valence and conduction bands of graphene, and has been identified with a $\pi \to \pi^*$ transition [49, 139].

At large wavevectors, specifically along the zone boundary between the M and the K (Dirac) points, full inclusion of LFE determines the appearance of a second, high-frequency ($20 - 25$ eV), optical-like plasmon mode $\omega_2(\mathbf{q})$, weakly dispersing as $q \to 0$.

Multiple plasmon modes are a generic consequence of the possibility of interband transitions, whenever several such bands are available. This is *e.g.* the case of quasi-2D quantum wells (2DQW), whose energy spectrum is characterized by quantized levels in the direction perpendicular to the plane of the well, while electrons can roam freely within the plane [54]. In this case, collective modes arise as zeroes of the determinant of the dielectric function. At low temperatures, at most the two lowest subbands need to be considered. One usually obtains an 'acoustic' mode associated to intrasubband coupling, and a 'optical' mode associated to intersubband coupling [146]. Such a situation is here paralleled by the case of graphene, the role of the two subbands of 2DQW being here played by the valence and conduction bands, touching at the Dirac points in the neutral material. It should be noticed that the plasmon mode due to interband coupling is suppressed when LFE are neglected. In 2DQW, the discrete nature of the

electronic subbands is due to the real-space confinement of the electron liquid in the direction perpendicular to the plane, *i.e.* to the *quasi*-2D character of the quantum well. In graphene, the origin of the two bands ultimately lies in the specific lattice structure of this material. Therefore, the high-energy, 'optical' plasmon mode disappears in the absence of LFE (Fig. 4.2, top panel), as expected whenever the lattice structure of graphene is neglected. In other words, while in the absence of LFE only scattering processes with momenta within the 1BZ are considered, LFE allow to include all scattering processes with arbitrarily low wavelengths, thereby taking into account the discrete nature of the crystalline lattice. Such a structure needs not be considered in the case of a 2DQW. Our finding of a high-energy 'optical' plasmon branch, as a generic consequence of the two-band electronic structure of graphene, should stimulate further investigation of the electronic collective modes in graphene [41, 69], in view of the role of electron-electron correlations in interpreting the results of electron spectroscopy for interband transitions [126].

Beyond two dimensionality

Usually the electronic system in graphene is considered as a two-dimensional electron gas. In this paragraph, we take into account a full three dimensional representation for the wave functions of the single particles. The generic electron wave function, corresponding to a λ band, is written as

$$\Psi_{\mathbf{k}\lambda}(\mathbf{r}) = \psi_{\mathbf{k}\lambda}(\mathbf{x})\Phi_{\mathbf{k}\lambda}(z), \tag{4.14}$$

where $\psi_{\mathbf{k}\lambda}(\mathbf{x})$ is the two-dimensional eigenfunction, which has been previously defined, and $\Phi_{\mathbf{k}\lambda}(z)$ describes the z-dependence of the electron wave function.

Neglecting the z-dimension is equivalent to approximate the $\Phi_{\mathbf{k}\lambda}(z)$ so that its square modulus is a Dirac delta function

$$|\Phi_{\mathbf{k}\lambda}(z)|^2 \approx \delta(z). \tag{4.15}$$

A simple approximation to describe the finite extension of the electron wave function along the z-direction is an exponential function

$$\Phi_{\mathbf{k}\lambda}(z) = \mathrm{sgn}\,(z)\sqrt{\frac{\kappa_z}{2}}e^{-\frac{\kappa_z}{2}|z|}, \tag{4.16}$$

where we consider κ_z as a constant. In particular we set $\kappa_z = 3$ Å^{-1}, which is in good agreement with *ab initio* calculations [153]. In limit $\kappa_z \to \infty$, the square modulus of $\Phi_{\mathbf{k}\lambda}(z)$ becomes the Dirac delta function. In addition, one can see that the electron wave functions are odd under reflection symmetry with respect to the basal plane, like the p_z wave functions.

Taking into account the finite extension of the electron wave function along the z-direction, the renormalized polarization maintains the expression in Eq. (4.8), but the two dimensional Coulomb potential $V_0(\mathbf{q}) = e^2/[\varepsilon_0(\epsilon_{r1} + \epsilon_{r2})q]$ is replaced by a more complex formula

$$V_0(\mathbf{q}) = \frac{e^2}{\varepsilon_0(\epsilon_{r1} + \epsilon_{r2})q} \left[\frac{\kappa_z(2\kappa_z + q)}{2(\kappa_z + q)^2} + \frac{(\epsilon_{r1} - \epsilon_{r2})^2}{8\epsilon_{r1}\epsilon_{r2}} \frac{\kappa_z q}{(\kappa_z + q)^2} \right], \tag{4.17}$$

where ϵ_{r1} and ϵ_{r2} denote the relative dielectric constants of the two media surrounding the graphene layer. The correction to the Coulomb potential in Eq. (4.17) is negligible at small momenta, $q \ll \kappa_z$, whereas its contribution is sizable for large momenta, $q \gg \kappa_z$. Hence, the scattering processes with large exchange momentum are particularly interested by the correction in Eq. (4.17).

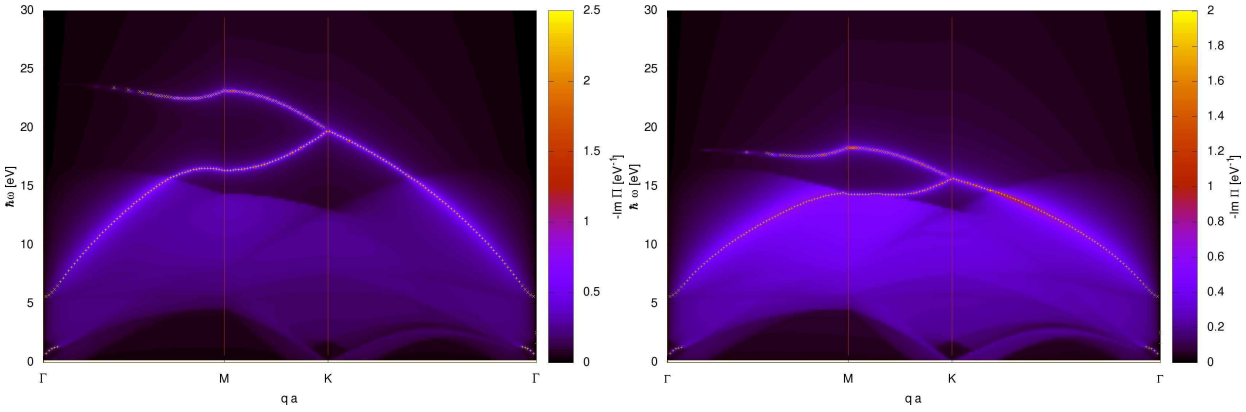

Figure 4.3: Plasmon dispersion relation for suspended doped graphene ($\mu = 1$ eV, $\epsilon_{r1} = \epsilon_{r2} = 1$) at finite temperature ($T = 3$ K), not including (left panel) and including (right panel) the z-extension of the electron wave functions, considering the LFE. Results are shown along a symmetry contour in the 1BZ, with $\Gamma = (0, 0)$, $M = (2\pi/3a, 0)$, and $K = (2\pi/3a, 2\pi/3\sqrt{3}a)$. Energies $\hbar\omega$ are in eV. The shaded background is a contour plot of $-\mathrm{Im}\,\Pi_{\rho\rho}(\mathbf{q}, \omega)$ (arbitrary scale), while continuous lines are the dispersion relation of damped plasmons, $\tilde{\omega}_\ell(\mathbf{q})$, Eq. (4.13), is shown as a dotted line.

Fig. 4.3 shows our numerical results for the plasmon dispersion relation in suspended doped graphene ($\mu = 1$ eV, $\epsilon_{r1} = \epsilon_{r2} = 1$) at finite temperature ($T = 3$ K) along a symmetry contour in the 1BZ, without (left panel) and with (right panel) the z-extension of the electron

wave functions, and both including the LFE. By a comparison of both panels in Fig. 4.3, at low energies and small wavevectors the contribution due to the z-extension of the electron wave functions has no appreciable effect. On the other hand, at high energies there is a quantitative, but not qualitative, modification of the plasmon dispersion relation due to the z-extension of the electron wave functions. In particular, there is an energy lowering of the 'optical' plasmon branch because of the correction on the Coulomb potential in Eq. (4.17). Moreover, one may observe that the high energy plasmon branch maintains the same form, since the features of this collective excitation are related to the LFE, more generally to the lattice symmetry.

Moreover, a quantitative improvement for the description of the high energy collective excitations could be obtained adding in the tight binding model the next neighbors terms, or further terms. However, these terms would make the model more complicated without adding new features of the π electronic structure. Indeed, our tight binding model contains all principal properties of the π electronic structure, *i.e.* the Dirac cones and the saddle points.

Finally, a qualitative improvement for the description of the high energy plasmon branch could be obtained taking into account the σ electrons beyond the π electrons. In particular, these further electronic bands could heavily change the structure of the high energy plasmon dispersion relation, and they could induce a finite lifetime to these collective excitations because of the further promotion of electrons from the valence band into the higher (σ^*) energy band.

4.1.2 Asymptotic behaviors

In certain limiting regimes, one may derive the asymptotic behavior of the polarization in close form. At low energies ($\hbar\omega \lesssim |t|$) and small wavevectors ($q \to 0$, *i.e.* $qa \ll 1$), LFE and z-extension can be neglected. The matrix product entering the definition of the polarization through Eq. (4.9) then reduces to

$$\begin{aligned} g_s A_{cell}^{-1} V(\mathbf{q}) Q^0(\mathbf{q},\omega) &= g_s A_{cell}^{-1} V_0(\mathbf{q}) \sum_{\alpha\beta} Q^0_{\alpha\beta}(\mathbf{q},\omega) \\ &= \frac{\tilde{V}_0}{qa}\frac{1}{N}\sum_{\mathbf{k}\lambda} \delta_T(\xi_{\mathbf{k}\lambda}) \left(\frac{\mathbf{q}\cdot\nabla_{\mathbf{k}} E_{\mathbf{k}\lambda}}{\hbar\omega}\right)^2, \end{aligned} \tag{4.18}$$

where $\tilde{V}_0 = g_s(8\pi/3\sqrt{3})(a_0/a)$ Ry, a_0 being Bohr's radius, and $\delta_T(\epsilon) \equiv -\partial n_{\rm F}(\epsilon)/\partial\epsilon \to \delta(\epsilon)$, as $T \to 0$. In the latter limit, the δ-function effectively restricts the integration over wavevectors along the Fermi line. Whenever the cone approximation holds (*i.e.*, for sufficiently low chemical potential and strain; see Chapter 3), this can be taken as the constant-energy ellipse in Eq. (3.21). The $\mathbf{k}$-integration in Eq. (4.18) can then be performed analytically, and the retarded polarization, Eq. (4.11), then reads

$$\Pi_{\rho\rho}(\mathbf{q},\omega) \approx \frac{g_s A_{cell}^{-1}\tilde{V}_0^{-1}\tilde{\omega}_1^2 q^2 a^2}{\hbar^2\omega^{+2} - \hbar^2\omega_1^2(\mathbf{q})}, \tag{4.19}$$

where $\omega^+ \equiv \omega + i0^+$, and

$$\hbar\tilde{\omega}_1 = \left(\tilde{V}_0\rho(\mu)\right)^{1/2} |\nabla_{\mathbf{q}} E_{\mathbf{q}2}/a|, \tag{4.20}$$

with $\rho(\mu)$ the density of states (DOS) at the Fermi level. To leading order in qa, from Eq. (4.19) one thus obtains

$$\omega_1(\mathbf{q}) \approx \tilde{\omega}_1\sqrt{qa} \tag{4.21}$$

for the acoustic-like plasmon dispersion relation. One thus recovers the square-root behavior of the plasmon dispersion relation, as is typical in 2D electron systems [54]. Moreover, one recovers the dependence of the coefficient $\tilde{\omega}_1 \sim n^{1/4}$ on the carrier density n, rather than $\sim n^{1/2}$, as is the case for a parabolic dispersion relation of the quasiparticles [35, 70]. The acoustic-like plasmon mode may be related to the Drude weight [1], thus enabling the observation of strain effects from optical measurements [114]. In the case of graphene on a dielectric substrate ($\epsilon_r > 1$), one has a reduction of $\tilde{\omega}_1$, thus a softening of the plasmon mode. From Eq. (4.19) one may also read off the imaginary part of the retarded polarization, which close to the 'acoustic' plasmon mode [$\omega \sim \omega_1(\mathbf{q})$] reads

$$\mathrm{Im}\,\Pi_{\rho\rho}(\mathbf{q},\omega^+) \approx -\frac{\pi}{2} g_s A_{cell}^{-1}\tilde{V}_0^{-1/2}\tilde{\omega}_1(qa)^{3/2}\delta\left(\omega - \omega_1(\mathbf{q})\right). \tag{4.22}$$

We now turn to the asymptotic behavior of the second branch of the plasmonic spectrum, $\omega_2(\mathbf{q})$. We have already established that it displays an optical-like character, with $\omega_2(\mathbf{q}) \to \omega_2(0)$, as $q \to 0$. Here, $\omega_2(0)$ is greater than the distance between the top of the conduction band and the bottom of the valence band. At small wavevectors, it is useful to consider the

expansions of the relevant terms in Eq. (4.9), which to leading order in q_i ($i = x, y$) read

$$Q^0_{AA}(\mathbf{q},\omega) \approx Q_{AA}(0,\omega) + \sum_{ij} q_i y_{ij}(\omega) q_j, \tag{4.23a}$$

$$Q^0_{AB}(\mathbf{q},\omega) \approx -Q_{AA}(0,\omega) + \sum_{ij} q_i z_{ij}(\omega) q_j, \tag{4.23b}$$

where $y_{ij}(\omega)$, $z_{ij}(\omega)$ are real valued functions of the frequency ω, and

$$Q^0_{AA}\left(0,\omega_2(0)\right) = \frac{1}{4N}\sum_{\mathbf{k}\lambda} \frac{n_{\mathrm{F}}(\xi_{\mathbf{k}\bar{\lambda}}) - n_{\mathrm{F}}(\xi_{\mathbf{k}\lambda})}{\omega_2(0) + \xi_{\mathbf{k}\bar{\lambda}} - \xi_{\mathbf{k}\lambda}}. \tag{4.24}$$

The asymptotically constant value of the optical-like plasmon frequency is then implicitly given by

$$1 - 4Q^0_{AA}\left(0,\omega_2(0)\right) g_s A^{-1}_{cell} \sum_{\mathbf{G}} V_0(\mathbf{G}) \sin^2\left(\frac{1}{2}\mathbf{G}\cdot\boldsymbol{\delta}_3\right) = 0, \tag{4.25}$$

whereas the imaginary part of the retarded polarization, close to the second plasmon branch [$\omega \sim \omega_2(0)$], to leading order in q, reads

$$\begin{aligned}\mathrm{Im}\,\Pi_{\rho\rho}(\mathbf{q},\omega^+) \approx & -\pi g_s A^{-1}_{cell} \left| \frac{1}{4N}\sum_{\mathbf{k}\lambda} \frac{n_{\mathrm{F}}(\xi_{\mathbf{k}\bar{\lambda}}) - n_{\mathrm{F}}(\xi_{\mathbf{k}\lambda})}{(\omega_2(0) + \xi_{\mathbf{k}\bar{\lambda}} - \xi_{\mathbf{k}\lambda})^2} \right|^{-1} \\ & \times \sum_{ijhk} q_i q_h (z_{ij} - y_{ij})(z_{hk} + y_{hk}) q_j q_k \delta\left(\omega - \omega_2(0)\right).\end{aligned} \tag{4.26}$$

In particular, it follows that the spectral weight of $\mathrm{Im}\,\Pi_{\rho\rho}$ close to $\omega_2(0)$ decreases as $\sim q^4$, as $q \to 0$, rather than as $\sim q^{3/2}$, as is the case for the acoustic-like plasmon mode, Eq. (4.22). This justifies the reduced spectral weight associated with the second plasmon branch at small wavevector in Fig. 4.3.

In the case of graphene on a dielectric substrate ($\epsilon_r > 1$), inspection of Eqs. (4.24) and (4.25) yields a reduction of $\omega_2(0)$.

Usually, experimental methodologies to detect plasmon dispersion relation, such as electron energy loss spectroscopy (EELS), measure the collective excitation at small wavevector limit ($q \to 0$) [41]. In graphene, to date there are measurements about the low energy plasmon [30, 59] and the pseudo-plasmon excitation [41], whereas there is no clear experimental evidence about the high energy plasmon. The detection of the high energy branch at small wavevector

could be difficult not only because of the reduced spectral weight associated with the high energy branch, but also because these plasmons could be damped by the further promotions of electrons from the valence band into the higher (σ^*) energy band. In this Thesis we have not considered the electronic bands due to the σ electrons, and this possible correction will be subject of future work.

4.2 Effect of strain on the plasmon dispersion relation

We now turn to consider the effect of strain on the plasmon dispersion relation. As in Refs. [110, 121], applied uniaxial strain can be modeled by explicitly considering the dependence on the strain tensor $\boldsymbol{\varepsilon}$ of the tight-binding parameters $t_\ell = t(\boldsymbol{\delta}_\ell)$ through the vectors $\boldsymbol{\delta}_\ell$ connecting two NN sites ($\ell = 1, 2, 3$). A linear dependence of $\boldsymbol{\delta}_\ell$ on $\boldsymbol{\varepsilon}$ is justified in the elastic limit. Such an assumption is however quite robust, due to the extreme rigidity of graphene [19], and is supported by *ab initio* calculations [27, 75].

Below, the strain tensor $\boldsymbol{\varepsilon}$ will be parametrized by a strain modulus ε, and by the angle θ between the direction of applied strain and the x axis in the lattice coordinate system. Specifically, one has $\theta = 0$ [*resp.*, $\theta = \pi/6$] for strain applied along the armchair [*resp.*, zig-zag] direction.

Fig. 4.4 shows the dispersion relation of the plasmon branches studied in § 4.1.1, including LFE and z-extension, along a symmetry contour of the 1BZ, for strain applied along the armchair direction ($\theta = 0$), with increasing strain modulus ($\varepsilon = 0 - 0.275$). The low-frequency, 'acoustic' plasmon mode $\omega_1(\mathbf{q})$ is not qualitatively affected by the applied strain. In particular, the dominant square-root behavior is independent with respect to the opening of a gap. On the other hand, one observes an increase of spectral weight associated with the high-frequency, 'optical' plasmon mode $\omega_2(\mathbf{q})$ at small wavevectors. The overall flattening of the second plasmon branch over the symmetry contour under consideration can be traced back to the strain-induced shrinking of both valence and conduction bands.

A qualitatively similar analysis applies to the case of strain applied along the zig-zag direction ($\theta = \pi/6$, Fig. 4.5), and for strain applied along a generic direction ($\theta = \pi/4$, Fig. 4.6), with $\omega_2(\mathbf{q})$ dispersing more weakly as the strain increases.

Finally, we turn to study the $\mathbf{q}$-dependence of the low-frequency, 'acoustic' mode $\omega_1(\mathbf{q}) \equiv$

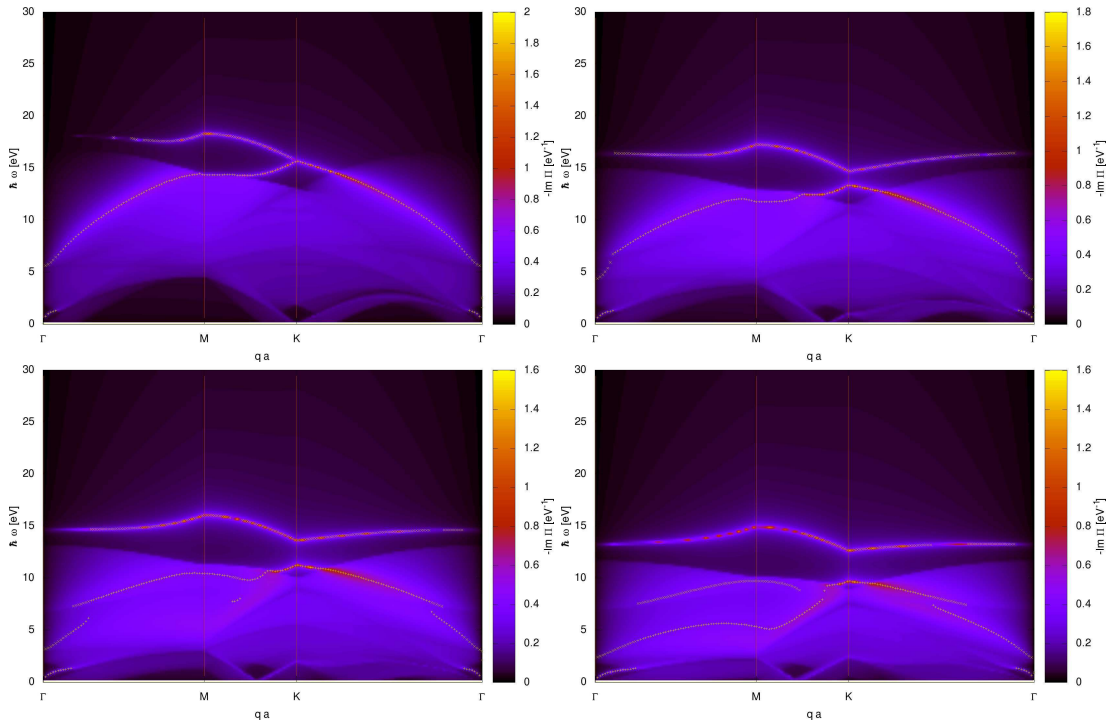

Figure 4.4: Plasmon dispersion relation for suspended doped graphene ($\mu = 1$ eV, $\epsilon_{r1} = \epsilon_{r2} = 1$), including LFE and z-extension, with strain applied along the $\theta = 0$ (armchair) direction. Strain increases (from left to right, from top to bottom) as $\varepsilon = 0,\ 0.075,\ 0.175,\ 0.275$.

$\omega_1(q, \varphi_{\mathbf{q}})$ under applied strain, where $q = |\mathbf{q}|$ and $\varphi_{\mathbf{q}}$ denotes the angle between $\mathbf{q}$ and the $\hat{x}$ axis. Fig. 4.7 shows then the dispersion relation of the lower plasmon branch as a function of q for several values of $\varphi_{\mathbf{q}}$, for increasing strain applied along the armchair direction ($\theta = 0$). While the overall square-root shape $\omega_1 \approx \tilde{\omega}_1\sqrt{qa}$, Eq. (4.21), is maintained in all cases, one observes a stiffening of such plasmonic mode with increasing strain and a maximum of the coefficient $\tilde{\omega}_1$, Eq. (4.20), when $\varphi_{\mathbf{q}} - \theta \approx \pi/2$. The same description qualitatively applies also to the cases of strain applied along the armchair ($\theta = \pi/6$), and along a generic ($\theta = \pi/4$) direction. Such a behavior can be justified analytically in the limit of no LFE (cf. Sec. 4.1.2), and corresponds to the strain dependence obtained for the optical conductivity [110]. Indeed, from Eq. (4.20), one may notice that all the strain dependence is contained in the modulus square of the quasiparticle dispersion relation of the conduction band at the Fermi level, $|\nabla_{\mathbf{q}} E_{\mathbf{k}2}/a|$. One finds

$$\tilde{\omega}_1 \propto |\nabla_{\mathbf{q}} E_{\mathbf{q}2}| = \left(\frac{\cos^2(\varphi_{\mathbf{q}} - \eta)}{A^2} + \frac{\sin^2(\varphi_{\mathbf{q}} - \eta)}{B^2} \right)^{1/2}, \tag{4.27}$$

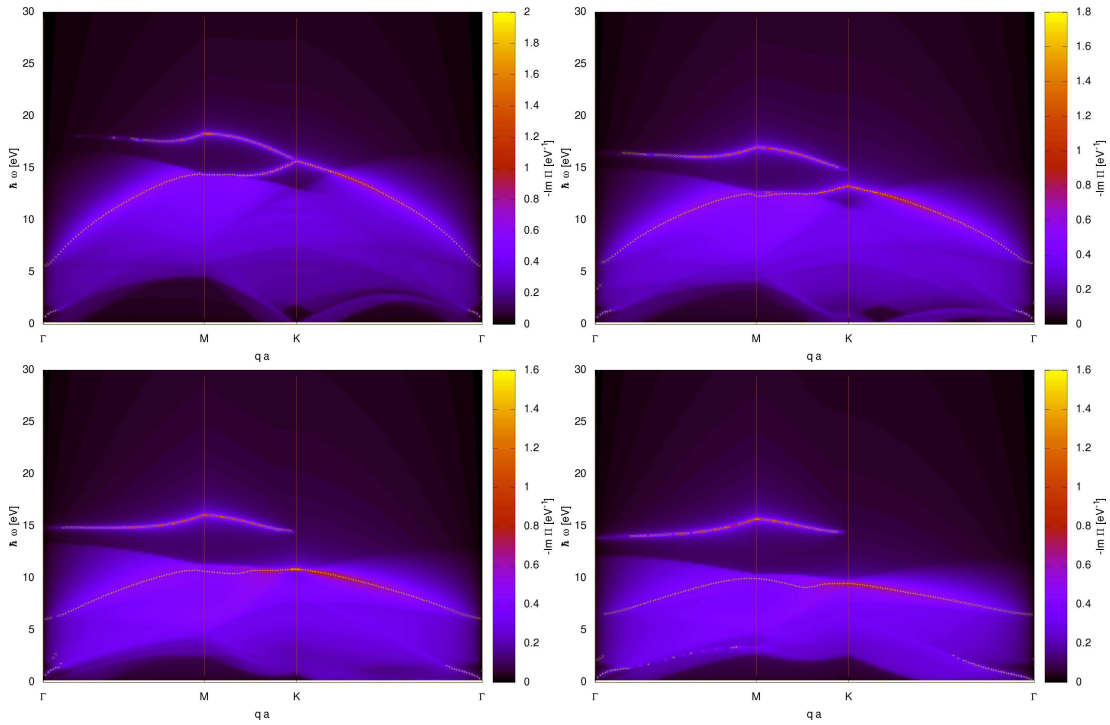

Figure 4.5: Plasmon dispersion relation for suspended doped graphene ($\mu = 1$ eV, $\epsilon_{r1} = \epsilon_{r2} = 1$), including LFE and z-extension, with strain applied along the $\theta = \pi/6$ (zig-zag) direction. Strain increases (from left to right, from top to bottom) as $\varepsilon = 0,\ 0.075,\ 0.175,\ 0.275$.

where A and B denote the semiaxes of the constant energy ellipse, which have been defined in Eqs. (3.23), whereas the angle η is a function of the hopping parameters which has been defined in Eqs. (3.24). It follows that $\tilde{\omega}_1$ attains its maximum values whenever $\varphi_{\mathbf{q}} - \eta = \pi/2$ (modulo π), and its minimum values whenever $\varphi_{\mathbf{q}} - \eta = 0$ (modulo π). It turns out that $\eta = \theta$ in the zig-zag and armchair cases (cf. Fig. 4.7), whereas $\eta \simeq \theta$ in the generic case.

In the previous Chapter, we have not considered the Drude peak in the optical conductivity. The Drude peak appears in the optical conductivity for $\omega \to 0$ in doped graphene as

$$\sigma(\omega \to 0) = D\delta(\omega), \tag{4.28}$$

where D is called Drude weight. The Drude weight can be connected by means of an effective f-sum rule to the dispersion relation of plasmons [1], which has been studied also under applied strain [114].

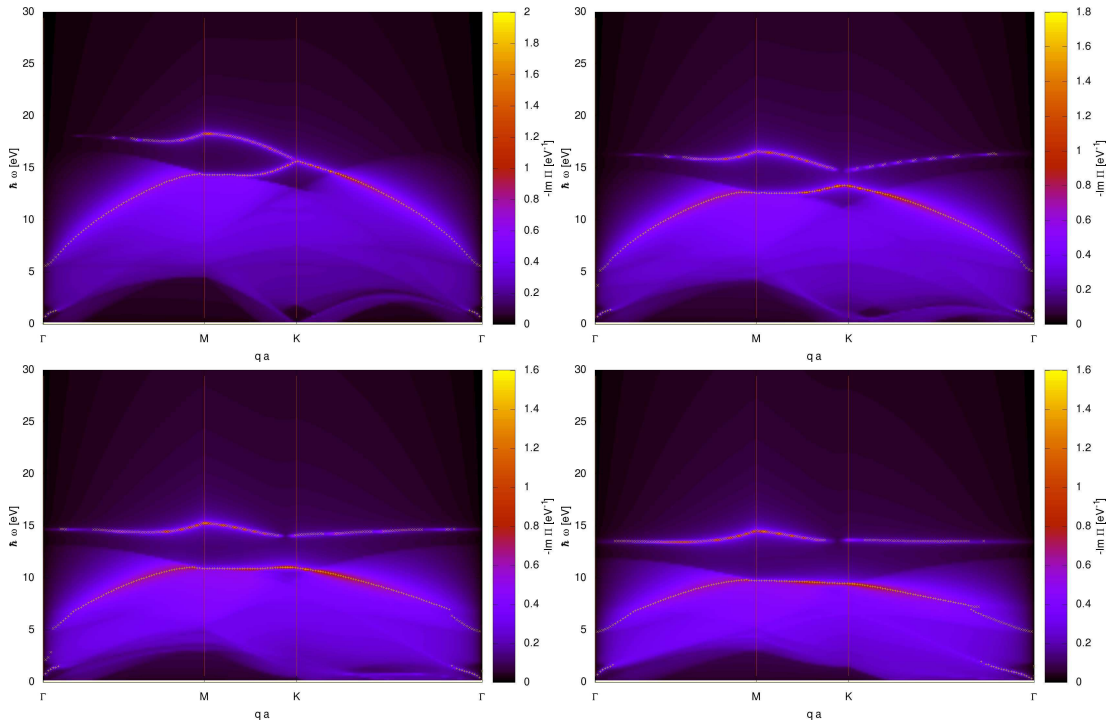

Figure 4.6: Plasmon dispersion relation for suspended doped graphene ($\mu = 1$ eV, $\epsilon_{r1} = \epsilon_{r2} = 1$), including LFE and z-extension, with strain applied along the $\theta = \pi/4$ (generic) direction. Strain increases (from left to right, from top to bottom) as $\varepsilon = 0,\ 0.075,\ 0.175,\ 0.275$.

Through the continuity equation, one obtains

$$\sigma_{\phi\phi}(\omega) = \frac{ie^2}{\omega} \lim_{q\to 0} \frac{\omega^2}{q^2} \Pi_{\rho\rho}(\mathbf{q}, -\mathbf{q}, \omega). \tag{4.29}$$

Letting $\omega \to \omega + i0^+$, and extracting the real part, one recognizes the Drude weight as

$$D_\phi = \pi e^2 \lim_{\omega\to 0} \lim_{q\to 0} \frac{\omega^2}{q^2} \mathrm{Re}\, \Pi_{\rho\rho}(\mathbf{q}, -\mathbf{q}, \omega). \tag{4.30}$$

Using the asymptotic limit of the polarization (4.19), one finds

$$D_\phi = 4\mu\sigma_0 \left[\pi A_{cell}^{-1} \rho_1 \left(\frac{\cos^2(\phi - \eta)}{A^2} + \frac{\sin^2(\phi - \eta)}{B^2} \right) \right], \tag{4.31}$$

where $\sigma_0 = \pi e^2/2h$ is the so-called universal interband electrical conductivity of neutral graphene [101], $A_{cell} = (1 + \varepsilon)(1 - \nu\varepsilon)3\sqrt{3}a^2/2$ is the area of the unit cell, ρ_1 is the strain-dependent prefactor in the linear dependence of the DOS on the chemical potential at low en-

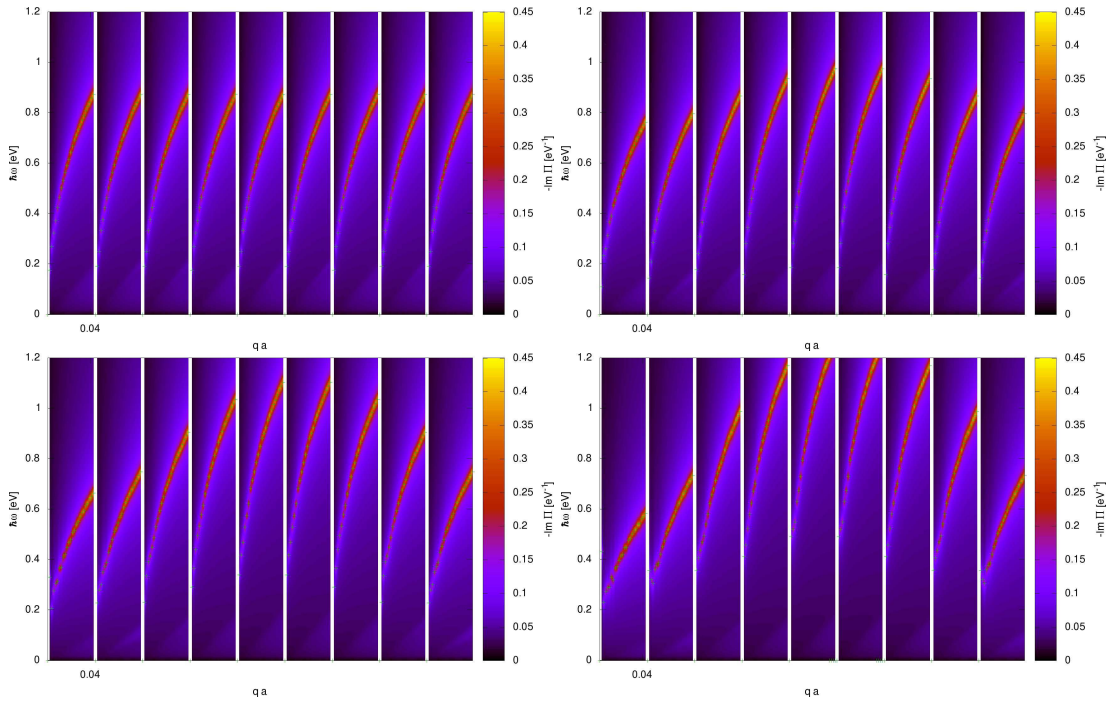

Figure 4.7: Plasmon dispersion relation for suspended doped graphene ($\mu = 1$ eV, $\epsilon_{r1} = \epsilon_{r2} = 1$), with strain applied along the $\theta = 0$ (armchair) direction. Strain increases (from left to right, from top to bottom) as $\varepsilon = 0, 0.075, 0.175, 0.275$. In each graph, different panels refer to $\omega_1(\mathbf{q}) = \omega_1(q, \varphi_{\mathbf{q}})$, with $\varphi_{\mathbf{q}} = 0°, 20°, 40°, \ldots 160°$.

ergy, $\rho(\mu) = \rho_1|\mu|$ [110], and ϕ is the direction of the normally incident monochromatic electric field.

In Eq. (4.31), the quantity between square brackets goes to unity in the limit $\varepsilon \to 0$, where in particular $\rho_1 = 4/(\pi\sqrt{3}t^2)$. From Eq. (4.31), it follows that D_ϕ attains its maximum values whenever $\phi - \eta = \pi/2$ (modulo π), and its minimum values whenever $\phi - \eta = 0$ (modulo π). The ellipse semiaxes A and B depend on strain, whose role is that of increasing the ellipse anisotropy according to Eqs. (3.23). In the unstrained limit, $\varepsilon = 0$, one has $A = B$, hence one recovers that the Drude weight is independent of polarization of incident electromagnetic field. Such a dependence of the Drude weight on applied uniaxial strain is amenable to experimental verification. Finally, the prefactor $\tilde{\omega}_1$ in the long-wavelength dispersion relation of low-energy plasmons in graphene [114], $\omega_{\mathbf{q}} = \tilde{\omega}_1\sqrt{qa}$, is related to the Drude weight through [1]

$$\frac{D_\phi}{(\hbar\tilde{\omega}_1)^2 a} = \frac{2\pi\epsilon_0\epsilon_r}{\hbar}. \tag{4.32}$$

Chapter 5

Electronic linear response functions in strained graphene within the Dirac model

In graphene, the low-energy quasiparticles can be described as massless Dirac fermions, with a cone dispersion relation in reciprocal space around the Dirac points. Such a linear spectrum and reduced dimensionality yield remarkable behaviors already in the non-interacting limit of several electronic properties of graphene. These include, *inter alia*, the reflectivity, the optical conductivity, the plasmon dispersion relation, as well as a newly predicted transverse electromagnetic mode [98]. These properties can be extracted from the study of the appropriate correlation functions within linear response theory [127, 155]. This description, which is called Dirac approximation, allows an analytical study of several electronic properties at low energies and small momenta. At these limits, the corrections due to the z-extension of the electron wave functions are negligible. Hence the electronic system is treated as a two dimensional electron gas.

In this Chapter, we consider the effect of strain on the various electronic properties that may be described by linear response correlation functions within the Dirac model. Usually, the main effect on the low energy electronic properties of the uniaxial strain which has been considered is a strain-induced shift of the position of the Dirac points in reciprocal space [61, 88]. In other terms, the main effect of strain can be described associating an effective gauge field vector potential $\mathbf{A}$ to each Dirac point. These effective vector potentials have opposite signs for graphene's two valleys K and K', which means that elastic deformations, unlike magnetic field,

do not violate the time-reversal symmetry of a crystal as a whole [61].

This description of the interplay of structural and electronic properties has been confirmed experimentaly. Indeed, recent experiments demonstrated the possibility to have Landau levels associated to strain in graphene [61]. Moreover, there are several ideas to exploit strain as a fictitious gauge field. For example, de Juan *et al.* [36] have proposed a device to measure microstresses in graphene based on a scanning-tunneling-microscopy setup, which is able to measure Aharonov-Bohm interferences at the nanometer scale. The interferences to be observed in the local density of states are created by the fictitious magnetic field associated to elastic deformations of the sample.

Here, we explicitly consider not only the strain-induced displacement of the Dirac points in reciprocal space, but also a strain-induced deformation of the Dirac cones, resulting in a strain-dependent anisotropic Fermi velocity. We also show that both effects are of the same order on the applied strain intensity ε.

In this Chapter, we take into account the case of homogeneous strain. In this case, the modifications of the electronic linear response correlation function at low energies are related to the strain-induced deformation of the Dirac cones. On the other hand, the Dirac cone shifts do not induce any change of the linear response correlation functions in homogeneously strained graphene. Hence, here, we deal with an analytical study of the modifications of several low-energy electronic properties of graphene under strain.

5.1 Massless Dirac fermions in strained graphene

In momentum space, the effect of uniaxial strain on the Hamiltonian is likewise accounted for by the strain tensor, Eq. (3.2). The strain tensor can be written in a more compact form as

$$\boldsymbol{\varepsilon} = \frac{1}{2}\varepsilon[(1-\nu)\mathbb{I} + (1+\nu)A(\theta)], \tag{5.1}$$

where

$$A(\theta) = \cos(2\theta)\sigma_z + \sin(2\theta)\sigma_x. \tag{5.2}$$

In Eq. (5.1), θ denotes the angle along which the strain is applied, with respect to the $\hat{x}$ axis in the lattice coordinate system, in accordance with Fig. 3.1, ε is the strain modulus, and ν is Poisson's ratio.

The effect of uniaxial strain in graphene is usually described as a shift in momentum space of the location of the Dirac points. However, starting from the more general, tight-binding Hamiltonian, expanding to first order in the strain modulus, and to second order in the impulses, one may show that applied strain also induces a deformation of the Dirac cones, at the same (first) order in ε. Explicitly, one finds

$$\begin{aligned} H = {} & \hbar v_{\mathrm{F}} \sigma_x \left[\left(1 + \frac{1-2\kappa_0}{2} \varepsilon (1-\nu) + \frac{1-\kappa_0}{2} \varepsilon (1+\nu) \cos(2\theta) \right) p_x + \frac{1-\kappa_0}{2} \varepsilon (1+\nu) \sin(2\theta) p_y \right] \\ & + \hbar v_{\mathrm{F}} \sigma_y \left[\left(1 + \frac{1-2\kappa_0}{2} \varepsilon (1-\nu) - \frac{1-\kappa_0}{2} \varepsilon (1+\nu) \cos(2\theta) \right) p_y + \frac{1-\kappa_0}{2} \varepsilon (1+\nu) \sin(2\theta) p_x \right] \\ & - \hbar v_{\mathrm{F}} \tau_z \sigma_x (\kappa_0 / a) \varepsilon (1+\nu) \sin(2\theta) - \hbar v_{\mathrm{F}} \tau_z \sigma_y (\kappa_0 / a) \varepsilon (1+\nu) \cos(2\theta) \\ & - \frac{1}{4} \hbar v_{\mathrm{F}} \tau_z \left[\sigma_y (p_x^2 - p_y^2) + 2 \sigma_x p_x p_y \right] , \end{aligned} \tag{5.3}$$

where v_{F} is the Fermi velocity in the unstrained graphene, σ_i ($i = x, y, z$) are the Pauli matrices which act on the pseudospin space (A and B), whereas τ_i ($i = x, y, z$) are the Pauli matrices which are associated with the two-dimensional valley space (K and K'). Moreover, $\kappa_0 = (a/2t)|\partial t / \partial a| \approx 1.6$ is related to the logarithmic derivative of the nearest-neighbor hopping t at $\varepsilon = 0$. Eq. (5.3) acts on the four-component spinors which we have just shown in the Eq. (2.50).

Our model is based on the tight-binding approximation for the band structure, including only nearest-neighbor hopping. We have studied in detail the tight-binding approximation for graphene under uniaxial strain in the Chapter 3. To this level of approximation, one does not observe any strain-induced modification of the work function, Φ. This effect is equivalent to a rigid vertical shift of the electronic bands. In order to include also such effects, one also needs to consider next-nearest neighbor hopping [28]. Making use of the expression for the hopping function between two neighboring carbon p-orbitals involved in a π bond, as a function of the

bond length ℓ, $V_{pp\pi}(\ell) = t_0 e^{-3.37(\ell/a-1)}$, with $t_0 = -2.7$ eV [121], one finds

$$\Phi = \frac{3}{2}(1-\nu)\sqrt{3}a \left.\frac{dV_{pp\pi}(\ell)}{d\ell}\right|_{\ell=\sqrt{3}a} \varepsilon \approx 1.7\,\mathrm{eV} \times \varepsilon, \tag{5.4}$$

viz. a scalar term, going linear with the strain modulus ε, whose order of magnitude agrees with the *ab initio* results of Ref. [32]. At any rate, the work function, Eq. (5.4), can be absorbed in an effective scalar potential U, which is diagonal both in the valley space and in the pseudospin space.

The spectrum of the strained Hamiltonian, Eq. (5.3), is still linear, but now around the shifted Dirac points

$$\mathbf{q}_{\mathrm{D}} a = \pm(\kappa_0 \varepsilon(1+\nu)\sin(2\theta), \kappa_0 \varepsilon(1+\nu)\cos(2\theta))^{\top}. \tag{5.5}$$

In particular, setting $\mathbf{q} = \mathbf{p} \mp \mathbf{q}_{\mathrm{D}}$, with $\mathbf{q}$ measuring now the vector displacement from the shifted Dirac point, the Fermi velocity, defined as the slope of the Dirac cone in the direction of $\mathbf{q}$, will now have anisotropic components $c_{\parallel} v_{\mathrm{F}}$, $c_{\perp} v_{\mathrm{F}}$ along the direction of applied strain and the direction orthogonal to it, respectively, with

$$c_{\parallel} = 1 - 2\kappa\varepsilon, \tag{5.6a}$$

$$c_{\perp} = 1 + 2\kappa\nu\varepsilon, \tag{5.6b}$$

where $\kappa = \kappa_0 - \frac{1}{2}$.

Thus, the low-energy Hamiltonian maintains a linear form even in the presence of strain, and can still be written as

$$H = \hbar v_{\mathrm{F}} \tau_0 \boldsymbol{\sigma} \cdot \mathbf{q}', \tag{5.7}$$

where

$$\mathbf{q}' = R(\theta) S(\varepsilon) R(-\theta) \mathbf{q}, \tag{5.8}$$

with $R(\theta)$ the rotation matrix in the direction of applied strain, and $S(\varepsilon) = \mathrm{diag}\,(c_{\parallel}, c_{\perp})$ the matrix describing the deformation of the Dirac cone. Explicitly, for the compound transformation matrix $R(\theta)S(\varepsilon)R(-\theta)$ mapping $\mathbf{q}$ onto $\mathbf{q}'$ one finds

$$R(\theta) S(\varepsilon) R(-\theta) = \mathbb{I} - 2\kappa\boldsymbol{\varepsilon}. \tag{5.9}$$

As is emphasized at length, the effect of applied strain on graphene is two-fold. Within the Dirac approximation, applied strain amounts to adding a term

$$-\hbar v_{\mathrm{F}} \tau_z \boldsymbol{\sigma} \cdot \mathbf{q}_{\mathrm{D}}$$

to the Hamiltonian. We remind that the shifted Dirac point $\mathbf{q}_{\mathrm{D}}$ is proportional to the deformation. Hence, such a term is analogous to a coupling term with a gauge field $\mathbf{A}$, say

$$-\hbar v_{\mathrm{F}} \tau_0 \boldsymbol{\sigma} \cdot \mathbf{A},$$

a part from the fact that τ_z is replaced by the identity τ_0 (*i.e.* there is no time-reversal breaking). Moreover, the second effect of the applied strain induces a variation of the Fermi velocity. In particular, uniaxial strain implies a Fermi velocity anisotropy.

While the first effect, *i.e.* Dirac points shift, dominates at low energies, and is therefore the focus of most previous investigations in this area, the second effect, *i.e.* Fermi velocity anisotropy, is usually neglected. If one takes into account only the first term, it can be adsorbed in a unitary gauge transformation, and should not produce observable effects, unless the vector $\mathbf{q}_{\mathrm{D}}$ is non-irrotational, *i.e.* $\nabla \times \mathbf{q}_{\mathrm{D}} \neq 0$, as is the case considered by Guinea, Katsnelson and Geim [61]. In the case of homogeneous strain, we are in the rotational case $\nabla \times \mathbf{q}_{\mathrm{D}} = 0$, where no effect should be observable *per se*, it is a strain-induced modification of the velocity, which is the only source of the effects on the linear response correlation functions.

A central result of this Chapter is that a correspondence holds between a generic linear response function $\chi(\mathbf{q}, \omega)$ under applied strain, with respect to its unstrained limit, $\chi^{(0)}(\mathbf{q}, \omega)$ [115]. This follows from the fact that any linear response function $\chi(\mathbf{q}, \omega)$ of a noninteracting electron system can be expressed as an integral over the first Brillouin zone (1BZ) of a suitable matrix operator over pseudospins, which is itself a function of $\mathbf{q}$. Such an operator then admits a unique expression in terms of the Pauli matrices σ_x, σ_y, σ_z, and the identity matrix σ_0. The simplest cases are then given by the density operator and the current density operator, which,

for the unstrained case, in reciprocal space read

$$\rho^{(0)}(\mathbf{q}) = \sum_{\mathbf{k}} \Psi^{\dagger}_{\mathbf{k}-\mathbf{q}} \sigma_0 \Psi_{\mathbf{k}}, \tag{5.10a}$$

$$J^{(0)}_i(\mathbf{q}) = -ev_{\mathrm{F}} \sum_{\mathbf{k}} \Psi^{\dagger}_{\mathbf{k}-\mathbf{q}} \sigma_i \Psi_{\mathbf{k}}, \quad i = x, y, \tag{5.10b}$$

respectively, where $\Psi^{\dagger}_{\mathbf{q}} = (\psi_{\mathbf{q}A}, \psi_{\mathbf{q}B})$, and $\psi_{\mathbf{q}\alpha}$ destroys a quasiparticle with momentum $\mathbf{q}$ and pseudospin $\alpha = A, B$, and summations run over the 1BZ. While the density operator does not change under applied strain, for the generic component of the current density operator one has

$$J_i = [\mathbb{I} - 2\kappa\boldsymbol{\varepsilon}]_{ij} J^{(0)}_j. \tag{5.11}$$

Here and below a summation will be understood over repeated indices ($j = x, y$). Both operators are diagonal in valley space, hence here we can neglect this quantity because its only effect is a degeneracy analogously to the spin.

Defining now eigenvalues and eigenvectors in pseudospin space of the Hamiltonian with and without applied strain, Eqs. (2.49) and (5.7), as $H^{(0)}|\mathbf{q}', \lambda\rangle^{(0)} = E^{(0)}_{\lambda\mathbf{q}'}|\mathbf{q}', \lambda\rangle^{(0)}$ and $H|\mathbf{q}, \lambda\rangle = E_{\lambda\mathbf{q}}|\mathbf{q}, \lambda\rangle$, respectively, with λ a band index, it follows that both $E_{\lambda\mathbf{q}}$ and $|\mathbf{q}, \lambda\rangle$ under applied strain are mapped onto $E^{(0)}_{\lambda\mathbf{q}'}$ and $|\mathbf{q}', \lambda\rangle^{(0)}$, respectively, where $\mathbf{q}'$ is given in terms of $\mathbf{q}$ by Eq. (5.8). Performing such a linear change of variables in the integral defining the correlation function of interest, in the cases of the density-density and current-current correlation function, it follows therefore that

$$\Pi_{\rho\rho}(\mathbf{q}, \omega) = [\det S(\varepsilon)]^{-1} \, \Pi^{(0)}_{\rho\rho}(\mathbf{q}', \omega), \tag{5.12a}$$

$$\Pi_{ij}(\mathbf{q}, \omega) = [\det S(\varepsilon)]^{-1} \, [\mathbb{I} - 2\kappa\boldsymbol{\varepsilon}]_{ih} \Pi^{(0)}_{hk}(\mathbf{q}', \omega) [\mathbb{I} - 2\kappa\boldsymbol{\varepsilon}]_{kj}, \tag{5.12b}$$

where $\det S(\varepsilon) = (1 - 2\kappa\varepsilon)(1 + 2\kappa\nu\varepsilon)$. From Eq. (5.12a), in the case of the density-density correlation function, it follows in particular that the effect of applied strain is that of transforming the momentum variable $\mathbf{q}$ into an 'effective' one $\mathbf{q}'$, plus the introduction of an overall scale factor $[\det S(\varepsilon)]^{-1}$, which is isotropic with respect with the strain direction. Such a scale factor is directly related to the slope of the electronic density of states at the Fermi level. As

is well known, this goes linearly with the chemical potential μ, and it has been shown that its steepness increases with increasing strain, for moderately low strain modulus [110]. In the case of the current-current correlation function, such an overall effect is then superimposed to an anisotropic deformation, depending on the angle of applied strain, θ, as shown by Eq. (5.12b).

Linearizing Eq. (5.12) with respect to ε, one finds

$$\Pi_{\rho\rho}(\mathbf{q},\omega) = [1+2\kappa(1-\nu)\varepsilon]\,\Pi^{(0)}_{\rho\rho}(\mathbf{q},\omega) - 2\kappa\frac{\partial\Pi^{(0)}_{\rho\rho}(\mathbf{q},\omega)}{\partial q_h}\varepsilon_{hk}q_k, \tag{5.13a}$$

$$\Pi_{ij}(\mathbf{q},\omega) = [1+2\kappa(1-\nu)\varepsilon]\,\Pi^{(0)}_{ij}(\mathbf{q},\omega) - 2\kappa\frac{\partial\Pi^{(0)}_{ij}(\mathbf{q},\omega)}{\partial q_h}\varepsilon_{hk}q_k - 2\kappa\{\boldsymbol{\varepsilon},\boldsymbol{\Pi}^{(0)}(\mathbf{q},\omega)\}_{ij}, \tag{5.13b}$$

where the curly brackets in the last term denote a matrix anticommutator.

5.1.1 Density-density correlation function

We now specifically turn to consider the density-density correlation function within linear response theory, *i.e.* the electron polarization $\Pi_{\rho\rho}(\mathbf{q},\omega)$. Plasmon modes are then recovered as poles of the polarization, and the effect of strain on their dispersion relation has been studied in Chapter 4.

In given limits, the asymptotic form of the noninteracting polarization in the absence of strain, say $\Pi^{(0)}_{\rho\rho}(\mathbf{q},\omega)$ is known explicitly. For instance, in the long wavelength limit ($\hbar v_{\mathrm{F}} q/\mu \to 0$), one finds [155]

$$\Pi^{(0)}_{\rho\rho}(q\to 0,\omega) = \frac{g_s g_v q^2}{8\pi\hbar\omega}\left[\frac{2\mu}{\hbar\omega} + \frac{1}{2}\log\left|\frac{2\mu-\hbar\omega}{2\mu+\hbar\omega}\right| - i\frac{\pi}{2}\Theta(\hbar\omega-2\mu)\right], \tag{5.14}$$

where $g_s = g_v = 2$ take into account for spin and valley degeneracies, respectively. In other words, $\Pi^{(0)}_{\rho\rho}(q\to 0,\omega) = Z(\omega)q^2$, at a given ω, with the complex factor $Z(\omega)$ implicitly defined by Eq. (5.14).

Longitudinal collective excitation and plasmarons

In the case of applied strain, but still in the noninteracting limit, this is then readily modified through the linearized Eq. (5.13), yielding

$$\Pi_{\rho\rho}(q \to 0, \omega) = [1 - 2\kappa(1+\nu)\varepsilon\cos(2\theta - 2\phi)]\, Z(\omega) q^2, \tag{5.15}$$

where $\mathbf{q} \equiv q(\cos\phi, \sin\phi)$. Within the random phase approximation (RPA), the interacting polarization reads $\bar{\Pi}_{\rho\rho}(\mathbf{q}, \omega) = \Pi_{\rho\rho}(\mathbf{q}, \omega)/(1 - V(q)\Pi_{\rho\rho}(\mathbf{q}, \omega))$, where $V(q) = e^2/(2\epsilon_r\epsilon_0 q)$ is the (bare) Coulombic electron-electron interaction, and ϵ_r is the dielectric constant of the medium. Here, we use the two dimensional Coulombic potential because in the limit $\hbar v_{\rm F} q/\mu \ll 1$ we can neglect the z-extension of the electron wave functions, since $q/\kappa_z \ll 1$. Moreover, we remind that κ_z is reciprocal to the decay length along z-direction, which has been defined in Eq. (4.16). Solving for the plasmon dispersion relation, $\mathrm{Re}\,\bar{\Pi}^{-1}_{\rho\rho}(\mathbf{q}, \omega) = 0$, at low energies one finds

$$\begin{aligned} \hbar\omega_{\rm pl} &= \sqrt{\frac{e^2}{2\pi\epsilon}\mu}\,[1 - \kappa(1+\nu)\varepsilon\cos(2\theta - 2\phi)]\,\sqrt{q} \\ &\equiv \hbar\tilde{\omega}_1(\phi)\sqrt{qa}. \end{aligned} \tag{5.16}$$

One thus finds that the prefactor $\tilde{\omega}_1(\phi)$ in the $\sqrt{q}$-dependence is maximum [resp., minimum] for $\phi - \theta = \pi/2$ [$\phi - \theta = 0$], *i.e.* wavevector orthogonal [parallel] to the direction of applied strain. Correspondingly, one also finds for the imaginary part of the retarded polarizability along the low-energy plasmon branch

$$\mathrm{Im}\,\bar{\Pi}_{\rho\rho}(\mathbf{q}, \omega + i0^+) = -\frac{1}{2}\sqrt{\frac{2\pi\epsilon}{e^2}\mu}\,[1 - \kappa(1+\nu)\varepsilon\cos(2\theta - 2\phi)]\,(qa)^{3/2}\delta(\hbar\omega - \hbar\omega_{\rm pl}(\mathbf{q})). \tag{5.17}$$

Therefore, one recovers a dependence of the plasmon spectral weight on the angle of applied strain, similar to that shown by $\tilde{\omega}_1(\phi)$ in Eq. (5.16). These results are in agreement with the analogous analysis shown in Chapter 4. Moreover, one can note that the angle η, defined in Eq.(3.24), which characterizes the anisotropy of low energy plasmon, coincides with the stress direction θ at first order in ε and at zeroth order in energy.

The composite elementary excitations arising from the coupling of charge carriers and plasmons, the so-called plasmarons, have been considered in a general context earlier on by Lundqvist [90, 91]. Recently, plasmarons have been experimentally observed in graphene by means of angular resolved photoemission spectroscopy (ARPES) [21], and their dispersion relation described theoretically within the G_0W-RPA approximation [126].

In n doped graphene, a plasmaron mode with momentum $\mathbf{k}$ results from the relatively strong coupling of a quasihole with momentum $\mathbf{k}+\mathbf{q}$, and a plasmon with momentum $-\mathbf{q}$, the quasihole-plasmon coupling being stronger when the two excitations have the same group velocity [126]. At $\mathbf{k}=0$, the plasmaron relative momentum modulus turns out to be

$$q = \frac{e^2}{8\pi\epsilon}\frac{\mu}{(\hbar v_{\mathrm{F}})^2}, \tag{5.18}$$

where μ is the chemical potential. Therefore, the plasmaron binding energy with respect to the Fermi energy can be estimated, in first approximation, as the sum of the energies of the bare quasihole and plasmon, both having momentum modulus q, *viz.*

$$E_P = -\mu - \alpha\frac{c}{v_{\mathrm{F}}}\frac{\mu}{2\epsilon_r}, \tag{5.19}$$

where α is the fine structure constant. In the realistic case of graphene on a SiO_2 substrate, Eq. (5.19) yields $E_P \simeq -1.25\mu$. A more accurate estimate, including the contribution of the quasihole-plasmon interaction at the G_0W-RPA level [126], yields $E_P \simeq -1.3\mu$, in better agreement with the experimental results [21]. In this Chapter we have seen that the uniaxial strain on the graphene sheet induces a modification of the electronic bands and of the plasmonic spectrum. Therefore, it can be expected that strain also affects the energy dispersion of the plasmaronic modes.

In particular, the quasiparticle dispersion relation, to linear order in ε, reads

$$\epsilon_{\mathbf{q}} = \pm\hbar v_{\mathrm{F}} q[(1-\kappa(1-\nu)\varepsilon) - \kappa(1+\nu)\varepsilon\cos(2\theta+2\phi)], \tag{5.20}$$

where the $+$ $(-)$ sign refers to the conduction (valence) band, and where the plasmon dispersion relation under strain is expressed by Eq. (5.16). Deriving the corresponding group velocities

from the above Eqs. (5.20) and (5.16), Eqs. (5.18) and (5.19) for the plasmaron momentum and energy, respectively, get modified into

$$q = [1 + 2\kappa(1-\nu)\varepsilon]\frac{e^2}{8\pi\epsilon}\frac{\mu}{(\hbar v_{\rm F})^2}, \tag{5.21a}$$

$$E_P(\phi) = -\mu - \alpha\frac{c}{v_{\rm F}}\frac{\mu}{2\epsilon_r}[1 + \kappa(1-\nu)\varepsilon - \kappa(1+\nu)\varepsilon\cos(2\theta - 2\phi)], \tag{5.21b}$$

to linear order in the strain modulus ε. Eq. (5.21b) shows that, in the presence of applied uniaxial strain, the plasmaronic energy at $\mathbf{k} = 0$ acquires an explicit dependence on the angle ϕ of the quasihole momentum $\mathbf{q}$. This is due to the anisotropy of both the electronic and the plasmon spectrum. Correspondingly, the plasmaron energy is characterized by a central value

$$E_P^{\rm c} = -\mu - \alpha\frac{c}{v_{\rm F}}\frac{\mu}{2\epsilon_r}[1 + \kappa(1-\nu)\varepsilon], \tag{5.22}$$

and a strain-induced energy width

$$\Delta E_P = \alpha\frac{c}{v_F}\frac{\mu}{\epsilon_r}\kappa(1+\nu)\varepsilon. \tag{5.23}$$

Considering again the realistic case of graphene on a SiO_2 substrate, one can estimate the central plasmaron energy in the unstrained case as $E_P^{\rm c}(\varepsilon = 0) = -1.25\mu = -125$ meV, for $\mu = 100$ meV, with zero energy width. Correspondingly, in the case of an applied strain $\varepsilon = 10$ %, one finds a central plasmaron energy of $E_P^{\rm c}(\varepsilon = 10\ \%) = -127.4$ meV, with an energy width $\Delta E_P(\varepsilon = 10\ \%) = 6.27$ meV. Hence, the effect of applied uniaxial strain on graphene is therefore that of shifting and broadening the plasmaron energy, proportionally to the strain modulus [119]. Therefore, by suitably applying uniaxial strain, one gains further control on the energy of the plasmaronic excitation, besides the possibility of tuning the relative dielectric constant ϵ_r [152].

Optical conductivity and the transverse collective excitation

Another quantity of interest which is related to the density-density correlation function is the optical conductivity, which can be obtained as

$$\sigma_{\phi\phi}(\omega) = \frac{ie^2}{\omega} \lim_{q\to 0} \frac{\omega^2}{q^2} \Pi_{\rho\rho}(\mathbf{q}, \omega). \tag{5.24}$$

Making use of Eqs. (5.13) and (5.14) one therefore finds the optical conductivity in the presence of applied strain as

$$\sigma_{\phi\phi}(\omega) = \sigma_0 \left[1 - 2\kappa(1+\nu)\varepsilon \cos(2\theta - 2\phi)\right] \left(\Theta(\hbar\omega - 2\mu) + i\frac{4}{\pi}\frac{\mu}{\hbar\omega} + \frac{i}{\pi} \log\left|\frac{2\mu - \hbar\omega}{2\mu + \hbar\omega}\right| \right), \tag{5.25}$$

where $\sigma_0 = \pi e^2/2h$ is proportional to the quantum of conductivity. In the hydrostatic limit, $\nu = -1$, $\sigma_{\phi\phi}$ does not depend on strain, as may be expected, as the unstrained relation does not contain the Fermi velocity. The expression of optical conductivity in Eq. (5.25) has the form typical for a rhombic two dimensional lattice, which is expressed in Eq. (3.52). If the stress is applied along one special direction (armchair or zig zag) the lattice becomes rhombic, hence the optical conductivity has the angular dependence expressed in Eq. (5.25) also at high energies ($|E/t| \gtrsim 1$, where t is the characteristic energy, *i.e.* the hopping parameter). On the other hand, if the stress is applied along a generic direction, the angular dependence of the optical conductivity in Eq. (5.25) is valid only at low energies. Indeed, in general the angular dependence of the optical conductivity is more complicated, and its form is expressed in Eq. (3.53).

The above expression for the conductivity, Eq. (5.25), can be exploited to study the strain dependence of the transverse electromagnetic mode, that has been recently predicted theoretically in graphene [98], and in a graphene bilayer [73] . In a 2D electron gas, the spectrum of self-consistent electromagnetic modes obeys the equations

$$1 + i\frac{\sigma}{2\epsilon_0\omega}\zeta(q,\omega) = 0, \tag{5.26a}$$

$$1 - i\frac{\sigma}{2\epsilon_0}\frac{\omega}{\zeta(q,\omega)c^2} = 0, \tag{5.26b}$$

for the longitudinal and transverse collective excitations, respectively, where $\zeta^2(q,\omega) = q^2 - (\omega/c)^2$, where c is the velocity of light in vacuum. In Eqs. (5.26) we take into account the case of suspended graphene, hence the dielectric constant is unitary ($\epsilon_r = 1$). Also here, we do not consider any correction due to z-extension of the electron wave functions since $\zeta/\kappa_z \ll 1$.

While conventional 2D electron systems cannot sustain a transverse electromagnetic mode, it has been predicted [98] that graphene can develop a transverse collective mode, as a consequence of a negative imaginary part in the interband contribution to its optical conductivity, Eq. (5.25). Its logarithmic divergence as $\hbar\omega/\mu \to 2$ is in turn related to the discontinuous behavior of the interband absorption of radiation at frequencies $\hbar\omega > 2\mu$. Such a feature is a generic consequence of causality, and is related through a Kramers-Krönig transformation to the step-like behaviour of the real part of the optical conductivity. This is in turn due to the existence of a Fermi surface, which is however expected to be smeared at finite temperature, thus implying the reduction of the logarithmic singularity into a pronounced (but finite) peak.

Observing Eqs. (5.26) one can state that both collective excitations are not damped only if the real part of the optical conductivity is zero. In order to fulfill this condition, the graphene sample must be doped. Hence the energy range, where both collective excitations are not damped, is $[0; 2\mu[$. Moreover, from Eqs. (5.26), one can observe that the solution for the longitudinal collective excitation (plasmon) is possible only if the imaginary part of the optical conductivity is positive, whereas the solution for the transverse collective excitation is possible only if the imaginary part of the optical conductivity is negative. Hence, these two kinds of collective excitations can exist in two different energy ranges. In other words, at a certain energy a doped graphene sample cannot sustain at the same time both collective excitations.

Making use of Eq. (5.25) in Eq. (5.26a), one consistently recovers Eq. (5.16) for the low energy plasmons. On the other hand, substituting Eq. (5.25) in Eq. (5.26b), one obtains the strain-dependence of the dispersion relation of the transverse electromagnetic mode implicitly as

$$\frac{\hbar c}{\alpha\mu}\zeta(q,\omega) = (1 - 2\kappa(1+\nu)\varepsilon\cos(2\theta - 2\phi)) \left[\frac{\hbar\omega}{2\mu}\log\left|\frac{2\mu + \hbar\omega}{2\mu - \hbar\omega}\right| - 2\right], \tag{5.27}$$

where $\alpha = e^2/(4\pi\epsilon_0\hbar c)$ is the fine structure constant.

Because of the small factor α in the left-hand side of Eq. (5.27), the dispersion relation

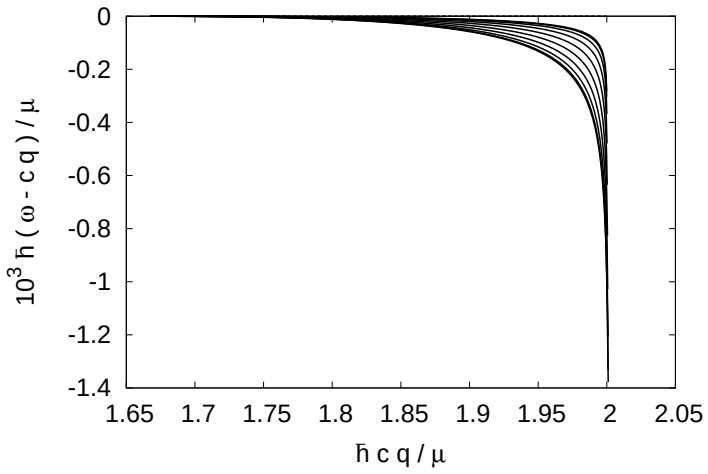

Figure 5.1: Showing deviations from linearity of the frequency of the transverse plasmon, Eq. (5.27), as a function of q modulus, for strain modulus $\varepsilon = 0.1$, and strain direction ranging from $\phi - \theta = 0$ (top) to $\phi - \theta = \pi/2$ (bottom).

of such a transverse mode is close to the linear dispersion relation of the electromagnetic radiation itself, $\omega - cq \lesssim 0$. However, one may expect that applied strain enhances deviations from linearity (*i.e.*, from the photon's dispersion relation), as a consequence of a strain-induced modification of the band dispersion. Fig. 5.1 shows indeed deviations from linearity, $\omega - cq$ of the transverse collective excitation, for q in the allowed range, for strain modulus $\varepsilon = 0.1$, and strain direction $0 \leq \phi - \theta \leq \pi/2$. One finds indeed that, in the case of applied strain, deviations of the transverse mode dispersion relation from that of the photon become significant over a sufficiently wide window in $\hbar cq/\mu \lesssim 2$, especially when $\phi - \theta = \pi/2$.

Therefore, applied strain should help the experimental detection of this elusive collective mode. Indeed, the fact that the transverse mode dispersion relation is close to the corresponding light dispersion implies that such a transverse collective excitation would have a marked photonic character, and a small linewidth would therefore hinder its observation [74]. On the other hand, at finite temperature, the real part of the optical conductivity is nonzero also for $\hbar\omega \lesssim 2\mu$, so that the transverse mode does acquire a finite, albeit small, linewidth [98]. In particular, this applies to energies such that $0 < 2\mu - \hbar\omega < k_{\mathrm{B}}T$. This is exactly where the transverse mode dispersion relation deviates most from its photonic counterpart, the deviation being enhanced, and shifted away from the limiting case $\hbar\omega = 2\mu$, in the case of applied strain, for $\mathbf{q}$ perpendic-

ular to the strain direction. Finally, one therefore expects wavevectors of the order of $\hbar c q \lesssim 2\mu$, or equivalently $q/k_{\rm F} \lesssim 2v_{\rm F}/c \ll 1$, so that it is justified to employ Eq. (5.27) [98, 155].

5.1.2 Current-current correlation functions

In the case of an applied vector field (*e.g.*, an electric field $\mathcal{E}_i$), one may in general decompose the linear response function in a longitudinal and a transverse component as

$$\chi_{ij}(\mathbf{q},\omega) = \frac{q_i q_j}{q^2}\chi_{\parallel}(q,\omega) + \left(\delta_{ij} - \frac{q_i q_j}{q^2}\right)\chi_{\perp}(q,\omega), \tag{5.28}$$

where $q = |\mathbf{q}|$, for a homogeneous system [54]. In particular, in the case of the current-current correlation function, the latter being proportional to the pseudospin-pseudospin counterpart, this can be further simplified as

$$\Pi^{(0)}_{ij}(\mathbf{q},\omega) = \Pi^{(0)}_{+}(q,\omega)\delta_{ij} + \Pi^{(0)}_{-}(q,\omega)A_{ij}(\phi), \tag{5.29}$$

where

$$\Pi^{(0)}_{\pm}(q,\omega) = \frac{1}{2}[\Pi^{(0)}_{\parallel}(q,\omega) \pm \Pi^{(0)}_{\perp}(q,\omega)]. \tag{5.30}$$

Making use of Eq. (5.13b), one finds

$$\begin{aligned}\Pi_{ij}(\mathbf{q},\omega) \;=\; & \Pi^{(0)}_{ij}(\mathbf{q},\omega) - 2\varepsilon\kappa(1+\nu)\Big[\Pi^{(0)}_{-}(q,\omega)\cos(2\theta-2\phi)\delta_{ij} + \\ & + \Pi^{(0)}_{+}(q,\omega)A_{ij}(\theta) + \Pi^{(0)}_{-}(q,\omega)A_{ij}(\phi+\pi/4)\sin(2\theta-2\phi)\Big] + \\ & -\kappa[(1-\nu)+(1+\nu)\cos(2\theta-2\phi)]\varepsilon\left[q\frac{\partial\Pi^{(0)}_{+}(q,\omega)}{\partial q}\delta_{ij} + q\frac{\partial\Pi^{(0)}_{-}(q,\omega)}{\partial q}A_{ij}(\phi)\right].\end{aligned} \tag{5.31}$$

In the static limit ($\omega = 0$), Eq. (5.31) can be further simplified, by considering the analytic result of Ref. [127], with $\Pi^{(0)}_{\parallel}(\mathbf{q},0) = 0$, and

$$\Pi^{(0)}_{\perp}(\mathbf{q},0) = \frac{g_s g_v e^2 v_{\rm F}}{16\hbar q}\Theta(1-x)\left\{1 - \frac{2}{\pi}\left[\arcsin(x) - x\sqrt{1-x^2}\right]\right\}, \tag{5.32}$$

where $x = 2\mu/\hbar v_{\rm F} q$. In particular, one recovers a vanishing response, $\Pi_{\mathbf{qq}}(\mathbf{q},0) = 0$, with

$\Pi_{\mathbf{qq}}$ denoting the current-current correlation function for both vector potential and response field aligned with $\mathbf{q}$, when $\mathbf{q}$ is aligned with the applied field also in the presence of strain, as expected in the static limit. Indeed, the static $\omega \to 0$ longitudinal response describes the response of the system to a static longitudinal vector potential, which can always be removed via a gauge transformation. Therefore, such a contribution to the linear response must be zero.

5.2 Electric and magnetic susceptibilities

The results obtained in the previous paragraph allow to derive several measurable quantities. In particular, in this paragraph we consider the magnetic and electric susceptibilities.

First of all, we study the response of strained graphene to a static and homogeneous magnetic field, which is normal to the graphene plane. A magnetic field applied in the direction perpendicular to the graphene plane can be described as $\mathbf{B}_{ext}(\mathbf{q}) = B_{ext}(\mathbf{q})\hat{\mathbf{z}} = i\mathbf{q} \times \mathbf{A}$, where $\mathbf{A} = i(q_y, -q_x)B_{ext}/q^2$, in reciprocal space. The linear response to such a magnetic field is then given by a current J_i, which in turn produces a magnetization term $\delta\mathbf{B} \equiv \chi_m \mathbf{B}_{ext}$.

In the case of a static, uniform magnetic field, oriented in the direction orthogonal to the graphene sheet, one is interested in the magnetic susceptibility defined as

$$\chi_M = \lim_{q\to 0} \int \frac{d\phi}{2\pi} \chi_m(\mathbf{q}, 0). \tag{5.33}$$

Making use of Eq. (5.32), one obtains

$$\chi_M = \lim_{q\to 0} \left(-\frac{\mu_0}{q^2}\right) \left[1 - \kappa(1-\nu)\varepsilon q \frac{\partial}{\partial q}\right] \Pi^{\perp(0)}(q, 0). \tag{5.34}$$

In the strained case, this reads

$$\chi_M = -\mu_0[1 - 2\kappa(1-\nu)\varepsilon] \frac{g_s g_v e^2 v_F^2}{6\pi} \delta(\mu). \tag{5.35}$$

One therefore obtains a qualitatively similar result to the case of undeformed graphene, treated within the Dirac approximation and neglecting the electron-electron interaction [95, 127]. On the other hand, applied strain causes a reduction of the magnetic response, Eq. (5.34). Although Eq. (5.35) would imply no response to a static, uniform magnetic field away from half-filling,

one expects that finite-temperature effects would broaden the δ-function, already in the noninteracting limit. A qualitatively similar smearing of the peak in the dependence on the chemical potential may also be induced by disorder [79]. Still at zero temperature and in the noninteracting limit, one recovers a nonzero magnetic response also away from half-filling, when the honeycomb lattice structure is considered [56]. The effect of the interactions has been considered in Ref. [127], where it is shown that an interacting 2D Dirac electron liquid develops a magnetic response also at finite doping.

An analogous procedure may be followed to derive the electric susceptibility χ_e, entering the relationship $\delta\mathbf{E} = \chi_e \mathbf{E}_{ext}$ between the electric polarization and an external electric field, which is oriented along the graphene plane. One is then interested in the static ($\omega = 0$) limit of the density-density polarization. In the presence of applied strain, at arbitrary chemical potential μ, using Eq. (5.13), one explicitly finds

$$\begin{aligned}\Pi_{\rho\rho}(q,\omega=0) &= [1+2\kappa(1-\nu)\varepsilon]\left[-\frac{g_s g_v \mu}{2\pi\hbar^2 v_{\rm F}^2}+\frac{g_s g_v q}{8\pi\hbar v_{\rm F}}G_<^+(x)\,\Theta(1-x)\right] \\ &\quad -\kappa[(1-\nu)+(1+\nu)\cos(2\theta-2\phi)]\varepsilon\frac{g_s g_v q}{8\pi\hbar v_{\rm F}}G_<^-(x)\,\Theta(1-x),\end{aligned} \tag{5.36}$$

where $x = 2\mu/\hbar v_{\rm F} q$ and [137, 155]

$$G_<^{\pm}(x) = \pm x\sqrt{1-x^2} - \arccos x, \quad |x|<1. \tag{5.37}$$

In particular, at zero doping ($\mu = 0$, $G_<^{\pm}(0) = -\pi/2$), one finds in general that

$$\chi_e(\mathbf{q},0) = V(q)\Pi_{\rho\rho}(q,0). \tag{5.38}$$

It should be emphasized that, while Eq. (5.38) describes the response of the system to a static electric field lying in the same graphene layer. More explicitly, in the undoped case, Eq. (5.38) reads

$$\begin{aligned}\chi_e = \lim_{q\to 0}\chi_e(\mathbf{q},0) &= -\frac{g_s g_v e^2}{32\epsilon_0\epsilon_r\hbar v_{\rm F}} \\ &\quad \times\left[1+\kappa(1-\nu)\varepsilon-\kappa(1+\nu)\varepsilon\cos(2\theta-2\phi)\right],\end{aligned} \tag{5.39}$$

where ϕ is the direction of the electric field on the graphene plane, thus showing that uniaxial strain introduces a modulation in the angle of applied strain. Observing Eq. (5.39), one can state that uniaxial strain reduces the susceptibility along the stress direction, whereas it enhances the susceptibility along the direction orthogonal to the stress direction.

Using Eq. (5.39) and considering the case of doped graphene, one obtains that the electric susceptibility in the long wavelength limit ($q < 2k_{\mathrm{F}}$) assumes the typical form for a two-dimensional electron gas

$$\chi_e(\mathbf{q}, 0) = -\frac{q}{q_{\mathrm{TF}}}, \tag{5.40}$$

where q_{TF} is the Thomas-Fermi wavevector [70]. In particular, in the case of a strained graphene monolayer, the Thomas-Fermi wavevector takes the following form

$$q_{\mathrm{TF}} = \frac{e^2}{\pi\epsilon}\frac{\mu}{(\hbar v_{\mathrm{F}})^2}[1 + 2\kappa(1-\nu)\varepsilon]. \tag{5.41}$$

Hence one can observe that is possible to tune the Thomas-Fermi wavevector, and consequently the screening properties, not only by doping, but also by applied strain.

Chapter 6

Ballistic transport in strained graphene

Both the low dimensionality and the high mobility make graphene an attractive material for electronic applications. It is possible to measure impressive values of the mobility both in suspended graphene [16, 17] and in graphene devices on suitable substrates, such as on single crystal hexagonal boron nitride (h-BN) [37]. Moreover, low dimensionality allows to realize a source-graphene-drain configuration where the electronic mean free path is longer than the distance between the source and drain, so that it presents ballistic properties [34]. Exploiting the electric field effect, using nano-gate geometries, it is possible to subject the system to potentials varying on a short length scale [25]. Using these techniques, recently it has been possible to experimentally study transport through *p*-*n* junctions and *p*-*n*-*p* junctions in graphene [102, 150, 157]. In these devices, resistance measurements show distinct oscillations, arising from the Fabry-Pérot interference between the two *p*-*n* interfaces. These effects can be explained in terms of ballistic transport.

In the previous Chapters we have seen how strain can modify the electronic properties of graphene. Moreover, recent interest is directed towards the study and realization of graphene-based electronic devices designed by a suitable tailoring of the electronic structure exploiting not only the electric field effect but also applied strain. Both these techniques would give liberty to modify the transport properties of graphene without adding any source of disorder. Hence, by exploiting strain engineering, as well as the electric field effect, it is possible to realize a new class of ballistic devices [120, 123]. Indeed, a considerable amount of work has been devoted to the study of the transport properties in graphene across strain-induced single and multiple

barriers [29, 50, 116, 118].

In this Chapter, we will study the effect of a strain-induced modulation profile on several transport properties of graphene, such as the angular dependence of the tunneling transmission, the conductivity, and the Fano factor [13]. After considering the cases of a single sharp tunneling barrier, and of a superstructure of several, periodically repeated, such sharp barriers, we will specifically study the case in which both the modulus of applied uniaxial strain, and possibly an applied gate potential, depend continuously on position. Moreover, we will generalize our analysis to embrace the case of a generic *nonuniform* strain, and possibly a scalar potential, profile.

6.1 Transmission across a single strain-barrier

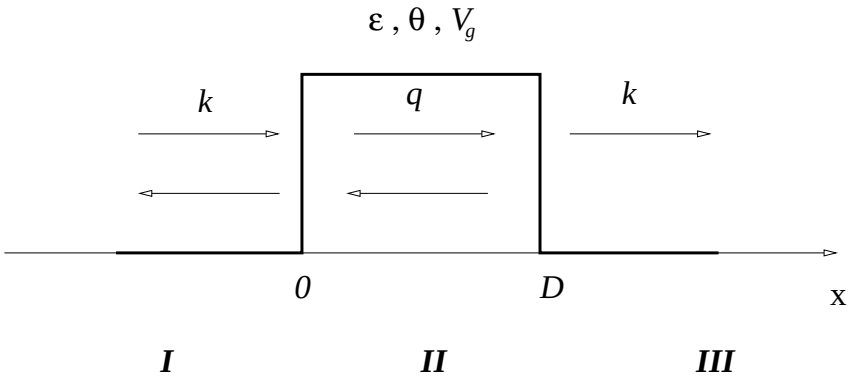

Figure 6.1: One-dimensional single tunneling barrier along the x direction. Region II ($0 \leq x \leq D$) is characterized by applied strain ε along the θ direction, as well as by a gate voltage V_g.

In the whole Chapter we will deal with a one-dimensional uniaxial strain profile, hence we fix the direction θ, along which the tension is applied, with respect to the $\hat{x}$ axis in the lattice coordinate system in Fig. 3.1, whereas the longitudinal deformation ε is generally a function of the position. Hence, it will be convenient to work in the reference frame with the new $\hat{x}$ axis along the direction of applied strain.

In order to describe the electronic properties of graphene under local strain it is useful to remind that the kinetic part of the Hamiltonian for graphene subjected to uniform strain, which

is characterized by ε and θ, has the following form

$$H = \int d\mathbf{r}\Psi^{\dagger}(\mathbf{r})\hbar v_j \left[\tau_0 \mathcal{U}^{\dagger}(\theta)\sigma_j \frac{1}{i}\nabla_j \mathcal{U}(\theta) - \tau_z \mathcal{U}^{\dagger}(\theta)\sigma_j q_{\mathrm{D}j}\mathcal{U}(\theta)\right]\Psi(\mathbf{r}), \tag{6.1}$$

where $\Psi(\mathbf{r}) = (\Psi_{AK}(\mathbf{r}), \Psi_{BK}(\mathbf{r}), \Psi_{BK'}(\mathbf{r}), -\Psi_{AK'}(\mathbf{r}))^{\top}$ is a four-component spinor, $v_j = v_{\mathrm{F}}(1 - \lambda_j\varepsilon)$, v_{F} is the Fermi velocity in unstrained graphene, $\lambda_x = 2\kappa$, $\lambda_y = -2\kappa\nu$, σ_i ($i = x, y, z$) are the Pauli matrices which act on the pseudospin space (A and B), τ_i ($i = x, y, z$) are the Pauli matrices which act on the valley space (K and K'), τ_0 is an identity matrix of order 2 which acts in the two-dimensional valley space, $\mathbf{q}_{\mathrm{D}}$ is the shifted Dirac point with respect to the K point, defined in Eq. (5.5), and the summation over the repeated index $j = x, y$ is understood. The choice of the suitable reference frame with the $\hat{x}$ axis along the direction of applied strain is accomplished by a rotation in the pseudospin space, described by the unitary matrix

$$\mathcal{U}(\theta) = \begin{pmatrix} 1 & 0 \\ 0 & e^{-i\theta} \end{pmatrix}. \tag{6.2}$$

Similarly, the density operator can be expressed as

$$\rho(\mathbf{r}) = \Psi^{\dagger}(\mathbf{r})\Psi(\mathbf{r}), \tag{6.3}$$

and the current density operator as

$$J_i(\mathbf{r}) = -e\Psi^{\dagger}(\mathbf{r})\tau_0 \mathcal{U}^{\dagger}(\theta)v_i\sigma_i\mathcal{U}(\theta)\Psi(\mathbf{r}). \tag{6.4}$$

.

First of all, we consider a graphene device where a central strip of length D is under uniaxial strain, whereas the lateral parts are unstrained and they are semi-infinite. In this model, we have a sharp profile of strain. This approximation holds if the characteristic length a, which describes the linear size over which the strain profile varies appreciably, is much smaller than both the length D and the Fermi wavelength λ_{F} ($\mathsf{a} \ll D, \lambda_{\mathrm{F}}$). Moreover, we will assume that any characteristic length in this model is much larger than the distance a between two nearest neighbor carbon atoms. This last condition allows to neglect any coupling between the valleys K and K'.

Therefore, we consider a strain-induced one-dimensional step-like barrier, characterized by uniaxial strain applied along the direction θ, with strain modulus ε for $0 \leq x \leq D$, and zero otherwise. Correspondingly, the Hamiltonian and current density vector are given by Eqs. (6.1) and (6.4), respectively. In addition, for the sake of generality, we may also consider a nonzero gate potential V_g within the barrier (Fig. 6.1). We remind that a general scalar potential has the following form

$$U = \int d\mathbf{r} U(\mathbf{r})\rho(\mathbf{r}), \tag{6.5}$$

in the case of a sharp barrier we would have $U(\mathbf{r}) = -eV_g\Theta(x)\Theta(D-x)$, where $\Theta(t)$ is the Heaviside (step) function.

Since we are interested in stationary solutions and the strain-barrier is uniform along the y direction, the energy E and the component k_y of the wavevector of an incoming wave are conserved. Actually, in addition to E and k_y, each stationary electronic mode is also labeled by the valley index K or K'. We look therefore for solutions of the stationary Dirac equation of the form

$$\Psi(x,y) = e^{ik_y y}\psi(x) \tag{6.6}$$

where

$$\psi(x) = \begin{cases} \tau_0\mathcal{U}^\dagger(\theta)\psi_{\rm I}(x), & x < 0, \\ e^{i\tau_z q_{{\rm D}x}x}\mathcal{U}^\dagger(\theta)\psi_{\rm II}(x), & 0 \leq x \leq D, \\ \tau_0\mathcal{U}^\dagger(\theta)\psi_{\rm III}(x), & x > D, \end{cases} \tag{6.7}$$

and

$$\psi_{\rm I}(x) = \frac{1}{\sqrt{2}}\begin{pmatrix}1\\ se^{i\varphi}\\ 1\\ se^{i\varphi}\end{pmatrix}e^{ik_x x}+\frac{1}{\sqrt{2}}\begin{pmatrix}r\\ -rse^{-i\varphi}\\ r'\\ -r'se^{-i\varphi}\end{pmatrix}e^{-ik_x x}, \tag{6.8a}$$

$$\psi_{\rm II}(x) = \frac{1}{\sqrt{2}}\begin{pmatrix}ae^{iq_x x}\\ as'e^{i\alpha}e^{iq_x x}\\ a'e^{iq'_x x}\\ a's'e^{i\alpha'}e^{iq'_x x}\end{pmatrix}+\frac{1}{\sqrt{2}}\begin{pmatrix}be^{-iq_x x}\\ -bs'e^{-i\alpha}e^{-iq_x x}\\ b'e^{-iq'_x x}\\ -b's'e^{-i\alpha'}e^{-iq'_x x}\end{pmatrix}, \tag{6.8b}$$

$$\psi_{\rm III}(x) = \begin{pmatrix}t\\ tse^{i\varphi}\\ t'\\ t'se^{i\varphi}\end{pmatrix}e^{ik_x x}. \tag{6.8c}$$

In Eqs. (6.8), φ denotes the angle of incidence with respect to the barrier, $k_x = (|E|/\hbar v_{\rm F})\cos\varphi$, $k_y = (|E|/\hbar v_{\rm F})\sin\varphi$, $(E-U_g)^2 = \hbar^2 v_{\rm F}^2[(1-\lambda_x\varepsilon)^2 q_x^2 + (1-\lambda_y\varepsilon)^2(k_y - q_{{\rm D}y})^2]$, $(E-U_g)^2 = \hbar^2 v_{\rm F}^2[(1-\lambda_x\varepsilon)^2 {q'_x}^2 + (1-\lambda_y\varepsilon)^2(k_y + q_{{\rm D}y})^2]$, $s = \mathrm{sgn}\,(E)$, $s' = \mathrm{sgn}\,(E-U_g)$, with $U_g = -eV_g$. In the four-component spinor in Eq. (6.8) we take into account contemporarily two stationary solutions: both modes have energy E and component k_y of the wavevector, but the first one is related to the valley K whereas the second one is related to the valley K'. The electronic modes, which correspond to the valley K (K'), are propagating waves if q_x (q'_x) is a real value, while they are evanescent if q_x (q'_x) is purely imaginary.

Given the stationary character of the solution, the continuity equation implies that $\nabla\cdot\mathbf{J} = 0$ everywhere. In particular, $\langle\mathbf{J}\rangle \equiv \langle\psi|\mathbf{J}|\psi\rangle$ may only depend on x, therefore $\langle J_x\rangle$ is constant. The latter condition implies, at the barrier boundaries,

$$\psi_{\rm I}(0^-) = (1-\lambda_x\varepsilon)^{-1/2}\psi_{\rm II}(0^+), \tag{6.9a}$$

$$(1-\lambda_x\varepsilon)^{-1/2}\psi_{\rm II}(D^-) = \psi_{\rm III}(D^+). \tag{6.9b}$$

Enforcing the above conditions in Eqs. (6.8), one eventually finds for the tunneling transmission

for a generic mode labeled by E, k_y, K,

$$T = |t|^2 = \frac{C^2 \cos^2\varphi}{C^2 \cos^2\varphi \cos^2(q_x D) + (1 - ss' S \sin\varphi)^2 \sin^2(q_x D)}, \tag{6.10}$$

where $q_y = k_y - q_{\mathrm{D}y}$, $q_x = (1-\lambda_x\varepsilon)^{-1}|(E-U_g)^2/\hbar^2 v_{\mathrm{F}}^2 - (1-\lambda_y\varepsilon)^2 q_y^2|^{1/2}$, $C = (1-\lambda_x\varepsilon)\hbar v_{\mathrm{F}} q_x/|E-U_g|$, $S = (1-\lambda_y\varepsilon)\hbar v_{\mathrm{F}} q_y/|E-U_g|$.

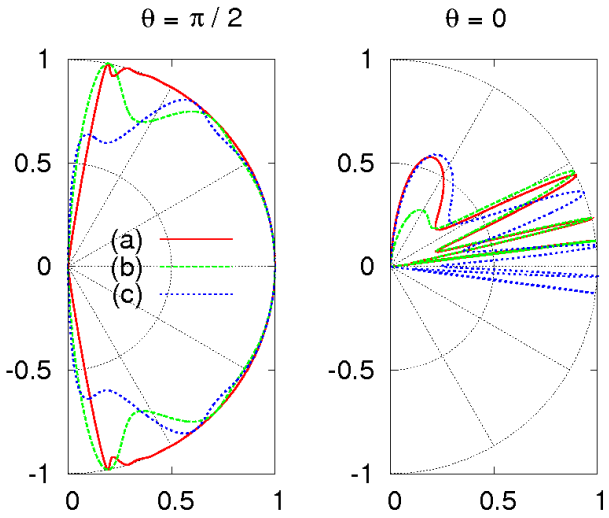

Figure 6.2: Dependence on the incidence angle φ of the tunneling transmission T, Eq. (6.10). Left panel refers to strain applied along the zig-zag direction ($\theta = \pi/2$), and (a) $\varepsilon = 0.03$, $U_g = 0$ meV; (b) $\varepsilon = 0.03$, $U_g = -20$ meV (the strain-induced deformation of the Dirac cone is neglected); (c) $\varepsilon = 0.03$, $U_g = -20$ meV. Right panel refers to strain applied along the armchair direction ($\theta = 0$), and (a) $\varepsilon = 0.01$, $U_g = 0$ meV; (b) $\varepsilon = 0.01$, $U_g = 0$ meV (the strain-induced deformation of the Dirac cone is neglected); (c) $\varepsilon = 0.01$, $U_g = -20$ meV. In any case the electronic modes is labeled with the K valley.

In order to discuss the dependence of the tunneling transmission on the incidence angle φ, we preliminarly observe that propagation within the barrier is allowed whenever

$$\hbar^2 v_{\mathrm{F}}^2 (1-\lambda_y\varepsilon)^2 (k_y - q_{\mathrm{D}y})^2 \leq (E-U_g)^2, \tag{6.11}$$

where $k_y = (E/\hbar v_{\mathrm{F}})\sin\varphi$. Within such a range, one has moreover total transmission ($T = 1$) whenever

$$q_x D = n\pi, \tag{6.12}$$

n being an integer.

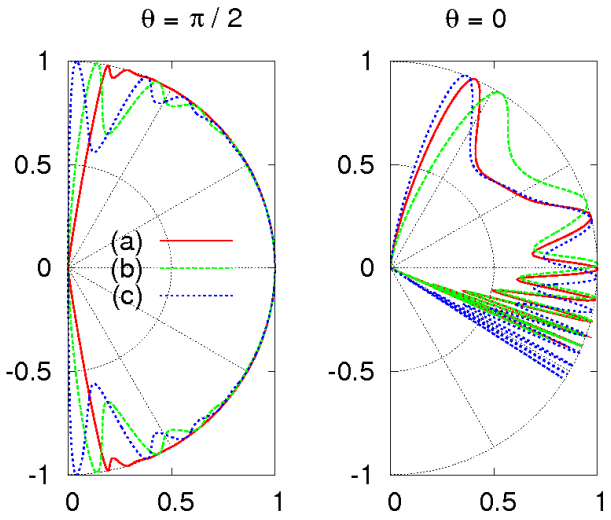

Figure 6.3: Same as Fig. 6.2, but for $E = 150$ meV and $D = 100$ nm.

Figs. 6.2 and 6.3 show our results for the tunneling transmission $T = T(\varphi)$, Eq. (6.10), as a function of the incidence angle φ, for $E = 80$ meV, $D = 100$ nm (Fig. 6.2) and $E = 150$ meV, $D = 100$ nm (Fig. 6.3). In both figures, left (*resp.*, right) panel refers to uniaxial strain applied along the zig-zag ($\theta = \pi/2$; *resp.*, armchair, $\theta = 0$) direction.

In the case of strain applied along the zig-zag direction ($\theta = \pi/2$, Figs. 6.2 and 6.3, left panels), curves (b) neglect a strain-induced deformation of the Dirac cone, namely we consider that the only effect of strain is to shift the Dirac point. Comparison with curves (c), where such a deformation is fully included, shows that the effect of a strain-induced anisotropy of the Fermi velocity is that of shifting the angular location of the maxima ($T = 1$, Eq. (6.12)) of the tunneling transmission. Such an effect becomes more important with increasing energy (from Fig. 6.2 to Fig. 6.3), while the number of peaks increases, Eq. (6.12), and the angular range in which the propagating regime is allowed widens. The effect of a strain-induced deformation of the Dirac cone is even more dramatic in the absence of a gate potential [$U_g = 0$ meV, curve (a)]. Indeed, in such a case, neglecting the Fermi velocity anisotropy for strain applied along the zig-zag direction would yield a uniform tunneling transmission $T = 1$, for all incidence angles φ, whereas we find that transmission via propagating waves is allowed only for $|\varphi| \leq \arcsin[(1 - \lambda_y \varepsilon)^{-1}]$, with small oscillations below $T = 1$ within, and evanescent waves beyond that range. A similar analysis applies to the case of strain applied along the armchair direction

($\theta = 0$, Figs. 6.2 and 6.3, right panels), which is characterized by an asymmetric transmission $T = T(\varphi)$, with pronounced oscillations for $\varphi > 0$ close to the propagating edge.

The origin of such an asymmetry of the φ-dependence of the transmission can be traced back to the particular Dirac cone vertex, whose shift is here considered. Global symmetry would be restored upon inclusion of the other Dirac cone. In that case, one would obtain the same picture, but with $\varphi \mapsto -\varphi$. It should be emphasized that the stationarity condition, Eq. (6.12), characterizes the occurrence of peaks in the transmission $T(\varphi)$ in any case. In addition, for a potential barrier, in the absence of strain, one also recovers complete transmission ($T = 1$) at $\varphi = 0$ (Klein tunneling) .

Summarizing, we have obtained that the overall effect of a strain-induced deformation of the Dirac cones, besides the shift of the Dirac point, is that of shifting the transmission peaks, and of reducing the range in φ at which transmission takes place.

6.1.1 Ballistic transport of a single strain-barrier

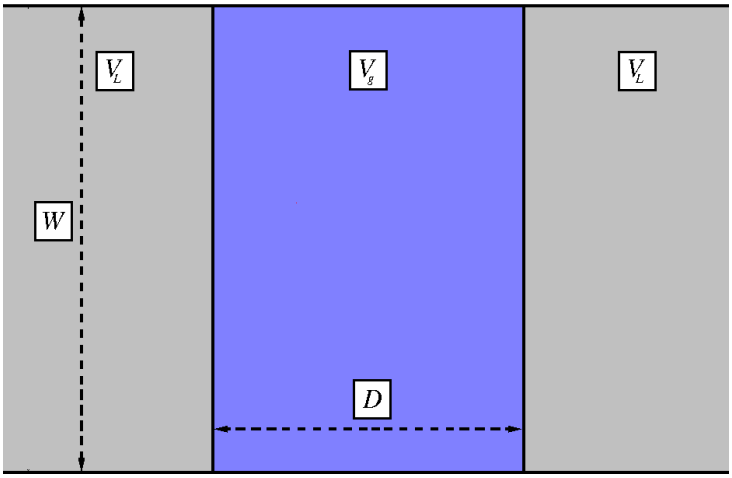

Figure 6.4: Schematic top view of a graphene layer contacted by metallic leads.

Now we consider a more realistic device, *viz.* a graphene strip of length D and width W, subjected to two heavily doped leads at a distance D (Fig. 6.4) [33, 50, 66, 145]. Following Ref. [145], we assume that $W/D \gg 1$, and that the gate potential within the strip is much less

than the potential of the leads, $|V_g| \ll |V_L|$. Moreover, we assume that the graphene strip is characterized by uniaxial strain, with modulus ε and strain direction θ, whereas the leads are treated as heavily doped unstrained graphene.

We can describe the strained graphene strip as a mesoscopic system connected to two reservoirs (the leads). We assume that the reservoirs are so large that they can be characterized by a well-defined temperature and chemical potential. We consider the limit of zero temperature, whereas the chemical potential of both leads is equal to $-eV_L$. Then we assume that the voltage applied between the two leads is infinitesimal. In these conditions, we can treat the system as in the stationary regime.

In order to obtain information about ballistic transport properties of the system we use the same procedure followed to obtain the transmission function in Eq. (6.10). Since the leads are heavily doped we will consider the limit $|V_L| \to \infty$, which is equivalent to impose the limit $\varphi \to 0$ to the transmission function expressed in Eq. (6.10). Thus we have

$$T_\alpha^{\mathrm{prop}}(E, k_y) = \frac{1}{\cos^2(q_x D) + g_\alpha(E, k_y)\sin^2(q_x D)}, \tag{6.13}$$

for propagating waves in the valley $\alpha = K$, and

$$g_\alpha(E, k_y) = \frac{(E - U_g)^2}{(E - U_g)^2 - \hbar^2 v_{\mathrm{F}}^2 (1 - \lambda_y \varepsilon)^2 (k_y \mp q_{\mathrm{D}y})^2}, \tag{6.14}$$

and the minus (*resp.*, plus) sign applies to the valley $\alpha = K$ (*resp.*, $\alpha = K'$). Analogous expressions hold for the transmission $T_\alpha^{\mathrm{evan}}(k_y)$ in the evanescent case, with $g_\alpha(k_y) \mapsto -g_\alpha(k_y)$, $\cos(q_x D) \mapsto \cosh(q_x D)$, and $\sin(q_x D) \mapsto \sinh(q_x D)$. The transmission for a general (propagating or evanescent) wave therefore reads

$$T_\alpha(E, k_y) = \Theta[g_\alpha(E, k_y)] T_\alpha^{\mathrm{prop}}(E, k_y) + (1 - \Theta[g_\alpha(E, k_y)]) T_\alpha^{\mathrm{evan}}(E, k_y). \tag{6.15}$$

Integrating over k_y and summing over both valleys, one obtains the conductance across the barrier, following the Landauer approach [26, 81],

$$G(E) = \frac{2e^2}{h} W \sum_\alpha \int_{-\infty}^{\infty} \frac{dk_y}{2\pi} T_\alpha(E, k_y), \tag{6.16}$$

where the factor of 2 takes into account for the spin degeneracy, the conductivity

$$\sigma = \frac{D}{W} G, \tag{6.17}$$

and the Fano factor [13]

$$F(E) = 1 - \frac{\sum_\alpha \int_{-\infty}^{\infty} \frac{dk_y}{2\pi} T_\alpha^2(E, k_y)}{\sum_\alpha \int_{-\infty}^{\infty} \frac{dk_y}{2\pi} T_\alpha(E, k_y)}. \tag{6.18}$$

In the zero-temperature limit the thermal noise, or Johnson-Nyquist noise, is vanishing. In such a limit, the fundamental source of noise is due to charge quantization. This kind of noise is called shot noise [13]. The shot noise is quantified by the dimensionless Fano factor, which is defined as the ratio between the noise power spectrum and the average conductance [34].

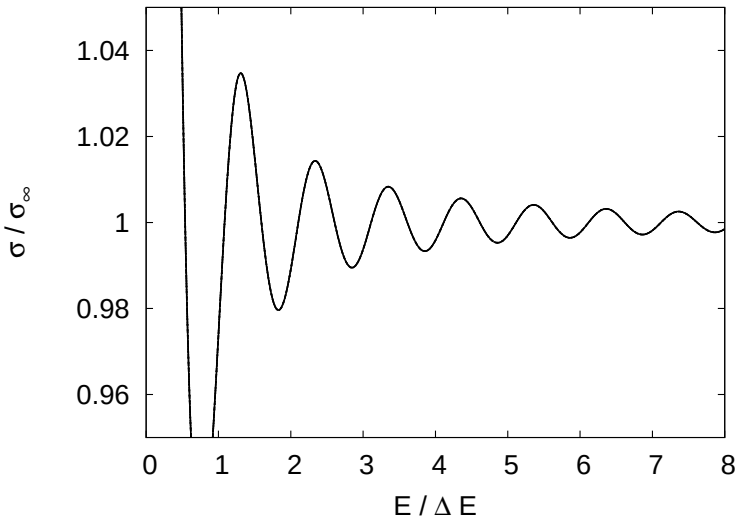

Figure 6.5: Conductivity across a graphene strip ($D = 100$ nm) normalized to asymptotic large-energy behavior, Eq. (6.23), *vs.* energy scaled to the pseudoperiod, Eq. (6.24). Actually shown are four curves, all collapsing into a single one, corresponding to strain applied along the armchair direction ($\theta = 0$), with $\varepsilon = 0.03, 0.05, 0.10, 0.15$.

Before discussing our results, let us observe that the inclusion of a strain-induced deformation of the Dirac cone in the expressions of the conductivity, Eq. (6.17), and of the Fano factor,

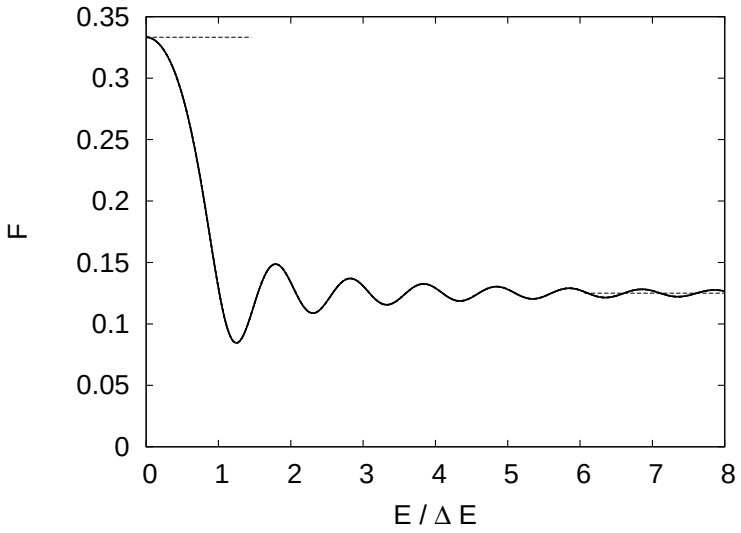

Figure 6.6: Fano factor for ballistic transport across a graphene strip. All parameters are as in Fig. 6.5. Dashed lines represent the universal low- and large-energy asymptotic values, $F(0) = \frac{1}{3}$ and $F_\infty = \frac{1}{8}$, respectively.

Eq. (6.18), amounts to the replacements

$$D \;\mapsto\; D_{\text{eff}} \equiv \xi D, \tag{6.19a}$$

$$E \;\mapsto\; E_{\text{eff}} \equiv \zeta E, \tag{6.19b}$$

for the strip width and incident energy, respectively, in the corresponding expressions, $\sigma^{(0)}$ and $F^{(0)}$, say, without cone deformation, with

$$\xi \;=\; \frac{1-\lambda_y\varepsilon}{1-\lambda_x\varepsilon}, \tag{6.20a}$$

$$\zeta \;=\; \frac{1}{1-\lambda_y\varepsilon}. \tag{6.20b}$$

In particular, one explicitly finds

$$\sigma(D;E) = \xi^{-1}\sigma^{(0)}(D_{\text{eff}};E_{\text{eff}}). \tag{6.21}$$

As a consequence, while $\lim_{E\to 0}\sigma^{(0)}(D,E) = 4e^2/\pi h$, a universal constant [142], in the pres-

ence of applied uniaxial strain one finds

$$\lim_{E\to 0}\sigma(D;E)=\frac{1}{\xi}\frac{4e^2}{\pi h}. \tag{6.22}$$

Only in the case of hydrostatic strain ($\nu=-1$, $\lambda_x=\lambda_y$, $\xi=1$) one recovers the universal limit, regardless of the strain modulus [33]. On the other hand, one finds $\lim_{E\to 0}F(D;E)=\frac{1}{3}$, which is smaller than the value $F=1$ expected for a Poisson process. This value is the same regardless of applied strain [145]. In the limit $E\to 0$, the ballistic transport is purely due to the evanescent modes. In particular, we have found that the shot noise due to the evanescent modes is insensitive to the presence of uniaxial strain.

In the opposite limit ($E\to\infty$), the ballistic transport is mainly due to the propagating modes, whereas the effect due to the evanescent modes is negligible. In the high energy limit, the conductivity across a single barrier in the absence of strain is linear in energy, $\sigma^{(0)}\approx(e^2/h)D|E|/\hbar v_{\rm F}$, with damped oscillations characterized by a pseudoperiod ΔE such that $D\Delta E/\hbar v_{\rm F}=\pi$ [66]. In the presence of strain, such results are modified by Eqs. (6.20), so that $\sigma(E)\approx\sigma_\infty(E)$ for $E\to\infty$, with

$$\sigma_\infty(E)=\frac{4e^2}{h}\frac{D|E|}{4}\zeta, \tag{6.23}$$

with damped oscillations characterized by a pseudoperiod given by

$$\xi\zeta D\frac{\Delta E}{\hbar v_{\rm F}}=\pi. \tag{6.24}$$

In view of the fact that $|\lambda_x|>|\lambda_y|$, one may conclude that applied strain induces a slight change in the slope of σ *vs* $|E|$, while it modifies the pseudoperiod of the oscillations more substantially.

Fig. 6.5 shows our results for the scaled conductivity in the presence of uniaxial strain ($\varepsilon=0.03-0.15$) applied along the armchair direction ($\theta=0$). When the conductivity $\sigma(E)$ is normalized with respect to its asymptotic limit, Eq. (6.23), and plotted against energy E scaled with the strain-dependent pseudoperiod ΔE, Eq. (6.24), results corresponding to different values of the strain modulus collapse into a single curve, displaying damped oscillations, as prescribed by Eq. (6.24). Similarly, Fig. 6.6 reports our results for the Fano factor as a function

of scaled energy. Again, the results for all the strain moduli here considered ($\varepsilon = 0.03 - 0.15$) collapse into a single, oscillating curve. Note that the universal limits $F(E = 0) = \frac{1}{3}$ and $F_\infty \equiv \lim_{E\to\infty} F(E) = \frac{1}{8}$ are recovered in all cases, regardless of applied strain. Such results do not depend on the direction θ of applied strain.

6.2 Transmission across multiple strain-barriers

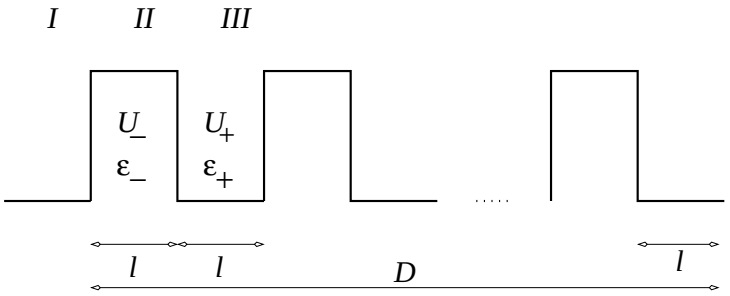

Figure 6.7: Schematic plot of the multiple barrier.

Now we consider quasiparticle tunneling across N identical barriers, each of width ℓ, two nearest neighbor (NN) barriers being separated by the distance ℓ, such that $2N\ell = D$ (Fig. 6.7). We assume a position-dependent strain modulus $\varepsilon(x)$ and gate potential energy $U(x)$, with

$$\varepsilon(x) = \varepsilon_-, \quad 2(m-1)\ell \le x \le (2m-1)\ell, \tag{6.25a}$$

$$= \varepsilon_+, \quad (2m-1)\ell \le x \le 2m\ell, \tag{6.25b}$$

and

$$U(x) = U_-, \quad 2(m-1)\ell \le x \le (2m-1)\ell, \tag{6.26a}$$

$$= U_+, \quad (2m-1)\ell \le x \le 2m\ell, \tag{6.26b}$$

with $m = 1, \ldots N$. We further consider the possibility of contacting the two extrema of the chain of barriers with leads at the potential V_L. First of all we consider the leads at zero potential $V_L = 0$, that means that the superstructure is contacted with pristine graphene. Eqs. (6.9) then

suggest to look for a solution of the Dirac equation in the form

$$\psi(x,y) = U^{\dagger}(\theta)\frac{\phi(x)}{\sqrt{1-\lambda_x\varepsilon(x)}}e^{ik_y y} \tag{6.27}$$

so that $\phi(x)$ is a continuous function at the barriers' edges. The stationary Dirac equation for $\phi(x)$ can then be cast in the form of an evolution equation [66], so that $\phi(x) = \mathbb{T}^{(N)}(x,x_0)\phi(x_0)$, where the evolution matrix $\mathbb{T}^{(N)}(x,x_0)$ in turn obeys the equation

$$\begin{aligned}\frac{d}{dx}\mathbb{T}^{(N)}(x,x_0) &= \left[iq_{\mathrm{D}x}^{(0)}\varepsilon(x)\tau_z + \frac{i}{\hbar v_{\mathrm{F}}}\frac{E-U(x)}{1-\lambda_x\varepsilon(x)}\sigma_x\right.\\ &\left.+\frac{1-\lambda_y\varepsilon(x)}{1-\lambda_x\varepsilon(x)}\left(k_y - q_{\mathrm{D}y}^{(0)}\varepsilon(x)\tau_z\right)\sigma_z\right]\mathbb{T}^{(N)}(x,x_0),\end{aligned} \tag{6.28}$$

with $\mathbb{T}^{(N)}(x_0,x_0) = \mathbb{I}_4$, and where $\mathbf{q}_{\mathrm{D}}^{(0)}$ is the strain independent prefactor of the shifted Dirac point $\mathbf{q}_{\mathrm{D}} = \mathbf{q}_{\mathrm{D}}^{(0)}\varepsilon$. The evolution matrix is related to the transfer matrix by [142]

$$\mathbb{M}^{(N)}(x,x_0) = Q_s^{-1}(\varphi)\mathbb{T}^{(N)}(x,x_0)Q_s(\varphi), \tag{6.29}$$

where

$$Q_s(\varphi) = \frac{1}{\sqrt{2}}\begin{pmatrix}1 & 1\\ se^{i\varphi} & -se^{-i\varphi}\end{pmatrix} \tag{6.30}$$

includes the incidence angle φ of the incoming spinor, Eq. (6.8a), and $s = \mathrm{sgn}\,(E)$. Since there is no mixing between the two valleys K and K', it is possible the transfer matrix in the block diagonal form

$$\mathbb{M}^{(N)}(x,x_0) = \begin{bmatrix}\mathbb{M}_K^{(N)}(x,x_0) & 0\\ 0 & \mathbb{M}_{K'}^{(N)}(x,x_0)\end{bmatrix}, \tag{6.31}$$

each block being related to one valley index (K or K').

Similarly to the previous case, since the strain superlattice is uniform along the coordinate orthogonal to the direction of applied strain, say y, stationary eigenmodes will be characterized by constant energy E, transverse wave vector k_y and valley index K or K'. Replacing $\mathbf{q}_{\mathrm{D}}$ with $-\mathbf{q}_{\mathrm{D}}$ in the matrix $\mathbb{M}_K^{(N)}(x,x_0)$, one obtains the matrix $\mathbb{M}_{K'}^{(N)}(x,x_0)$. Hence, for simplicity here we consider that the valley index is K and we omit to write the chosen index.

For the transfer matrix across the first, say, barrier in Fig. 6.7, one finds $\mathbb{M}^{(1)}(2\ell,0) =$

$e^{iq_{\mathrm{D}x}^{(0)}(\varepsilon_+ + \varepsilon_-)\ell}\tilde{\mathbb{M}}^{(1)}$, where $\tilde{\mathbb{M}}^{(1)}$ is a unimodular matrix, $\det \tilde{\mathbb{M}}^{(1)} = 1$. Specifically, one obtains

$$\tilde{\mathbb{M}}_{11}^{(1)} = \lambda + i\eta, \tag{6.32a}$$

$$\lambda = \frac{\sinh(q_-\ell)}{q_-}\frac{\sinh(q_+\ell)}{q_+}(\kappa_-\kappa_+ - u_-u_+) + \cosh(q_-\ell)\cosh(q_+\ell), \tag{6.32b}$$

$$\eta = i\Big[\frac{u_+u_- - \kappa_+\kappa_-}{q_+q_-}\sinh(q_-\ell)\cosh(q_+\ell) - \sinh(q_+\ell)\cosh(q_-\ell)\Big], \tag{6.32c}$$

where λ is always real, whereas η can be real or purely imaginary, depending on k_y and E. More compactly, one also finds

$$\tilde{\mathbb{M}}_{11}^{(1)} = \exp(q_+\ell)\left[\frac{\kappa_+\kappa_- - u_+u_-}{q_+q_-}\sinh(q_-\ell) + \cosh(q_-\ell)\right]. \tag{6.33}$$

In Eqs. (6.32) and (6.33), we have employed the definitions

$$\kappa_\pm = \frac{1 - \lambda_y\varepsilon_\pm}{1 - \lambda_x\varepsilon_\pm}(k_y - q_{\mathrm{D}y}^{(0)}\varepsilon_\pm), \tag{6.34a}$$

$$u_\pm = \frac{E - U_\pm}{\hbar v_{\mathrm{F}}(1 - \lambda_x\varepsilon_\pm)}, \tag{6.34b}$$

$$q_\pm = \sqrt{\kappa_\pm^2 - u_\pm^2}. \tag{6.34c}$$

Making use of the Chebyshev identity for the Nth power of a unimodular matrix [156], for the transfer matrix across N identical barriers, one finds [116]

$$[\tilde{\mathbb{M}}^{(1)}]_{11}^N = \frac{\sinh(Nz)}{\sinh z}\tilde{\mathbb{M}}_{11}^{(1)} - \frac{\sinh[(N-1)z]}{\sinh z}, \tag{6.35}$$

where $\cosh z = \lambda$. Finally, the transmission can be related to the transfer matrix as

$$T_N(E, k_y) = \left|[\tilde{\mathbb{M}}^{(1)}]_{11}^N\right|^{-2}. \tag{6.36}$$

We are now in the position to discern whether an electronic mode is characterized by an oscillating or evanescent behavior far from the barrier superlattice. To this aim, we preliminarly observe that, depending on E and k_y, one has a propagating (*resp.*, evanescent) wave for $q_\pm^2 < 0$ (*resp.*, $q_\pm^2 > 0$), where the subscript $+$ refers to the region between two consecutive barriers [$(2m-1)\ell \leq x \leq 2m\ell$, $m = 1, \ldots N$], and the subscript $-$ refers to the region within a barrier

$[2(m-1)\ell \leq x \leq (2m-1)\ell, m = 1, \ldots N]$ (Fig. 6.7).

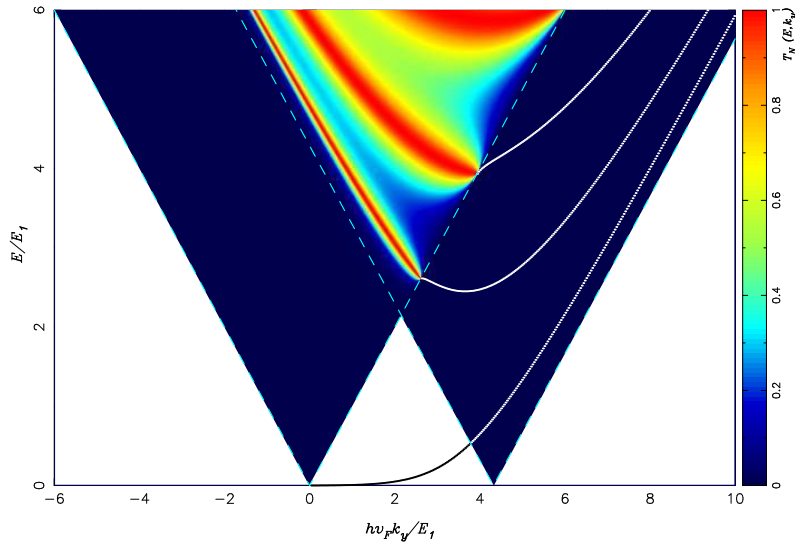

Figure 6.8: Single electron transmission $T_1(E, k_y)$, Eq. (6.36) across a single barrier ($N = 1$, $\ell = 25$ nm), as a function of scaled transverse wave vector $\hbar v_{\rm F} k_y/E_1$ and scaled energy E/E_1, Eq. (6.37), with $E_1 \approx 40$ meV. Here, strain is applied along the armchair direction, $\theta = 0$, and we set $\varepsilon_- = 0.02$, $\varepsilon_+ = 0$, and $U_\pm = 0$. Cyan dashed lines delimit cones corresponding to the (deformed) Dirac cones outside (left cone) and within (right cone) the barrier (regions I+III and II, respectively, in Fig. 6.7). Solid lines outside the left Dirac cone correspond to bound modes.

Fig. 6.8 shows the single electron transmission $T_N(E, k_y)$ across a single barrier, Eq. (6.36) with $N = 1$, as a function of the transverse wave vector $\hbar v_{\rm F} k_y/E_1$ and energy E/E_1, each scaled by the characteristic energy

$$E_1 = \frac{\pi \hbar v_{\rm F}}{2\ell\gamma}, \tag{6.37}$$

where $\gamma = \frac{1}{2}[(1-\lambda_x\varepsilon_+)^{-1} + (1-\lambda_x\varepsilon_-)^{-1}]$. Here and in the following, strain is applied along the armchair direction, $\theta = 0$, and we set $\varepsilon_- = 0.02$, $\varepsilon_+ = 0$, and $U_\pm = 0$. In Fig. 6.8, cyan dashed lines delimit the two (deformed) Dirac cones defined by $q_+^2 < 0$ (left cone) and $q_-^2 < 0$ (right cone), corresponding to regions I+III and II in Fig. 6.7), respectively. One finds that $T_1(E, k_y)$ is defined within the left cone and is exponentially vanishing within the intersection between both cones. This corresponds to having propagating modes in all the three regions. In this case, resonant modes, *i.e.* propagating modes with unit transmission, are characterized by the condition for stationary waves

$$\tilde{q}_-\ell = m\pi, \tag{6.38}$$

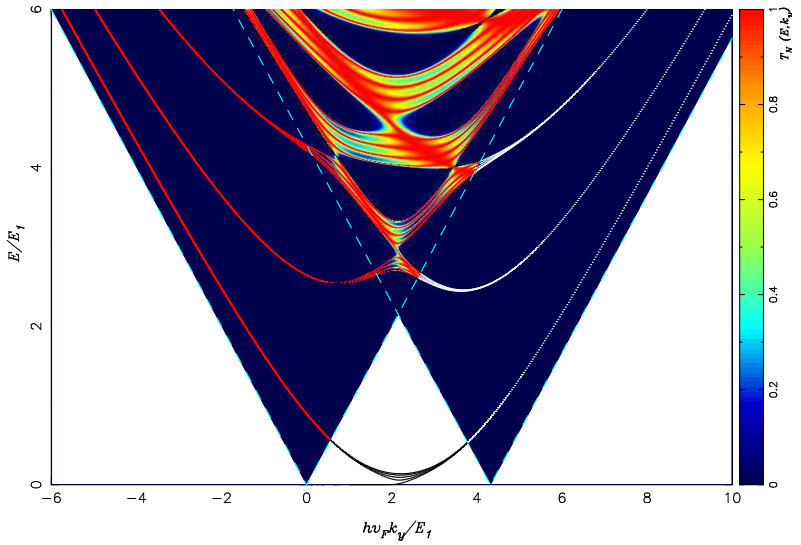

Figure 6.9: Single electron transmission $T_5(E, k_y)$, Eq. (6.36) across a superlattice of $N = 5$ identical barriers (Fig. 6.7), as a function of scaled transverse wave vector $\hbar v_{\mathrm{F}} k_y/E_1$ and scaled energy E/E_1, Eq. (6.37). All other parameters are as in Fig. 6.8. Red lines outside the right cone correspond to resonant modes.

where $q_- = i\tilde{q}_-$, and m is an integer. We have just seen this condition in the previous paragraph, cf. Eq. (6.12).

Fig. 6.9 shows the single electron transmission $T_N(E, k_y)$ across a superlattice composed of five identical barriers, Eq. (6.36) with $N = 5$. Again, nonzero values of the transmission are to be found within the intersection of the Dirac cones corresponding to the region inside a barrier and between two consecutive barriers. However, at variance of the case $N = 1$, because of multiple scatterings, a nonzero transmission is also possible beyond the cone $q_-^2 < 0$. This corresponds to having evanescent modes within the barriers. Such a phenomenon is analogous to what happens to photons propagating across a 1D photonic crystal with alternative layers of a left-handed and a right-handed material (1D metamaterial) [154]. As for resonant modes, $T_N(E, k_y) = 1$, besides the ones given by Eq. (6.38) regardless of N, additional resonant modes are given by the condition

$$\lambda = \cos\left(\frac{\pi j}{N}\right), \quad j = 1, \ldots N-1, \tag{6.39}$$

where λ is defined by Eq. (6.32b), and $|\lambda| < 1$. The latter condition implies that these resonant modes have globally propagating behavior. Comparing Figs. 6.8 and 6.9, one finds that, in the

domain within both Dirac cones, in addition to the resonant modes given by Eq. (6.38), in the case $N > 1$ there exist $N - 1$ new resonant modes given by Eq. (6.39). It should also be noted that in the domain within the left cone but outside the second the resonant modes, which are only given by Eq. (6.39), are characterized by quite narrow lines in the transmission plots.

Outside the left Dirac cone, it is still possible to find bound states [7, 94, 120]. Within the transfer matrix method, these are given by the condition $[\tilde{\mathbb{M}}^{(1)}]_{11}^{N} = 0$. For $q_+^2 > 0$ one finds evanescent modes outside the barriers, and therefore also far from the superlattice structure. In the case $N = 1$, one finds several such confined modes within the second cone (Fig. 6.8, solid lines outside the left cone), whereof only one such mode survives in the region outside both cones. The latter is the surface mode analyzed in Ref. [120]. In the case $N > 1$ (Fig. 6.9, solid lines outside the right cone), one finds that to each bound mode in the single barrier case there correspond exactly N bound states outside either cones. This is remindful of electron bands in solids, where the overlap of N periodically arranged atomic orbitals give rise to a band of N states.

6.2.1 Ballistic transport of multiple strain-barriers

Similarly to the case of a single strain barrier, we consider now a strain graphene superstructure, Fig. 6.7, in contact with two metallic leads. These are described by two highly doped semi-infinite graphene samples. In the leads we assume to have a potential $|V_L| \to \infty$. The presence of the leads has no effect on the evolution matrix, that we have just obtained for the superstructure, but it induces a modification of the transfer matrix. Indeed, in the limit $|V_L| \to \infty$ the transfer matrix is related to the evolution matrix for any energy E and transverse wavevector k_y by

$$\mathbb{M}^{(N)}(x, x_0) = Q_s^{-1}(0)\mathbb{T}^{(N)}(x, x_0)Q_s(0), \tag{6.40}$$

with $Q_+(0) = \frac{1}{\sqrt{2}}(\sigma_z + \sigma_x)$, $Q_+^{-1}(0) = Q_+(0)$, $Q_-(0) = Q_+(0)\sigma_x$, $Q_-^{-1}(0) = \sigma_x Q_+(0)$, and $s = \mathrm{sgn}\,(V_L)$. Following the transfer matrix method that we have just used, we have

$$\left(\tilde{\mathbb{M}}_1\right)_{11} = \lambda + i\eta, \tag{6.41}$$

where

$$\lambda = \frac{\sinh(q_-\ell)}{q_-}\frac{\sinh(q_+\ell)}{q_+}(\kappa_-\kappa_+ - u_-u_+) + \cosh(q_-\ell)\cosh(q_+\ell), \tag{6.42a}$$

$$\eta = \frac{u_-}{q_-}\sinh(q_-\ell)\cosh(q_+\ell) + \frac{u_+}{q_+}\sinh(q_+\ell)\cosh(q_-\ell), \tag{6.42b}$$

where we have used the definitions in Eqs. (6.34). We are taking into account the case labeled with K valley, but in order to obtain the case labeled with K' one needs to replace $\mathbf{q}_\mathrm{D}$ with $-\mathbf{q}_\mathrm{D}$. Moreover, exploiting the Chebyshev identity (6.35) and Eq. (6.36) one finds the transmission function explicitly

$$\begin{aligned} T_\alpha(E,k_y) &\equiv T_\alpha^{\mathrm{prop}}(E,k_y) \\ &= \left[\cos^2(Ny) + \frac{\eta^2}{\lambda^2-1}\sin^2(Ny)\right]^{-1}, \end{aligned} \tag{6.43a}$$

with $y = \arccos\lambda$, if $|\lambda| < 1$,

$$\begin{aligned} &\equiv T_\alpha^{\mathrm{evan}}(E,k_y) \\ &= \left[\cosh^2(Nx) + \frac{\eta^2}{\lambda^2-1}\sinh^2(Nx)\right]^{-1}, \end{aligned} \tag{6.43b}$$

with $x = \log|\lambda + \sqrt{\lambda^2-1}|$, if $|\lambda| > 1$,

$$= [1+\eta^2N^2]^{-1}, \tag{6.43c}$$

if $|\lambda| = 1$. We remind that both λ and η are dependent on the energy E, the component k_y of the wavevector and the valley index K or K'.

Making use of Eqs. (6.43) for the transmission $T_\alpha(E,k_y)$ in Landauer's formula for the conductivity, Eq. (6.16), and in the definition for the Fano factor, Eq. (6.18), one again finds that the conductivity in strained graphene, and strained graphene where the strain-induced velocity anisotropy has been neglected, are related by means of Eqs. (6.20), (6.21), but now with $D =$

$2N\ell$, and

$$\xi = \frac{1}{2}(\xi_+ + \xi_-), \tag{6.44a}$$

$$\zeta = \frac{1}{2}(\zeta_+ + \zeta_-), \tag{6.44b}$$

$$\xi_\pm = \frac{1-\lambda_y\varepsilon_\pm}{1-\lambda_x\varepsilon_\pm}, \tag{6.44c}$$

$$\zeta_\pm = \frac{1}{1-\lambda_y\varepsilon_\pm}. \tag{6.44d}$$

Eq. (6.22) in the limit $E \to 0$ then follows straightforwardly, with ξ given now by Eq. (6.44a). Moreover, the conductivity at large energies is characterized by an overall linear behavior, interrupted by dips with decreasing depth, which result from the coherent superposition of the damped oscillations produced by scattering off the edges of the single barriers. The energies E_n at which such dips occur are asymptotically given by

$$\frac{E_n}{\hbar v_{\rm F}}\frac{D}{N}\frac{1}{2}(\xi_+\zeta_+ + \xi_-\zeta_-) = n\pi, \tag{6.45}$$

with n an integer.

Fig. 6.10 shows our numerical results for the conductivity in strained graphene, with strain applied nonuniformly along the armchair direction, across a superlattice of $N = 10$ barriers. At variance with Fig. 6.5, we have not scaled σ with its asymptotic behavior at large energies, Eq. (6.23). As expected, the overall linear behavior of $\sigma(E)$ is interrupted by dips, whose approximate energy location is given by Eq. (6.45). While such dips get damped as energy increases, they are nonetheless enhanced with respect to the case in which the strain-induced deformation of the Dirac cones is neglected [50], especially those corresponding to even integer values of n in Eq. (6.45). Correspondingly, the Fano factor (Fig. 6.11) is characterized by essentially analogous features, with bumps occurring at approximately E_n, Eq. (6.45). In particular, the universal limit at low energy, $F(0) = \frac{1}{3}$, is recovered as in the single-barrier case, regardless of applied strain.

Fig. 6.12 shows our numerical results for the conductivity in strained graphene, but now for nonuniform strain applied along the zig-zag direction. At variance with the armchair case (Fig. 6.10), for strain applied along the zig-zag direction the conductivity seems not to be char-

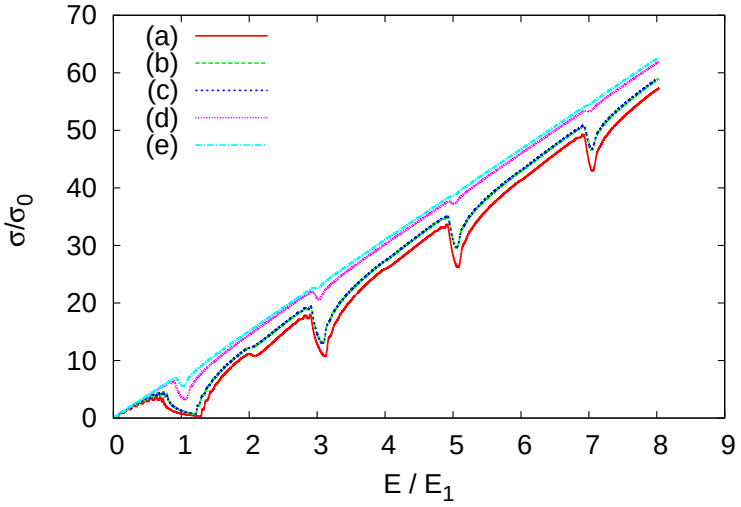

Figure 6.10: Conductivity $\sigma(E)$ in units of $\sigma_0 = 4e^2/h$, *vs.* energy E, scaled with respect to the approximate location of the first dip, E_1, as given by Eq. (6.45). Subsequent dips then occur close to integer values of the ratio E/E_1. Uniaxial strain is applied along the armchair direction ($\theta = 0$) in the case of a multibarrier superlattice, with $N = 10$ barriers, $\ell = 25$ nm ($D = 500$ nm). Different curves refer to nonuniform strain moduli within and outside NN barriers (cf. Fig. 6.7), with (a) $\varepsilon_+ = 0.004$, $\varepsilon_- = 0$; (b) $\varepsilon_+ = 0.003$, $\varepsilon_- = 0$; (c) $\varepsilon_+ = 0.002$, $\varepsilon_- = -0.001$; (d) $\varepsilon_+ = 0.002$, $\varepsilon_- = 0.001$; (e) $\varepsilon_+ = 0.0005$, $\varepsilon_- = 0$. In all cases, we set $U_\pm = 0$, for the sake of simplicity.

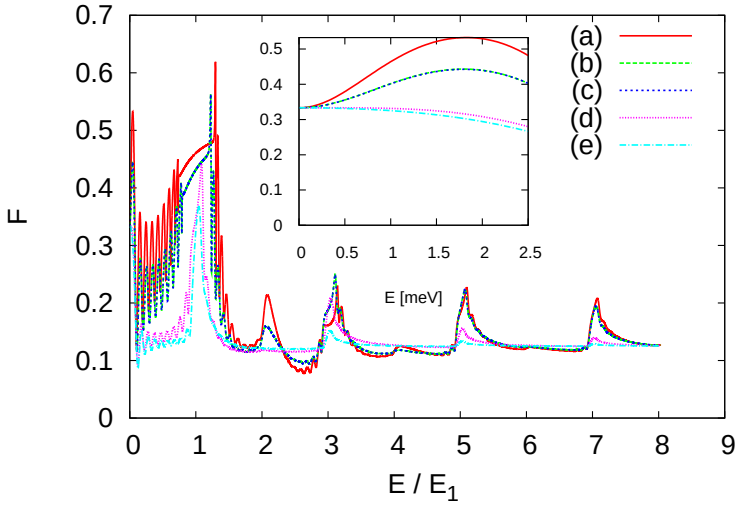

Figure 6.11: Fano factor F *vs.* scaled energy E/E_1, for transport across a multibarrier superlattice, with nonuniform uniaxial strain applied along the armchair direction ($\theta = 0$). All parameters are as in Fig. 6.10. Inset shows the universal low-energy asymptotic behavior in the various cases. In the limit $E \to 0$, the universal asymptotic value, $F(0) = \frac{1}{3}$, is recovered.

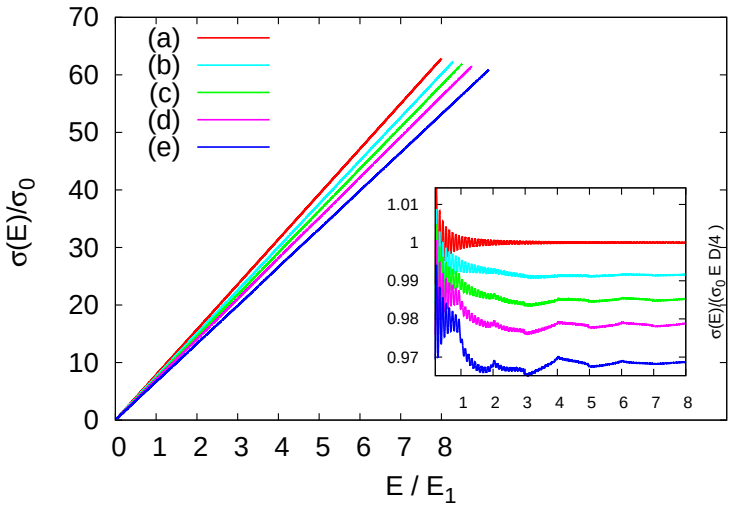

Figure 6.12: Conductivity $\sigma(E)$ in units of $\sigma_0 = 4e^2/h$, *vs.* energy E, scaled with respect to E_1, as given by Eq. (6.45). Uniaxial strain is applied along the zig-zag direction ($\theta = \pi/2$) in the case of a multibarrier superlattice, with $N = 10$ barriers, $\ell = 25$ nm ($D = 500$ nm). Different curves refer to nonuniform strain moduli within and outside NN barriers (cf. Fig. 6.7), with (a) $\varepsilon_+ = 0$, $\varepsilon_- = 0$; (b) $\varepsilon_+ = 0.03$, $\varepsilon_- = 0$; (c) $\varepsilon_+ = 0.05$, $\varepsilon_- = 0$; (d) $\varepsilon_+ = 0.07$, $\varepsilon_- = 0$; (e) $\varepsilon_+ = 0.10$, $\varepsilon_- = 0$. In all cases, we set $U_\pm = 0$, for the sake of simplicity. Inset shows the conductivity scaled with respect to its large-energy asymptotic limit, σ/σ_∞, as a function of scaled energy, E/E_1.

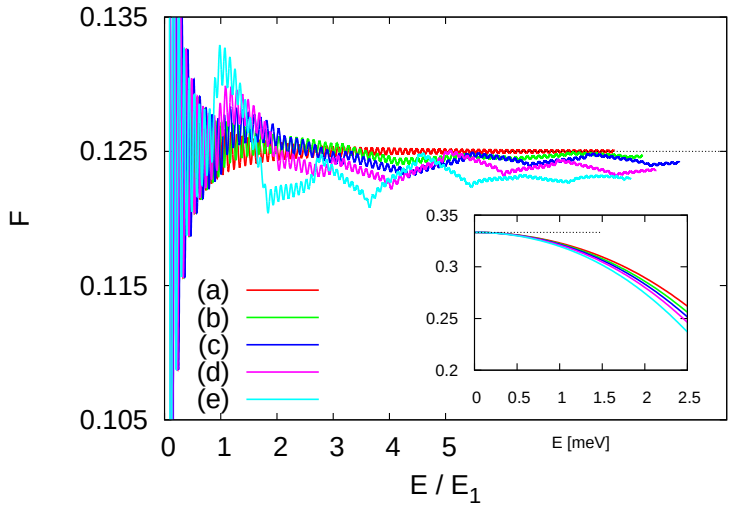

Figure 6.13: Fano factor F *vs.* scaled energy E/E_1, for transport across a multibarrier superlattice, with nonuniform uniaxial strain applied along the zig-zag direction ($\theta = \pi/2$). All parameters are as in Fig. 6.12. Note the deviations from the large-energy asymptotic limit for the unstrained case, $F_\infty = \frac{1}{8}$ (dashed line). The low-energy universal limit, $F(0) = \frac{1}{3}$ (inset, dashed line), is recovered, regardless of strain.

acterized by prominent dips as a function of energy. This may be explained by a reduced coherent superposition of the effects due to each single barrier. However, if the trailing linear dependence on energy is divided out (Fig. 6.12, inset), one may again recognize 'oscillations', with extrema approximatively occurring at E_n, as given by Eq. (6.45). At variance with the armchair case, the Fano factor exhibits a strain-dependent asymptotic limit, for large energies (Fig. 6.13), with increasing deviations from the unstrained behavior $F_\infty = \frac{1}{8}$, with increasing strain modulus ε (at least within the strain range that has been numerically investigated). On the other hand, both the oscillations as a function of scaled energy E/E_1 and the low-energy limit $F(0) = \frac{1}{3}$ (Fig. 6.13, inset) are recovered.

6.3 Trasmission across a smooth barrier: effect of continuous strain

Although considerable insight is afforded by analytical solutions to the problem of tunneling across single or multiple *sharp* barriers, there is sufficient evidence, both experimental [83] and theoretical [29], that barrier edge effects are also important to determine the transport properties across corrugated graphene. Here, we therefore consider the case in which uniaxial strain is applied in a nonuniform but continuous fashion to a graphene sheet, which can be modeled by a single barrier with *smooth* strain and gate potential profiles, $\varepsilon = \varepsilon(x)$ and $U = U(x)$, respectively.

On quite general grounds, one may expect that a smooth potential profile (whether induced by strain or by gating) introduces a new length scale, a say [as in Eq. (6.49) below]. At the beginning of this Chapter we have studied the electronic transmission through a sharp strain barrier, and we remind that this approximation holds whenever $\mathsf{a} \ll \lambda_\mathrm{F}$. On the other hand, the detailed structure of the barrier needs to be considered when $\mathsf{a} \sim \lambda_\mathrm{F}$. Similarly to the sharp barrier case, we are interested to the more general and realistic cases where $a \ll \mathsf{a}$, where one may neglect the occurrence of K–K' coupling. Indeed, truly sharp electrostatic barriers on the order of the electron wavelength are quite difficult to be realized, as is *e.g.* demonstrated by the occurrence of Fabry-Pérot oscillations of the conductance in graphene heterostructures

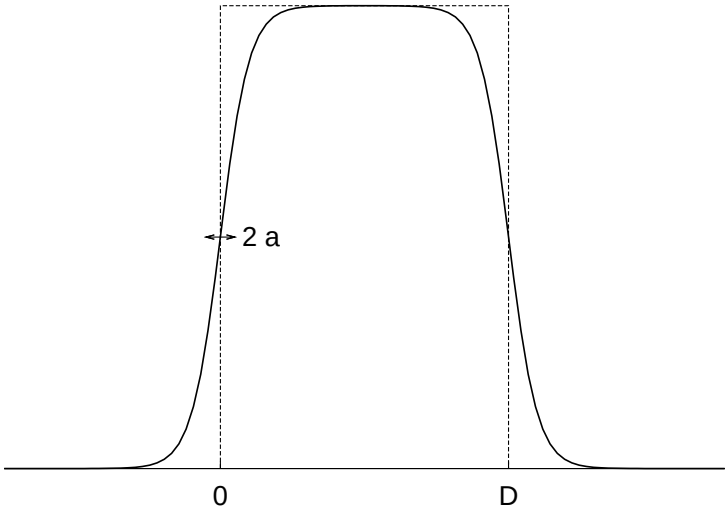

Figure 6.14: Schematic single tunneling barrier, with smooth strain profile, Eq. (6.49). Dashed line depicts a sharp barrier, corresponding to the limit a $\to 0$.

as narrow as ~ 20 nm, where a resonant cavity is formed between two electrostatically created bipolar junctions [157]. Such oscillations are more accurately described when the smooth structure of these potential barriers is taken into account, whereas intervalley scattering can be safely neglected (see Supplementary Information in Ref. [157]). Another instance of nonuniform barrier, where smoothing effects are important, is the strain-induced ripples superlattice experimentally realized in Ref. [6], which smoothing is essential on a length scale of ~ 100 nm, whereas intervalley processes are negligible.

In order to generalize the Hamiltonian for graphene subjected to uniform strain Eq. (6.1) to the case of a nonuniform, but continuous strain profile $\varepsilon = \varepsilon(x)$, one may be tempted to perform the replacements $v_i \mapsto v_i(\mathbf{r}) \equiv v_{\rm F}[1 - \lambda_i \varepsilon(x)]$ and $\mathbf{q}_{\rm D} \mapsto \mathbf{q}_{\rm D}(\mathbf{r})$, with $\varepsilon = \varepsilon(x)$. However, the resulting Hamiltonian must be symmetrized, in order to preserve hermiticity, thus leading to the model Hamiltonian for a nonuniform strain profile:

$$H = \int d\mathbf{r} \Psi^\dagger(\mathbf{r}) \frac{1}{2} \left\{ \hbar v_j(\mathbf{r}) \left[\tau_0 \mathcal{U}^\dagger(\theta) \sigma_j \frac{1}{i} \nabla_j \mathcal{U}(\theta) - \tau_z \mathcal{U}^\dagger(\theta) \sigma_j q_{{\rm D}j}(\mathbf{r}) \mathcal{U}(\theta) \right] + \right.$$
$$\left. + \left[\tau_0 \mathcal{U}^\dagger(\theta) \sigma_j \frac{1}{i} \nabla_j \mathcal{U}(\theta) - \tau_z \mathcal{U}^\dagger(\theta) \sigma_j q_{{\rm D}j}(\mathbf{r}) \mathcal{U}(\theta) \right] \hbar v_j(\mathbf{r}) \right\} \Psi(\mathbf{r}) \qquad (6.46)$$

Eq. (6.46) includes the effect of nonuniform, continuous strain both as a shift in the position of

the Dirac points, and as a deformation of the Dirac cones (nonuniform and anisotropic Fermi velocity), at variance *e.g.* with Ref. [128], where a nonuniform velocity is considered, but an isotropic profile is assumed. As in the case of a single, sharp barrier, continuity of the current density, Eqs. (6.9), suggests to seek for a solution of the stationary Dirac equation in a form analogous to Eq. (6.27), *viz.*

$$\psi(x,y) = U^{\dagger}(\theta)\frac{\phi(x)}{\sqrt{v_x(x)}}e^{ik_y y}. \tag{6.47}$$

One explicitly finds [cf. Eq. (6.28)]

$$\frac{d\phi(x)}{dx} = \left[\frac{1-\lambda_y\varepsilon(x)}{1-\lambda_x\varepsilon(x)}\left(k_y - q_{\mathrm{D}y}^{(0)}\varepsilon(x)\tau_z\right)\sigma_z + i\frac{E-U(x)}{(1-\lambda_x\varepsilon(x))\,\hbar v_{\mathrm{F}}}\sigma_x + iq_{\mathrm{D}x}^{(0)}\varepsilon(x)\tau_z\right]\phi(x). \tag{6.48}$$

We have solved Eq. (6.48) numerically, for the nonuniform, smooth strain profile

$$\varepsilon(x) = \frac{\varepsilon_0}{\tanh(D/4\mathsf{a})}\left(\frac{1}{1+e^{-x/\mathsf{a}}} - \frac{1}{1+e^{-(x-D)/\mathsf{a}}}\right), \tag{6.49}$$

as shown in Fig. 6.14. Such a strain profile is essentially flat for $|x - D/2| \ll \mathsf{a}$, where $\varepsilon(x) \approx \varepsilon_0$, and for $|x - D/2| \gg \mathsf{a}$, where $\varepsilon(x) \approx 0$. In the limit $\mathsf{a}/D \to 0$, Eq. (6.49) tends to the sharp barrier. Therefore, asymptotically for $|x| \to \infty$, the solutions of Eq. (6.48) must merge into Eqs. (6.8), in regions I and III. We have therefore taken an initial value $\phi(x = x_0)$ in the form of Eq. (6.8c), for $x_0 = 5D$, and integrated Eq. (6.48) backwards for $x \ll 0$. Comparing the numerical solution with Eq. (6.8a), one may extract the reflection coefficient r, relative to an incident wave with unit amplitude incoming from $x > 0$, as the Fourier weight with respect to its negative frequency component, whence the transmission $T(\varphi)$ follows straightforwardly. As a cross-check of our procedure, we have also verified that the continuity equation, Eq. (6.9), holds true, within the numerical error.

Figs. 6.15 and 6.16 show our numerical results for the tunneling transmission $T(\varphi)$ across the smooth strain barrier, Eq. (6.49), with $D = 100$ nm and different values of the smoothing parameter, a/D. Fig. 6.15 refers to an incidence energy $E = 80$ meV, corresponding to an incident wavelength $\lambda_{\mathrm{F}} = \hbar v_{\mathrm{F}}/(2\pi E) \approx 1.3$ nm. One finds that transmission of propagating

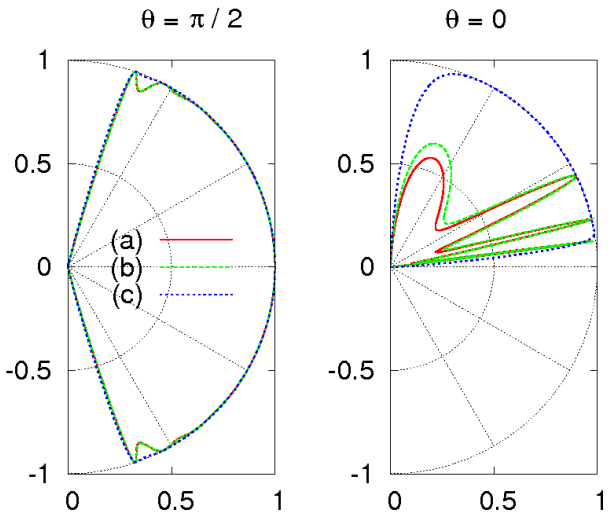

Figure 6.15: Tunneling transmission *vs* incidence angle φ across a smooth strain barrier, Eq. (6.49), with $D = 100$ nm, and incidence energy $E = 80$ meV ($\lambda_{\rm F} = \hbar v_{\rm F}/(2\pi E) \approx 1.3$ nm). Left panel refers to strain applied along the zig-zag direction ($\theta = \pi/2$), with $\varepsilon_0 = 0.1$. Right panel refers to strain applied along the armchair direction ($\theta = 0$), with $\varepsilon_0 = 0.01$. In both cases, the different lines correspond to different values of the smoothing parameter, *viz.* (a) a $= 0$ (sharp barrier); (b) a $= 10^{-2}D = 1$ nm; (c) a $= 10^{-1}D = 10$ nm. In all cases, $U(x) = 0$, for the sake of simplicity.

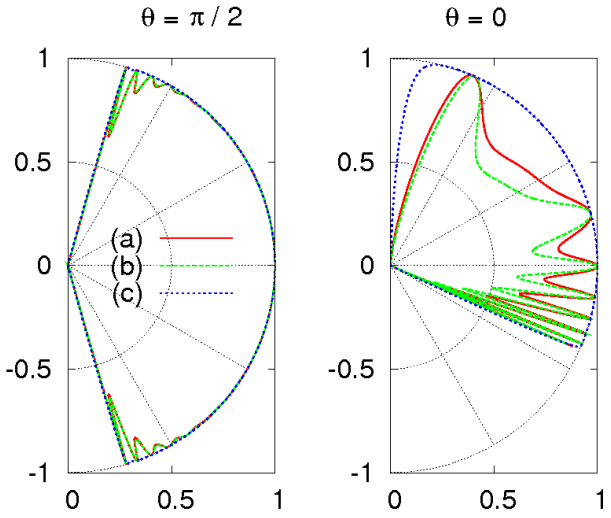

Figure 6.16: Same as Fig. 6.15, but with $E = 150$ meV ($\lambda_{\rm F} \approx 0.7$ nm).

waves is allowed for incidence angles φ such that $\varphi_{\mathrm{cr}-} \leq \varphi \leq \varphi_{\mathrm{cr}+}$, with

$$\varphi_{\mathrm{cr}\pm} = \pm \arcsin\left(\frac{1}{1-\lambda_y \varepsilon_0}\right), \tag{6.50}$$

in the zig-zag case ($\theta = \pi/2$), and $\varphi > \varphi_{\mathrm{cr}}$, with

$$\arcsin\left(-\frac{1}{1-\lambda_y \varepsilon_0} + \frac{\hbar v_{\mathrm{F}}}{a|E|}\varepsilon_0 \kappa(1-\nu)\right), \tag{6.51}$$

in the armchair case ($\theta = 0$), independent of the smoothing parameter a/D. Outside that window, transmission takes place via evanescent waves only, and $T(\varphi) \approx 0$. For strain applied along the zig-zag direction ($\theta = \pi/2$, Fig. 6.15, left panel), Eq. (6.50) predicts the existence of critical angles $|\varphi_{\mathrm{cr}\pm}| < \pi/2$. This is a direct consequence of the strain-induced deformation of the Dirac cones [$\lambda_y \neq 0$ in Eq. (6.50)]. Both in case of strain applied along the zig-zag and armchair directions, increasing the smoothness parameter a/D away from the limit of a sharp barrier ($\mathsf{a}/D = 0$) suppresses the oscillations in $T(\varphi)$ within the propagating window, until $\mathsf{a} > \lambda_{\mathrm{F}}$, in which case transmission is almost undisturbed by the presence of the barrier. These results are confirmed by Fig. 6.16, where we consider quasiparticles with larger incident energy $E = 150$ meV, corresponding to a smaller Fermi wavelength $\lambda_{\mathrm{F}} \approx 0.7$ nm. While the transmission window widens and the number of oscillations increases, smoothening the strain profile immediately washes out the deviations of the tunneling transmission from unity. In ending this paragraph, we note that the procedure applied to extracting the tunneling transmission from the numerical solution of Eq. (6.48) can be generalized, in principle, to the case of an arbitrary nonuniform strain potential, such as a superlattice of several smooth barriers, such as Eq. (6.49).

Conclusions

The present Thesis reports a theoretical study of the effects of strain on the electronic properties of graphene.

First of all, we have discussed the strain dependence of the electronic band structure, and derived the strain and electric field dependence of the optical conductivity of graphene under uniaxial strain. Within a tight-binding model, including strain-dependent nearest neighbour hoppings and orbital overlaps, we have interpreted the evolution of the band dispersion relations with strain modulus and direction in terms of the proximity to several electronic topological transitions (ETT). These correspond to the change of topology of the Fermi line as a function of strain. In the case of graphene, one may distinguish among three distinct ETTs. We also recover the evolution of the location of the Dirac points, which move away from the two inequivalent symmetric points K and K' as a function of strain. For sufficiently small strain modulus, however, one may still linearly expand the band dispersion relations around the new Dirac points, thereby recovering a cone approximation, but now with elliptical sections at constant energy, as a result of the strain-induced deformation. For increasing strain, two inequivalent Dirac points may merge into one, which usually occurs at either midpoint M_ℓ ($\ell = 1, 2, 3$) of the first Brillouin zone boundary, depending on the strain direction. This corresponds to the breaking down of linearity of the band dispersions along a given direction through the Dirac points, the emergence of low-energy quasiparticles with an anisotropic massive low-energy spectrum, and the opening of a gap in the energy spectrum. Besides, we confirm that such an event depends not only on the strain modulus, but characteristically also on the strain direction. In particular, no gap opens when strain is applied along the armchair direction. We derived the energy dependence of the density of states (DOS), and recovered a linear dependence at low energy within

the cone approximation, albeit modified by a renormalized strain-dependent slope. In particular, such a slope has been shown to increase with increasing strain modulus, regardless of the strain direction, thus suggesting that applied strain may obtain a steeper DOS in the linear regime. We have also calculated the DOS beyond the Dirac cone approximation. The proximity to ETTs gives rise to (possibly degenerate) Van Hove singularities in the density of states, appearing as logarithmic peaks in the DOS. Finally, we generalized our previous results for the optical conductivity to the case of strained graphene. We studied the frequency dependence of the longitudinal optical conductivity as a function of strain modulus and direction, as well as of field orientation. Our main results are that (a) logarithmic peaks appear in the optical conductivity at sufficiently high frequency, and can be related to the ETTs in the electronic spectrum under strain, and depending on the strain direction; (b) the relative weight of the peaks in general depends on the strain direction and field orientation, and contributes to the generally anisotropic pattern of the optical conductivity as a function of field orientation; (c) the opening of a band gap, where allowed, is signalled by a vanishing optical conductivity. The optical conductivity is directly related to measurable quantities, such as the transmittance and reflectance. Thus, an experimental study of the optical conductivity in the visible range of frequencies as a function of strain modulus and direction, as well as of field orientation, should enable one to identify the occurrence of the three distinct ETTs predicted for graphene. In addition, according to our results, the asymmetry induced by uniaxial strain in the optical conductivity causes an observable degree of dichroism. Indeed, the optical response of uniaxially strained graphene to linearly polarized light depends on the direction of the polarization. Moreover, the optical response of graphene can give information about the magnitude and the direction of strain in a graphene sample. Finally, these results about the effect of uniaxial strain on the electronic structure and optical conductivity are in agreement with recent *ab initio* calculations [122, 130].

After an in-depth study of the changes of electronic structure due to uniaxial strain, we dealt with the strain-induced modifications of the plasmons. By studying the electronic polarization, we have derived the dispersion relation of the plasmon modes in graphene. Besides including electron-electron correlation at the random phase approximation (RPA) level, we have considered local field effects (LFE), that are specific to the peculiar lattice structure under study, and

we have also taken into account the z-extension of the electron wave functions. Both terms are sizable in electron-electron scattering processes with large exchange momentum ($q \sim \pi/a$). As a consequence of the two-band character of the electronic band structure of graphene, we have found in general two plasmonic branches: (1) a low-energy branch, with a square-root behavior at small wavevectors, and (2) a high-energy branch, weakly dispersing at small wavevectors. In particular, we have found that the high-energy plasmon mode disappears neglecting LFE. While in the absence of LFE only scattering processes with momenta within the 1BZ are considered, LFE allow to include all scattering processes with arbitrarily low wavelengths, thereby taking into account the discrete nature of the crystalline lattice. Hence, the Umklapp electron-electron scattering processes have fundamental role in order that the system sustains the high-energy plasmon mode. Moreover, we have found an intermediate energy pseudo-plasmon mode, associated with a logarithmic divergence of the polarization, which can be related to an interband transition between the Van Hove singularities in the valence and conduction bands of graphene, and it can be identified with a $\pi \rightarrow \pi^*$ transition. In graphene, to date there are measurements about the low energy plasmon [30, 59] and the pseudo-plasmon excitation [41], whereas there is no clear experimental evidence about the high energy plasmon. Usually, experimental methodologies to detect plasmon dispersion relation, such as electron energy loss spectroscopy (EELS), measure the collective excitation at small wavevector limit ($q \rightarrow 0$) [41]. The detection of the high energy branch at small wavevector could be difficult, first of all, because of the reduced spectral weight associated with the high energy branch, but also because these plasmons could be damped by the promotions of electrons from the valence band into the higher (σ^*) energy band. In this Thesis we have not considered the electronic bands due to the σ electrons, and this possible correction will be the subject of future investigation.

Due to the robustness of the Dirac cones with respect to the application of uniaxial strain, for sufficiently small strain modulus, it is possible to use the massless Dirac approximation in order to describe the low energy electronic properties. In particular, exploiting the massless Dirac approximation, we have studied the dependence on applied uniaxial strain of density-density and current-current linear-response electronic correlation functions of graphene. Starting from these linear correlation functions, it is possible to obtain analytical results about several mea-

surable quantities of strained graphene, such as the plasmonic dispersion relation, the optical conductivity, as well as the static magnetic and electric susceptibilities. After deriving a general correspondence between strained and unstrained correlation functions, we derived the strain dependence of the low-energy plasmon dispersion relation and of the optical conductivity. Specifically, we found that the prefactor in the $\sqrt{q}$-dependence of the plasmon frequency develops an anisotropic character, with maximum (minimum) occurring when the wavevector is orthogonal (longitudinal) to the direction of applied strain. We have obtained that uniaxial strain induces an anisotropy on both the plasmonic dispersion relation and the electronic dispersion relation. Hence, we presume that the application of uniaxial strain on graphene could induce a modification of the plasmaronic resonance. We remind that plasmaron is an excitation which arises from the coupling of charge carriers and plasmons. Indeed, by means of a heuristic argument we found that uniaxial strain applied on graphene should induce a shifting and broadening of the plasmaron resonance energy, proportionally to the strain modulus. Therefore, by suitably applying uniaxial strain, one gains further control on the energy of the plasmaronic excitation, besides the possibility of tuning the relative dielectric constant ϵ_r. In addition, we have derived a strain-induced anisotropic enhancement of the deviations from the photonic behavior of the theoretically predicted transverse collective excitation, which should facilitate its experimental detection in suitably strained graphene samples.

Finally, we have studied the effect of a strain-induced one-dimensional profile on several ballistic transport properties of graphene. This study may be useful for the realization of a new class of ballistic devices designed by suitable tailoring of the electronic structure exploiting not only the electric field effect but also applied strain. In particular, we have studied the cases of a single strain-induced sharp barrier, and of a superstructure of several, periodically repeated, such sharp barriers. In both cases, we have dealt with the analysis of the angular dependence of the tunneling transmission, the conductivity, and the Fano factor. In particular, we have found that a strain-induced superlattice in graphene can accommodate additional resonant quasiparticle states, besides the ones usually found across a single barrier. We thus surmise that a strain-induced superlattice in graphene could be used as a filter for well-defined electronic resonant modes. After considering the cases of a single sharp tunneling barrier, and of a su-

perstructure of several, periodically repeated, such sharp barriers, we have specifically studied the more realistic case in which both the modulus of applied uniaxial strain, and possibly an applied gate potential, depend continuously on position.

List of publications

The research reported in this thesis is based on the following publications:

- F. M. D. Pellegrino, G. G. N. Angilella, and R. Pucci, *Strain effect on the optical conductivity of graphene*, Physical Review B **81**, 035411 (2010).
- F. M. D. Pellegrino, G. G. N. Angilella, and R. Pucci, *Dynamical polarization of graphene under strain*, Physical Review B **82**, 115434 (2010).
- F. M. D. Pellegrino, G. G. N. Angilella, and R. Pucci, *Effect of uniaxial strain on the Drude weight of graphene*, High Pressure Research **31**, 98 (2011).
- F. M. D. Pellegrino, G. G. N. Angilella, and R. Pucci, *Linear response correlation functions in strained graphene*, Physical Review B **84**, 195407 (2011).
- F. M. D. Pellegrino, G. G. N. Angilella, and R. Pucci, *Effect of uniaxial strain on plasmon excitations in graphene*, Journal of Physics: Conference Series **377**, 012083 (2012).
- F. M. D. Pellegrino, G. G. N. Angilella, and R. Pucci, *Transport properties of graphene across strain-induced nonuniform velocity profiles*, Physical Review B **84**, 195404 (2011).
- F. M. D. Pellegrino, G. G. N. Angilella, and R. Pucci, *Resonant modes in strain-induced graphene superlattices*, Physical Review B **85**, 195409 (2012).

Other publications, not included in this thesis:

- M. Orlita, P. Neugebauer,, C. Faugeras, A.-L. Barra, M. Potemski, F. M. D. Pellegrino, D. M. Basko, *Cyclotron Motion in the Vicinity of a Lifshitz Transition in Graphite*, Physical Review Letters **108**, 017602 (2012).

- F. M. D. Pellegrino, G. G. N. Angilella, and R. Pucci, *Ballistic transport properties across nonuniform strain barriers in graphene* High Pressure Research **32**, 18 (2012).

Acknowledgements

First of all, I would like to express my sincere gratitude to my long-time tutor, Prof. G. G. N. Angilella. From the very beginning, he taught me an huge amount of physical concepts, theoretical and numerical tools, and he continuously gave me real life suggestions, that have been all fundamental ingredients to become what I am today. In addition, I am grateful to Prof. R. Pucci for the stimulating discussions and his fruitful suggestions.

During my PhD course, I spent a period in Grenoble. In particular, I worked at Laboratoire de Physique et Modélisation des Milieux Condensés (LPMMC) for seven months, under the supervision of Dr. D. Basko. Therefore, I would like to thank Dr. D. Basko for his availability, patience and hospitality. He gave me the opportunity to work on very interesting problems, and he taught me a lot of elegant approaches to solve these problems. I thank Prof. B. van Tiggelen for his kindness and hospitality. I would like to thank Prof. V. Olevano for his useful suggestions. Moreover, in this period I had the opportunity to work with the experimental group of the Laboratoire National des Champs Magnétiques Intenses (LNCMI). In particular I am grateful to Prof. M. Potemski and Dr. M. Orlita. During this period in France, I met a lot of wonderful people, I would like to thank Filippo, Luca, Giulia, Arthur, Dani, Seb, Gianluca, Angelo D., Roberto & Elisa, Marco S. & Ester, Mathias, Ilaria, and Angelo C., because for them I have often forgotten being in a foreign country.

I am grateful to the coordinator of my PhD course, Prof. S. Mobilio. In addition, an acknowledgement is due to Dr. S. Venezia and Dr. F. Federici because they have beared me, and overall they have always solved my bureaucratic problems. Thanks to my colleagues Elisa, Alberto and Lorenzo. Although we met once a year, every time it has been a pleasant meeting.

I would like to thank all the people of the Dept of Physics and Astronomy, University of

Catania, with which I have had the pleasure of sharing enjoyable moments during these years. I would like to acknowledge Giorgia, we met during the first lessons of the degree course, and since then a true, sincere and fundamental friendship was born. A special thanks is due to Egidio, Lucia, Emanuele P. and Elena, for their friendship and the sincere discussions about any possible topic. I am grateful to Salvo I., Gianluca, Luca, Brunilde, Massimo G. and in particular Emanuele M., for sharing the PhD student room in a pleasant atmosphere. I would like to thank Giuseppe G. N., my true friend, for the amusing trips, the fantastic days that we have spent, and for those ones that we will spend together. Finally, I would like to thank Diana, Salvo C., Gigi, Adriano, Pietro, Gabriele, Daniele, Maria, Simona, Roberto, Salvo B., Dr. V. Privitera, Enzo, Roberta, and Alessio.

A special thanks to my dear friends and colleagues of the Scuola Superiore di Catania Alessandro, Paolo and Andrea, each of them is physically far, but during these years they have always been close to me.

I would like to thank my long-time friends Emilio, Federico, Dario, Vittorio, Carla, Ezio, Andrea Q., Fabrizio, because when we are together it seems that this long time has never passed. A special thanks to my fraternal friend Marco. Among my old friends I want to dedicate a personal thanks to Paul, David, Adam and Larry.

Finally, I would like to thank my parents for their infinite love and their confidence in me. A thanks to my sister Ramona, she is always ready to help me and she trusts me much more than I trust myself. The last and the most special thank to Stefania, *the sweetest thing* which destiny has given to me. I would like to thank Stefania, for her love, her patience, her continuous encouragement and an uncountable amount of other big and little reasons which make her my strength today, yesterday and tomorrow.

Bibliography

[1] S. H. Abedinpour, G. Vignale, A. Principi, M. Polini, W. K. Tse, and A. H. MacDonald, Phys. Rev. B **84**, 045429 (2011).

[2] S. L. Adler, Phys. Rev. **126**, 413 (1962).

[3] G. G. N. Angilella, E. Piegari, and A. A. Varlamov, Phys. Rev. B **66**, 014501 (2002).

[4] D. P. Arovas, L. Brey, H. A. Fertig, E. A. Kim, and K. Ziegler, New Journal of Physics **12**, 123020 (2010).

[5] N. W. Ashcroft and N. D. Mermin, *Solid State Physics* (Harcourt College Publishers, Harcourt, 1976).

[6] W. Bao, F. Miao, Z. Chen, H. Zhang, W. Jang, C. Dames, and C. N. Lau, Nature Nanotechnology **4**, 562 (2009).

[7] M. Barbier, P. Vasilopoulos, and F. M. Peeters, Phil. Trans. R. Soc. A **368**, 5499 (2010).

[8] W. L. Barnes, A. Dereux, and T. W. Ebbesen, Nature **424**, 824 (2003).

[9] D. M. Basko, Phys. Rev. B **78**, 125418 (2008).

[10] C. W. J. Beenakker, Rev. Mod. Phys. **80**, 1337 (2008).

[11] C. Bena and G. Montambaux, New Journal of Physics **11**, 095003 (2009).

[12] O. L. Blakslee, D. G. Proctor, E. J. Seldin, G. B. Spence, and T. Weng, J. Appl. Phys. **41**, 3373 (1970).

[13] Y. M. Blanter, Physics Reports **336**, 1 (2000).

[14] Y. M. Blanter, M. I. Kaganov, A. V. Pantsulaya, and A. A. Varlamov, Physics Reports **245**, 159 (1994).

[15] Y. P. Bliokh, V. Freilikher, and F. Nori, Phys. Rev. B **81**, 075410 (2010).

[16] K. I. Bolotin, K. J. Sikes, J. Hone, H. L. Stormer, and P. Kim, Phys. Rev. Lett. **101**, 096802 (2008).

[17] K. I. Bolotin, K. J. Sikes, Z. Jiang, M. Klima, G. Fudenberg, J. Hone, P. Kim, and H. L. Stormer, Solid State Communications **146**, 351 (2008).

[18] F. Bonaccorso, Z. Sun, T. Hasan, and A. C. Ferrari, Nature Photonics **4**, 611 (2010).

[19] T. J. Booth, P. Blake, R. R. Nair, D. Jiang, E. W. Hill, U. Bangert, A. Bleloch, M. Gass, K. S. Novoselov, M. I. Katsnelson, and A. K. Geim, Nano Letters **8**, 2442 (2008).

[20] A. Bostwick, T. Ohta, T. Seyller, K. Horn, and E. Rotenberg, Nature Physics **3**, 36 (2007).

[21] A. Bostwick, F. Speck, T. Seyller, K. Horn, M. Polini, R. Asgari, A. H. MacDonald, and E. Rotenberg, Science **328**, 999 (2010).

[22] V. W. Brar, S. Wickenburg, M. Panlasigui, C. H. Park, T. O. Wehling, Y. Zhang, R. Decker, C. Girit, A. V. Balatsky, S. G. Louie, A. Zettl, and M. F. Crommie, Phys. Rev. Lett. **104**, 036805 (2010).

[23] H. Bruus and K. Flensberg, *Many-body Quantum Theory in Condensed Matter Physics* (Oxford University Press, Oxford, 2004).

[24] J. S. Bunch, S. S. Verbridge, J. S. Alden, A. M. van der Zande, J. M. Parpia, H. G. Craighead, and P. L. McEuen, Nano Letters **8**, 2458 (2008).

[25] P. Burset, A. L. Yeyati, L. Brey, and H. A. Fertig, Phys. Rev. B **83**, 195434 (2011).

[26] M. Büttiker, Phys. Rev. Lett. **57**, 1761 (1986).

[27] E. Cadelano, P. L. Palla, S. Giordano, and L. Colombo, Phys. Rev. Lett. **102**, 235502 (2009).

[28] A. H. Castro Neto, F. Guinea, N. M. R. Peres, K. S. Novoselov, and A. K. Geim, Rev. Mod. Phys. **81**, 109 (2009).

[29] J. Cayssol, B. Huard, and D. Goldhaber-Gordon, Phys. Rev. B **79**, 075428 (2009).

[30] J. Chen, M. Badioli, P. Alonso-Gonzalez, S. Thongrattanasiri, F. Huth, J. Osmond, M. Spasenovic, A. Centeno, A. Pesquera, P. Godignon, A. Zurutuza Elorza, N. Camara, de Abajo, R. Hillenbrand, and F. H. L. Koppens, Nature pp. 77–81 (2012).

[31] J.-H. Chen, C. Jang, S. Xiao, M. Ishigami, and M. S. Fuhrer, Nature Nanotechnology **3**, 206 (2008).

[32] S. M. Choi, S. H. Jhi, and Y. W. Son, Phys. Rev. B **81**, 081407 (2010).

[33] A. Concha and Z. Tešanović, Phys. Rev. B **82**, 033413 (2010).

[34] S. Das Sarma, S. Adam, E. H. Hwang, and E. Rossi, Rev. Mod. Phys. **83**, 407 (2011).

[35] S. Das Sarma and E. H. Hwang, Phys. Rev. Lett. **102**, 206412 (2009).

[36] F. de Juan, A. Cortijoand, M. A. H. Vozmediano, and A. Cano, Nature Physics **7**, 810 (2011), 10.1038/nphys2034.

[37] C. R. Dean, A. F. Young, I. Meric, C. Lee, L. Wang, S. Sorgenfrei, K. Watanabe, T. Taniguchi, P. Kim, K. L. Shepard, and J. Hone, Nature Physics pp. 722–726 (2010).

[38] H. S. R. Dingle, A. Gossard, W. Wiegmann, and M. Sturge, Solid State Commun. **29**, 705 (1979bo).

[39] M. S. Dresselhaus, G. Dresselhaus, and A. Jorio, *Group Theory - Application to the Physics of Condensed Matter* (Springer, Berlin, 2008).

[40] X. Du, I. Skachko, A. Barker, and E. Y. Andrei, Nature Nanotechnology **3**, 491 (2008).

[41] T. Eberlein, U. Bangert, R. R. Nair, R. Jones, M. Gass, A. L. Bleloch, K. S. Novoselov, A. Geim, and P. R. Briddon, Phys. Rev. B **77**, 233406 (2008).

[42] L. A. Falkovsky and A. A. Varlamov, Eur. Phys. J. B **56**, 281 (2007).

[43] M. Farjam and H. Rafii-Tabar, Phys. Rev. B **80**, 167401 (2009).

[44] A. Fasolino, J. H. Los, and M. I. Katsnelson, Nature Materials **6**, 858 (2007).

[45] A. C. Ferrari, J. C. Meyer, V. Scardaci, C. Casiraghi, M. Lazzeri, F. Mauri, S. Piscanec, D. Jiang, K. S. Novoselov, S. Roth, and A. K. Geim, Phys. Rev. Lett. **97**, 187401 (2006).

[46] A. L. Fetter and J. D. Walecka, *Quantum Theory of Many-Particle Systems* (McGraw Hill, San Francisco, 1971).

[47] M. M. Fogler, F. Guinea, and M. I. Katsnelson, Phys. Rev. Lett. **101**, 226804 (2008).

[48] M. S. Fuhrer, C. N. Lau, and A. H. M. Donald, MRS Bulletin **35**, 289 (2010).

[49] M. H. Gass, U. Bangert, A. L. Bleloch, P. Wang, R. R. Nair, and A. K. Geim, Nature Nanotechnology **3**, 676 (2008).

[50] S. Gattenlöhner, W. Belzig, and M. Titov, Phys. Rev. B **82**, 155417 (2010).

[51] A. K. Geim, Rev. Mod. Phys. **83**, 851 (2011).

[52] A. K. Geim and K. S. Novoselov, Nature Materials **6**, 183 (2007).

[53] V. Geringer, M. Liebmann, T. Echtermeyer, S. Runte, M. Schmidt, R. Rückamp, M. C. Lemme, and M. Morgenstern, Phys. Rev. Lett. **102**, 076102 (2009).

[54] G. Giuliani and G. Vignale, *Quantum Theory of the Electron Liquid* (Cambridge University Press, Cambridge, 2005).

[55] N. Goldenfeld, *Lectures on Phase Transitions and the Renormalization Group* (Perseus Publishing, New York, 1992).

[56] G. Gómez-Santos and T. Stauber, Phys. Rev. Lett. **106**, 045504 (2011).

[57] J. González, F. Guinea, and M. A. H. Vozmediano, Phys. Rev. B **59**, R2474 (1999).

[58] I. S. Gradshteyn and I. M. Ryzhik, *Table of Integrals, Series, and Products* (Academic Press, Boston, 1994), 5th ed. edition.

[59] A. N. Grigorenko, M. Polini, and K. S. Novoselov, Nature Photonics **6**, 749 (2012).

[60] G. Gui, J. Li, and J. Zhong, Phys. Rev. B **78**, 075435 (2008).

[61] F. Guinea, M. I. Katsnelson, and A. K. Geim, Nature Physics **6**, 30 (2009).

[62] V. P. Gusynin and S. G. Sharapov, Phys. Rev. B **73**, 245411 (2006).

[63] I. Hamberg and C. G. Granqvist, J. Appl. Phys. **60**, R123 (1986).

[64] W. Hanke and L. J. Sham, Phys. Rev. Lett. **33**, 582 (1974).

[65] W. Hanke and L. J. Sham, Phys. Rev. B **12**, 4501 (1975).

[66] W. R. Hannes and M. Titov, EPL (Europhysics Letters) **89**, 47007 (2010).

[67] W. A. Harrison, *Electronic structure and the properties of solids* (Dover, New York, 1980).

[68] Y. Hasegawa, R. Konno, H. Nakano, and M. Kohmoto, Phys. Rev. B **74**, 033413 (2006).

[69] A. Hill, S. A. Mikhailov, and K. Ziegler, EPL (Europhysics Letters) **87**, 27005 (2009).

[70] E. H. Hwang and S. Das Sarma, Phys. Rev. B **75**, 205418 (2007).

[71] M. Hytch, F. Houdellier, F. Hue, and E. Snoeck, Nature **453**, 1086 (2008).

[72] M. Jablan, H. Buljan, and M. Soljačić, Phys. Rev. B **80**, 245435 (2009).

[73] M. Jablan, H. Buljan, and M. Soljavcić, Opt. Express **19**, 11236 (2011).

[74] M. Jablan, M. Soljavcić, and H. Buljan, Phys. Rev. B **83**, 161409 (2011).

[75] J. W. Jiang, J. S. Wang, and B. Li, Phys. Rev. B **81**, 073405 (2010).

[76] M. I. Katsnelson, *Graphene - Carbon in Two Dimensions* (Cambridge University Press, Cambridge, 2012).

[77] K. S. Kim, Y. Zhao, H. Jang, S. Y. Lee, J. M. Kim, K. S. Kim, J. H. Ahn, P. Kim, J. Y. Choi, and B. H. Hong, Nature **457**, 706 (2009).

[78] F. H. Koppens, D. E. Chang, and J. G. de Abajo, Nano Letters **11**, 3370 (2011).

[79] M. Koshino and T. Ando, Phys. Rev. B **75**, 235333 (2007).

[80] L. D. Landau and E. M. Lifshitz, *Theory of Elasticity* (Pergamon, , 1986), 3rd ed. edition.

[81] R. Landauer, IBM J. Res. Develop. **223**, 223 (1957).

[82] C. Lee, X. Wei, J. W. Kysar, and J. Hone, Science **321**, 385 (2008).

[83] E. J. H. Lee, K. Balasubramanian, R. T. Weitz, M. Burghard, and K. Kern, Nature Nanotechnology **3**, 486 (2008).

[84] M. L. Lee, E. A. Fitzgerald, M. T. Bulsara, M. T. Currie, and A. Lochtefeld, J. Appl. Phys. **97**, 011101 (2005).

[85] Z. Li, E. Henriksen, Z. Jiang, Z. Hao, M. Martin, P. Kim, H. Stormer, and D. Basov, Nature Physics **4**, 532 (2008).

[86] I. M. Lifshitz, Zh. Eksp. Teor. Fiz. **38**, 1565 (1960).

[87] F. Liu, P. Ming, and J. Li, Phys. Rev. B **76**, 064120 (2007).

[88] T. Low and F. Guinea, Nano Letters **10**, 3551 (2010).

[89] T. Low, V. Perebeinos, J. Tersoff, and P. Avouris, Phys. Rev. Lett. **108**, 096601 (2012).

[90] B. I. Lundqvist, Phys. Kondens. Materie **6**, 193 (1967).

[91] B. I. Lundqvist, Phys. Kondens. Materie **6**, 206 (1967).

[92] G. D. Mahan, *Many Particle Physics* (Plenum, New York, 2000).

[93] K. F. Mak, M. Y. Sfeir, Y. Wu, C. H. Lui, J. A. Misewich, and T. F. Heinz, Phys. Rev. Lett. **101**, 196405 (2008).

[94] M. R. Masir, P. Vasilopoulos, and F. M. Peeters, New Journal of Physics **11**, 095009 (2009).

[95] J. W. McClure, Phys. Rev. **104**, 666 (1956).

[96] A. Messiah, *Quantum Mechanics* (John Wiley & Sons, New York, 1958).

[97] J. C. Meyer, A. K. Geim, M. I. Katsnelson, K. S. Novoselov, T. J. Booth, and S. Roth, Nature **446**, 60 (2007).

[98] S. A. Mikhailov and K. Ziegler, Phys. Rev. Lett. **99**, 016803 (2007).

[99] T. M. G. Mohiuddin, A. Lombardo, R. R. Nair, A. Bonetti, G. Savini, R. Jalil, N. Bonini, D. M. Basko, C. Galiotis, N. Marzari, K. S. Novoselov, A. K. Geim, and A. C. Ferrari, Phys. Rev. B **79**, 205433 (2009).

[100] S. V. Morozov, K. S. Novoselov, M. I. Katsnelson, F. Schedin, D. C. Elias, J. A. Jaszczak, and A. K. Geim, Phys. Rev. Lett. **100**, 016602 (2008).

[101] R. R. Nair, P. Blake, A. N. Grigorenko, K. S. Novoselov, T. J. Booth, T. Stauber, N. M. R. Peres, and A. K. Geim, Science **320**, 1308 (2008).

[102] S. G. Nam, D. K. Ki, J. W. Park, Y. Kim, J. S. Kim, and H. J. Lee, Nanotechnology **22**, 415203 (2011).

[103] K. S. Novoselov, Rev. Mod. Phys. **83**, 837 (2011).

[104] K. S. Novoselov, A. K. Geim, S. V. Morozov, D. Jiang, Y. Zhang, S. V. Dubonos, I. V. Grigorieva, and A. A. Firsov, Science **306**, 666 (2004).

[105] K. S. Novoselov, D. Jiang, T. Booth, V. V. Khotkevich, S. M. Morozov, and A. K. Geim, Proc. Natl. Acad. Sci. USA **102**, 10451 (2005).

[106] M. Orlita, P. Neugebauer, C. Faugeras, A.-L. Barra, M. Potemski, F. M. D. Pellegrino, and D. M. Basko, Phys. Rev. Lett. **108**, 017602 (2012).

[107] E. Ozbay, Science **311**, 189 (2006).

[108] I. Paul and G. Kotliar, Phys. Rev. B **67**, 115131 (2003).

[109] F. M. D. Pellegrino, G. G. N. Angilella, and R. Pucci, Phys. Rev. B **80**, 094203 (2009), arXiv:0909.1903.

[110] F. M. D. Pellegrino, G. G. N. Angilella, and R. Pucci, High Pressure Research **29**, 569 (2009), arXiv:0912.3616.

[111] F. M. D. Pellegrino, G. G. N. Angilella, and R. Pucci, Phys. Rev. B **82**, 115434 (2010), arXiv:1008.4454.

[112] F. M. D. Pellegrino, G. G. N. Angilella, and R. Pucci, Eur. Phys. J. B **76**, 469 (2010), arXiv:1006.4078v1.

[113] F. M. D. Pellegrino, G. G. N. Angilella, and R. Pucci, Phys. Rev. B **81**, 035411 (2010), arXiv:0912.3614.

[114] F. M. D. Pellegrino, G. G. N. Angilella, and R. Pucci, High Pressure Research **31**, 98 (2011), arXiv:1009.3453.

[115] F. M. D. Pellegrino, G. G. N. Angilella, and R. Pucci, Phys. Rev. B **84**, 195407 (2011), arXiv:1110.4036.

[116] F. M. D. Pellegrino, G. G. N. Angilella, and R. Pucci, Phys. Rev. B **84**, 195404 (2011), arXiv:1110.3391.

[117] F. M. D. Pellegrino, G. G. N. Angilella, and R. Pucci, High Pressure Research **32**, 18 (2012), arXiv:1112.3836.

[118] F. M. D. Pellegrino, G. G. N. Angilella, and R. Pucci, Phys. Rev. B **85**, 195409 (2012), arXiv:1203.4368v1.

[119] F. M. D. Pellegrino, G. G. N. Pucci, and R. Pucci, Journal of Physics: Conference Series **377**, 012083 (2012), arXiv:1206.2098.

[120] V. M. Pereira and A. H. Castro Neto, Phys. Rev. Lett. **103**, 046801 (2009).

[121] V. M. Pereira, A. H. Castro Neto, and N. M. R. Peres, Phys. Rev. B **80**, 045401 (2009).

[122] V. M. Pereira, R. M. Ribeiro, N. M. R. Peres, and A. H. Castro Neto, EPL (Europhysics Letters) **92**, 67001 (2010).

[123] N. M. R. Peres, Rev. Mod. Phys. **82**, 2673 (2010).

[124] N. M. R. Peres, F. Guinea, and A. H. Castro Neto, Phys. Rev. B **73**, 125411 (2006).

[125] I. Pletikosić, M. Kralj, P. Pervan, R. Brako, J. Coraux, A. T. N'Diaye, C. Busse, and T. Michely, Phys. Rev. Lett. **102**, 056808 (2009).

[126] M. Polini, R. Asgari, G. Borghi, Y. Barlas, T. Pereg-Barnea, and A. H. MacDonald, Phys. Rev. B **77**, 081411 (2008).

[127] A. Principi, M. Polini, and G. Vignale, Phys. Rev. B **80**, 075418 (2009).

[128] A. Raoux, M. Polini, R. Asgari, A. R. Hamilton, R. Fazio, and A. H. MacDonald, Phys. Rev. B **81**, 073407 (2010).

[129] S. Reich, J. Maultzsch, C. Thomsen, and P. Ordejón, Phys. Rev. B **66**, 035412 (2002).

[130] R. M. Ribeiro, V. M. Pereira, N. M. R. Peres, P. R. Briddon, and A. H. Castro Neto, New Journal of Physics **11**, 115002 (2009).

[131] E. Rossi, J. H. Bardarson, P. W. Brouwer, and S. Das Sarma, Phys. Rev. B **81**, 121408 (2010).

[132] R. Saito, M. Fujita, G. Dresselhaus, and M. S. Dresselhaus, *Physical properties of carbon nanotubes* (Imperial College Press, London, 1998).

[133] J. J. Sakurai, *Modern Quantum Mechanics* (Addison-Wisley, New York, 1985).

[134] W. Schattke, *Encyclopedia of Condensed Matter Physics*, volume 1, p. 145 (Elsevier, Amsterdam, 2005), edited by F. Bassani, G. L. Liedl, and P. Wyder.

[135] F. Schwierz, Nature Nanotechnology **5**, 487 (2010).

[136] G. W. Semenoff, Phys. Rev. Lett. **53**, 2449 (1984).

[137] T. Stauber and G. Gómez-Santos, Phys. Rev. B **82**, 155412 (2010).

[138] T. Stauber, N. M. R. Peres, and A. K. Geim, Phys. Rev. B **78**, 085432 (2008).

[139] T. Stauber, J. Schliemann, and N. M. R. Peres, Phys. Rev. B **81**, 085409 (2010).

[140] E. Stolyarova, K. T. Rim, S. Ryu, J. Maultzsch, P. Kim, L. E. Brus, T. F. Heinz, M. S. Hybertsen, and G. W. Flynn, Proc. Natl. Acad. Sci. USA **104**, 9209 (2007).

[141] S. M. Sze and K. K. Ng, *Physics of Semiconductor Devices* (John Wiley & Sons, Hoboken, New Jersey, 2007).

[142] M. Titov, EPL (Europhysics Letters) **79**, 17004 (2007).

[143] P. E. Trevisanutto, M. Holzmann, M. Côté, and V. Olevano, Phys. Rev. B **81**, 121405 (2010).

[144] W. K. Tung, *Group Theory in Physics* (World Scientific, Singapore, 1985).

[145] J. Tworzydło, B. Trauzettel, M. Titov, A. Rycerz, and C. W. J. Beenakker, Phys. Rev. Lett. **96**, 246802 (2006).

[146] C. A. Ullrich and G. Vignale, Phys. Rev. B **65**, 245102 (2002).

[147] O. Vafek, Phys. Rev. Lett. **97**, 266406 (2006).

[148] M. van Schilfgaarde and M. I. Katsnelson, Phys. Rev. B **83**, 081409 (2011).

[149] A. L. Vázquez de Parga, F. Calleja, B. Borca, M. C. G. Passeggi, J. J. Hinarejos, F. Guinea, and R. Miranda, Phys. Rev. Lett. **100**, 056807 (2008).

[150] J. Velasco Jr., G. Liu, W. Bao, and C. N. Lau, New Journal of Physics **11**, 095008 (2009).

[151] P. R. Wallace, Phys. Rev. **71**, 622 (1947).

[152] A. L. Walter, A. Bostwick, K.-J. Jeon, F. Speck, M. Ostler, T. Seyller, L. Moreschini, Y. J. Chang, M. Polini, R. Asgari, A. H. MacDonald, K. Horn, and E. Rotenberg, Phys. Rev. B **84**, 085410 (2011).

[153] T. O. Wehling, I. Grigorenko, A. I. Lichtenstein, and A. V. Balatsky, Phys. Rev. Lett. **101**, 216803 (2008).

[154] L. Wu, S. He, and L. Shen, Phys. Rev. B **67**, 235103 (2003).

[155] B. Wunsch, T. Stauber, F. Sols, and F. Guinea, New Journal of Physics **8**, 318 (2006).

[156] P. Yeh, A. Yariv, and C. S. Hong, J. Opt. Soc. Am. **67**, 423 (1977).

[157] A. F. Young and P. Kim, Nature Physics **5**, 222 (2009).

[158] M. F. Yu, O. Lourie, M. J. Dyer, K. Moloni, T. F. Kelly, and R. S. Ruoff, Science **287**, 637 (2000).

[159] P. Y. Yu and M. Cardona, *Fundamentals of Semiconductors: Physics and Materials Properties* (Springer, Berlin, 2010).

[160] J. Zabel, R. R. Nair, A. Ott, T. Georgiou, A. K. Geim, K. S. Novoselov, and C. Casiraghi, Nano Letters (2011).

Index